2012

Isothermal Deformation and Modeling of Ti-6al-4v

Vamsi Krishna Vempati
Wright State University

ISOTHERMAL DEFORMATION AND MODELING OF Ti-6Al-4V

A thesis submitted in partial fulfillment of the
requirements for the degree of
Master of Science

By

Vamsi Krishna Vempati

B.Tech, JNTU, 2009

2012
Wright State University

WRIGHT STATE UNIVERSITY

GRADUATE SCHOOL

June 15, 2012

I HEREBY RECOMMEND THAT THE THESIS PREPARED UNDER MY SUPERVISION BY Vamsi Krishna Vempati ENTITLED Isothermal Deformation And Modeling Of Ti-6Al-4V BE ACCEPTED IN PARTIAL FULFILLMENT OF THE REQUIREMENTS FOR THE DEGREE OF Master of Science in Engineering.

_____

Raghavan Srinivasan, Ph.D.
Thesis Director

_____

George Huang, Ph.D.
Department Chair

Committee on
Final Examination

_____
Raghavan Srinivasan, Ph.D.

_____
Sharmila M Mukhopadyay, Ph.D.

_____
Balakrishna Cherukuri, Ph.D.

_____
Andrew Hsu, Ph.D.
Dean, School of Graduate Studies

ABSTRACT

Vempati, Vamsi Krishna, M.S.Egr, Department of Mechanical and Materials Engineering, Wright State University, 2012. Isothermal Deformation and Modeling of Ti-6Al-4V

Ti-6Al-4V has attractive properties such as high strength to weight ratio, good fatigue properties and excellent corrosion resistance and these properties have made this alloy an important material for the aerospace industry. In this thesis, the deformation behavior of Ti-6Al-4V with several processing histories, was studied by conducting isothermal constant strain rate compression tests over a temperature range of 829^{o}C to 996^{o}C (1525^{o}F to 1825^{o}F) and at strain rates of 10^{-2} s^{-1}, 10^{-1} s^{-1} and 10^{0} s^{-1}. True stress versus true strain flow curves showed a peak stress followed by flow softening. The data was analyzed to obtain constitutive equations to describe the variation of flow stress as a function of strain, strain rate and temperature. The strain rate sensitivity values were found to increase as the temperature was increased, and the activation energy for deformation was found to be comparable to values reported in literature.

Finite element simulations were carried out using the temperature corrected flow curves as input. The simulated and experimental results were found to be comparable to each other.

ACKNOWLEDGMENTS

First I would like to thank my thesis advisor, Dr. Raghavan Srinivasan, for his valuable support, guidance and his helpful attitude during the course of my Master's program of 2 years.

I am grateful to Dr. Balakrishna Cherukuri from RTI Intl., Niles, Oh, for his guidance and for serving on the thesis committee. Sincere thanks to Arjaan Buijik from Simufact Forming for helping me out with the finite element simulations used for this study. Special thanks to Dr. Sharmila Mukhopadhyay for serving on the thesis committee.

Finally I would like to thank my parents, family and friends for showing a great love, support and encouragement.

Table of Contents

List of Figures

List of Tables

Chapter 1

Introduction

Metallic Titanium (Ti) was first extracted over two centuries ago and with time it has spread its wings in terms of applications into various sectors of engineering. Ti is the fourth most abundant structural metal available on the earth's crust, and is exceeded in abundance only by magnesium, aluminum and iron [1]. If Ti as an element is considered then it is the ninth most abundant element in the earth's crust, and is exceeded by potassium, magnesium, sodium, calcium, iron, aluminum, silicon and oxygen [2]. Ti has a high melting point of 1725 ^{0}C, which is about 200 ^{0}C higher than that of melting point of steel and is considered to be a refractory material. The density of Ti is about 4.51 g/cm^{3} which are ~60% than that of steel [3]. Other important properties of Ti include relatively low electrical conductivity, low thermal conductivity, and good corrosion resistance [4]. Ti is not present in metallic form in the earth's crust and hence needs to be processed to extract from its ore. Important Ti ores are Ilminite ($FeTiO_3$), Rutile (TiO_2) and Leucoxene [5]. Ilminite has 53% of TiO_2, Leucoxene has 90% TiO_2 and Rutile is 100% TiO_2. Across the globe Australia, Canada, China, Norway, South Africa and Ukraine are the countries, which are the major producers of Ti and in United States New York, Virginia, New Jersey, Florida and Idaho are the major producers of Ti [1, 2]. All the properties stated above can be enhanced or decreased by the addition of alloying elements. Taking advantages of the above properties Ti has its applications in aerospace, marine, chemical industries and medical implants [2].

Metallic Ti is extracted from its ores such as Rutile using the Kroll's process [5], which involves subjecting the ore by a reduction process in the presence of coke and then chlorinating to obtain $TiCl_4$. The $TiCl_4$ is then reduced using Mg to obtain Ti sponge [1].

Once the Ti sponge is obtained, ingots are produced by mixing the sponge with alloying elements and Ti scrap in vacuum arc furnaces under inert atmospheres. Multiple melting operations are carried out in the same furnace to enhance the homogeneity of the ingot. Once the ingot is produced and a primary operation such as forging is done to obtain a mill product and secondary operations such as extrusion is carried out on the mill product to yield the final product.

Ti- 6 Aluminum- 4 Vanadium (Ti6Al4V) is an alloy of Ti also known as grade 5 alloy of Ti. Ti6Al4V is an important alloy of Ti and has found its major usage in the aerospace industry. Ti6Al4V is an alpha beta alloy, wherein Al acts as alpha stabilizer and V acts as beta stabilizer. Improved properties such as high strength to weight ratio, good fatigue properties and excellent corrosion resistance have made Ti6Al4V a leader in the manufacturing of aerospace components. Adding alloying elements to Ti enhances its mechanical as well as it physical properties.

Ti-6Al-4V with several processing histories was studied. Four different materials which were used for this study are:

1. Pre HIPed alpha-beta processed.

2. Pre HIPed beta processed.

3. Post HIPed alpha-beta processed.

4. Post HIPed beta processed.

Hot Isostatic Pressing (HIP) is a heat treatment technique where in the material is heated to a high temperature under high pressures in a pressure vessel to get rid of internal porosity in the material.

Hot constant strain rate compression tests at temperatures of 829^0C, 885^0C, 940^0C and 996^0C were carried out at different strain rates of 10^{-2} s^{-1}, 10^{-1} s^{-1} and 10^0 s^{-1}. Flow curve analysis, constitutive modeling, microstructural analysis using optical microscopy and finite element simulations were done.

Chapter 2

Background of Titanium and its alloys

This chapter deals with the background of titanium alloys and also discusses the microstructure of Ti6Al4V. The materials used for experiments in this thesis belong to the alpha-beta group of titanium alloys which are briefly presented. The different processing techniques for alpha-beta alloys are examined in detail.

Titanium exhibits allotropy like many other metals. The two allotropic forms of titanium are the alpha phase and the beta phase. Titanium is in a hexagonal closed packed (hcp) crystal structure also known as "alpha phase" at room temperature. As the temperature is increased to $882 \pm 2^{o}C$ its crystal structure changes to body centered cubic (bcc) structure also known as "beta phase" [6]. Figure 1 shows the unit cells of alpha and beta structures.

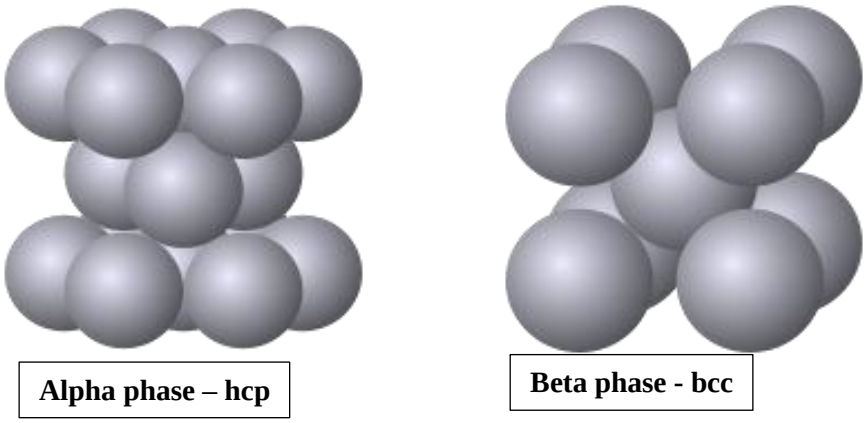

Figure 1: Crystal Structures of alpha and beta unit cells

The transformation temperature of $882 \pm 2^{o}C$ where titanium changes its crystal structure is know as the beta transus (T_{β}). Alloying elements and interstitial elements can alter the beta transus temperature [4]. Alloying elements such as aluminum, tin and oxygen which are also called as alpha stabilizers, increase the temperature to which the alpha phase is stable and on the other hand elements such as molybdenum,vanadium and tungsten can stabilize the beta phase and lower the beta transus temperature. Table 1 shows the ranges and effects of different alloying elements that can be added to Ti.

Table 1: Effects of different alloying elements on Ti

Alloying Elements	Range (appx. Wt%)	Effect on Structure
Aluminum	2 to 7	Alpha Stabilizer
Tin	2 to 6	Alpha Stabilizer
Vanadium	2 to 20	Beta Stabilizer
Molybdenum	2 to 20	Beta Stabilizer
Chromium	2 to 12	Beta stabilizer
Copper	2 to 6	Beta Stabilizer
Zirconium	2 to 8	Alpha and beta Strengthner
Silicon	0.2 to 1	Improves creep resistance

2.1 Classification of titanium alloys

Titanium can be classified into four different types of alloys which are:

- Alpha
- Near alpha
- Alpha-beta
- Beta

2.1.1 Unalloyed or Pure Titanium

Commercially pure titanium is available in different grades and the major difference between these grades is the amount of oxygen and iron which are considered impurities [1,2,4]. The grades with lower content of impurities have a lower hardness, strength and transformation temperature compared to the grades which have higher content [7].

Commmercially pure (CP) titanium exhibits excellent corrosion resistance and is bio-compatable, these two reasons have made commercially pure titanium find its usage in the field of bio medical applications [7].

CP titanium has a yield strength which varies between 170 MPa to 480 MPa [7] and a fracture toughness between the range of 66 MPa.√m to 135 MPa.√m [8], because of these low values of fracture toughness CP titanium has generally found its useage which do not require high strength. Some of the other areas where CP titanium has its useage are heat exchangers and reaction chambers of chemical plants [9].

Table 2 shows the different grades of CP titanium and their chemical compositions.

Table 2: Different grades of pure titanium and their chemical composition

Element	Grade-1 ELI	Grade-1	Grade-2	Gade-3	Grades 4A/4B
Oxygen	0.1	0.18	0.25	0.35	0.4
Iron	0.1	0.2	0.3	0.3	0.5
Nitrogen	0.012	0.03	0.03	0.05	0.05
Carbon	0.03	0.1	0.1	0.1	0.1
Hydrogen	0.125	0.125	0.125	0.125	0.125
Titanium	Balance	Balance	Balance	Balance	Balance

2.1.2 Alpha and Near Alpha alloys

Titanium alloys when mixed with one or more alpha stabilizers such as aluminum, galium or tin are know as alpha or near alpha alloys [1,2]. These alloys exhibit a hcp structure at room temperature. Some of the alloys belonging to alpha phase are Ti-5Al-2.5 Sn and Ti-Al-Ga alloys. When alpha alloys are mixed with small amounts of beta stabilizers (maximum of 2% [10]) then such group of alloys are classified to be “super alpha” or “near alpha” alloys [6]. Some of the alloys belonging to near alpha group are: Ti-8Al-1Mo-1V and Ti-6Al-2Nb-1Ta-0.8Mo. Rosenberg showed the effect of alpha

stabilizers on titanium alloys by forming an equation which shoes equivalent amount of aluminum to be present and the equation is given as [10]:

$$Al_{eq} = Al + \frac{1}{3}\,Sn + \frac{1}{6}\,Zr + 10\,(O + C + 2N)\ wt\%$$

The maximum amount of Al_{eq} is 9%, this is to avoid embrittlement [10].

Alpha alloys are known for their strength, creep resistance, toughness and weldbility [11] and because of these properties alpha alloys have found their useage in the field of cryogenic applications[3,11]. Near alpha/super alpha alloys can be heat treatable only to a certain extent. Thermo-mechanical operations such as forgings can be done using small reduction steps to control their microstructural properties [10].

2.1.3 Alpha – Beta alloys

Alpha-Beta alloys are the class of titanium alloys which contain one or more alpha stabiliziers in addition to one or more beta stabilizers. Since these alloys contain both the alpha and beta stabilizers, their microstructure is a combination of alpha phase (hcp) and the beta phase (bcc). Strengthining of alpha beta alloys is done by solution treating them to high temperatures and then quenching in water, oil or other soluble quenching agents. This solution treating results in the formation of retained beta. The amount of retained beta in alpha beta alloys is greater than compared to near alpha alloys.

The solution treating and aging process increase the strength of alpha beta alloys by 30-50% [4]. The amount of beta phase at room temperature in these alloys is between 4-6% [1,4]. Mechanical properties of these alloys are strongly dependent on the initial microstructures and the microstructures can be controlled by thermo-mechnical

processing [12]. The thermo-mechanical routes can produce either fully lamellar or bi-modal structures of lamellar and equiaxed grains depending on the final desired properties.

Alpha colony size is an other factor which controls the mechanical properties of alpha beta alloys [12]. The smaller the alpha colony size the better are the properties such as yield strength,ductility and fatigue strength [12]. One of the most common alloys of titanium which is Ti-6Al-4V belong to this class of alloys. Some of the other alpha beta alloys are Ti-6Al-6V-2Sn, Ti-7Al-4Mo, Ti-5Al-2Sn-2Zr-4Mo-4Cr.

2.1.4 Beta Alloys

Beta alloys are the class of titanium alloys which contain one or more beta stabilzers and very small amounts of alpha stabilizers [4]. Beta alloys are charecteristic for their high hardenability and have excellent forgability. The amount of beta stabilizers in a beta alloy can be expressed by the amount of molybdenum equivalent (Mo_{eq}) and can be expressed as [13]:

$$Mo_{eq} = 1\,Mo + 0.67V + 0.44W + 0.28Nb + 0.22Ta + 2.9\,Fe + 1.6\,Cr - 1Al\ wt\%$$

Beta phase is generally a metastable phase and hence has a tendency to transform into equilibrium alpha plus beta structure [2]. Beta alloys are considered for their low modulus, good castability, deep hardenability and good corrosion resistance. The disadvantage of beta alloy in comparison to alpha beta alloys are high density, low creep resistance and low ductility [14]. Beta alloys have found their usage in military,

aerospace and bio medical applications. Some of the beta alloys are Ti-13V-11Cr-3Al, Ti-10V-2Fe-3Al and Ti-3Al-8V-6Cr-4Mo-4Zr.

2.2 Ti-6Al-4V

The work presented in this thesis is with Ti-6Al-4V an alpha-beta alloy which has excellent mechanical properties. This alloy is widely used and accounts for 80% of usage of titanium in the aircraft industry.

Ti-6Al-4V can be produced in a various formulations. Depending on the field of application the amounts of the oxygen and nitrogen in the alloy can be controlled. The amount of oxygen in the alloy is between 0.08 to 0.2% and the maximum concentration of nitrogen is 0.05% [4]. The higher the concentrations of nitrogen and oxygen result in greater strength of the alloy; conversely lower concentrations of nitrogen and oxygen increase the ductility, fracture toughness, stress corrosion resistance and resistance to crack growth [2,4].

Ti-6Al-4V is available in wrought form, cast, or powder metallurgy form. However 95% of the industrial applications use the alloy in the wrought form. Wrought alloys are used in the mill annealed condition which exhibits a favorable combination of properties such as strength, ductility and fatigue [4]. Most of the cast forms of titanium are used in the hot isostatic pressed (HIP) form which removes any internal porosity present in the alloy and thereby increasing its mechanical properties.

Aluminum which acts as an alpha stabilizer increases the tensile strength and elastic modulus by a solid solution strengthening mechanism. But greater than 6% of

aluminum would result in the forming of Ti_3Al, which is a brittle intermetallic. Vanadium on the other hand acts as beta stabilizer which has similar structure as that of Ti and by the addition of vanadium the formation of inter metallic can be decreased.

2.3 Processing and Microstructure

Ti-6Al-4V can be thermo mechanically processed to obtain three different types of microstructures, each of which can be used for different applications. The three microstructures are [17]:

(i) Fully lamellar structure

(ii) Fully equiaxed structure

(iii) Bi-modal structure

2.3.1 Lamellar Structure

Lamellar type of microstructure is obtained by an annealing treatment in the beta phase field and for this reason this lamellar structure is often called as "β annealed structure" [15]. The processing sequence can be seen in the Figure 2 [17].

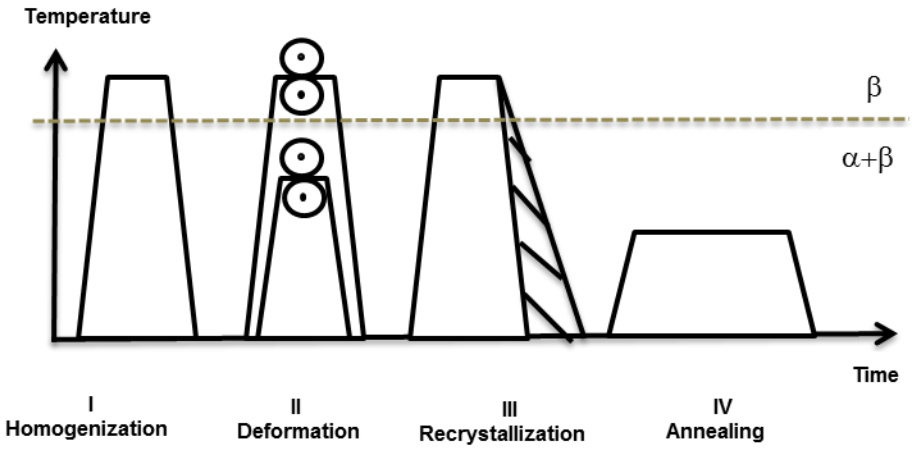

Figure 2: Processing sequence for lamellar type β annealed microstructure [based from ref. 17]

The deformation process involves operations such as forging, side pressing and side cogging. These deformation steps help in achieving chemical homogenity and break down of as cast microstructure. After the completion of the deformation process, if a faster cooling opertion such as air cooling is done then a lamellar or Widmanstatten kind of microstructure is obtained [15]. This lamellar structure is useful in applications where fracture toughness and creep play a major role [17]. Cooling rate plays a major role recrystallization step. As the cooling becomes faster, the alpha lamellae, colony size and width of alpha layer at beta boundaries decreases. Final annealing treatment is done to obtain a martenstitic structure. In this final heat treatment process temperature plays a important role. For Ti-6Al-4V, Ti_3Al solvus temperature is 550^oC, so aging at 500^oC will precipitate out Ti_3Al, whereas aging at 600^oC will result in stress relieving [17].

Another lamellar structure that can be obtained is the beta processed structure. This kind of structure is greatly used for beta titanium alloys than for alpha beta alloys. The procedure to produce the beta processed lamellar is same as that of beta annealed

process but in this case the step of recrystallization is not present [17]. The important parameters to be considered during the primary deformation are time, temperature and strain rate. Figure 3 shows the processing route for beta processed microstructure [17].

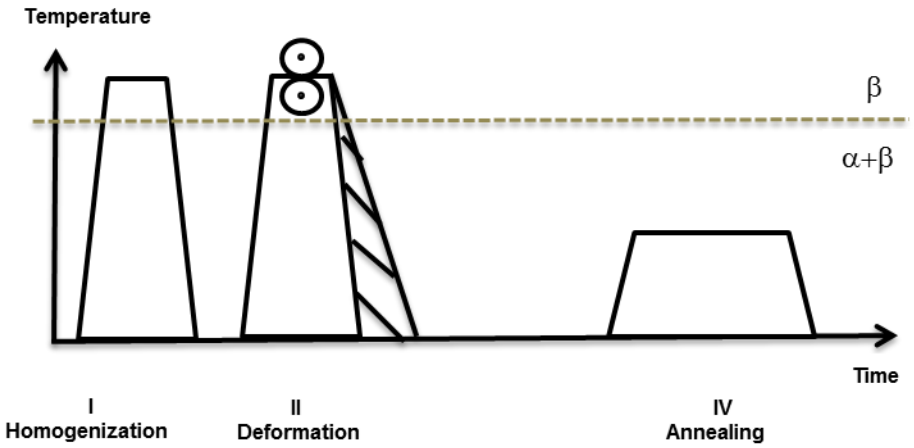

Figure 3 : Processing sequence for lamellar type beta processed microstructure [based from ref. 17]

Figure 4 shows an example of a lamellar microstructure.

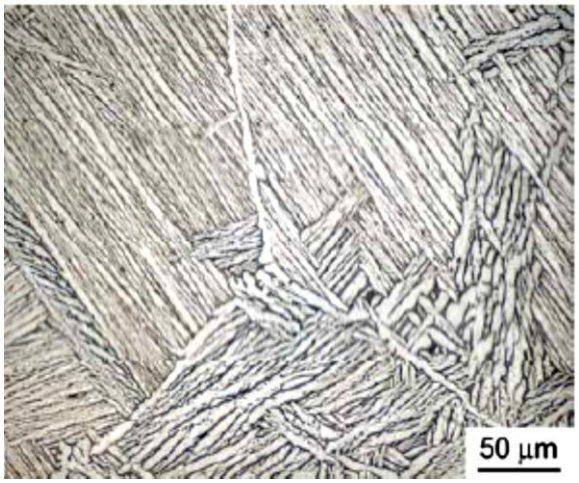

Figure 4: Lamellar Microstructure [18]

2.3.2 Bimodal Structure

Bimodal structures are also know as duplex microstructures. Processing route to obtain a bimodal structure is shown in Figure 5. Bimodal structures follow the same processing route as that of lamellar structure. Figure 6 shows an example of a bimodal microstructure.

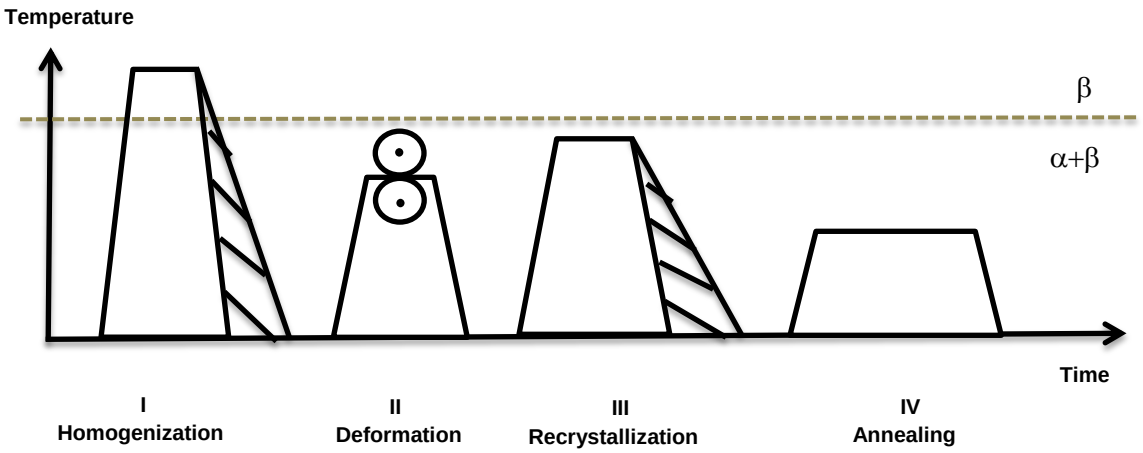

Figure 5: Processing route for bimodal structure [based from ref. 17]

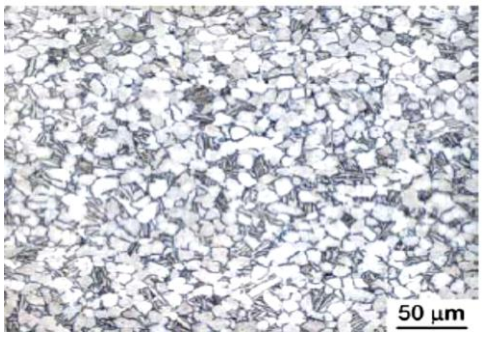

Figure 6: Bimodal Microstructure [18]

Cooling rate from the homogenization temperature is a critical factor, which determines the width of α-lamellae, which are deformed in the consecutive steps. The

deformation step is the one where in the deformation should be high enough such that some amount of energy is stored for recrystallization to take place. In the recrystallization step temperature plays an important role, which determines the position of recrystallized α in β grains. As long as there is enough time for the growth of α grains annealing time doesn't play an important role. In bimodal structures cooling rate in the annealing stage influences the growth of α lamellae but α colony size is determined by β grain size.

2.3.3 Fully Equiaxed Structure

Fully equiaxed microstructures in titanium alloys can be obtained in two different ways. In the first case, the process is almost similar to the bimodal structure upto the recrystallization step. When the cooling rate in the recrystallization step is slow enough then α grains will grow and there are no α lamellae in the β grains there by forming a fully equiaxed microstructure [16]. Figure 7 shows the processing route for this process [17].

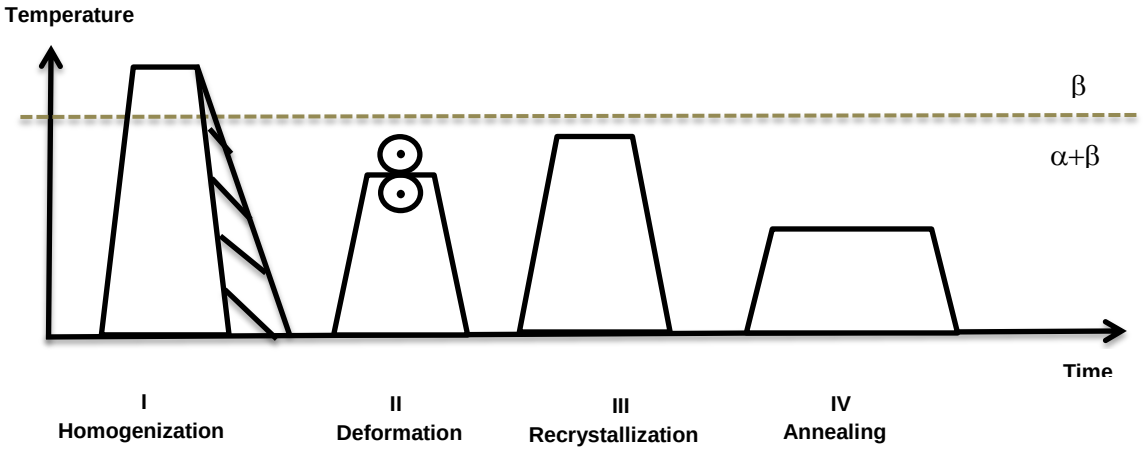

Figure 7 : Processing sequence for fully equiaxed microstructure [based from ref. 17]

Second way of producing a fully equiaxed microstructure is by recrystallising at a very low temperature such that an equillibrium volume fraction of α phase is formed from the deformed lamellar structure there by forming an equiaxed microstructure [16]. Using this process, smaller α grains can be obtained than compared to the previous process. By using the second process, at 800^{o}C on Ti-6Al-4V a fully equiaxed microstructure was obtained [18]. Figure 8 shows the processing route for the second process [17].

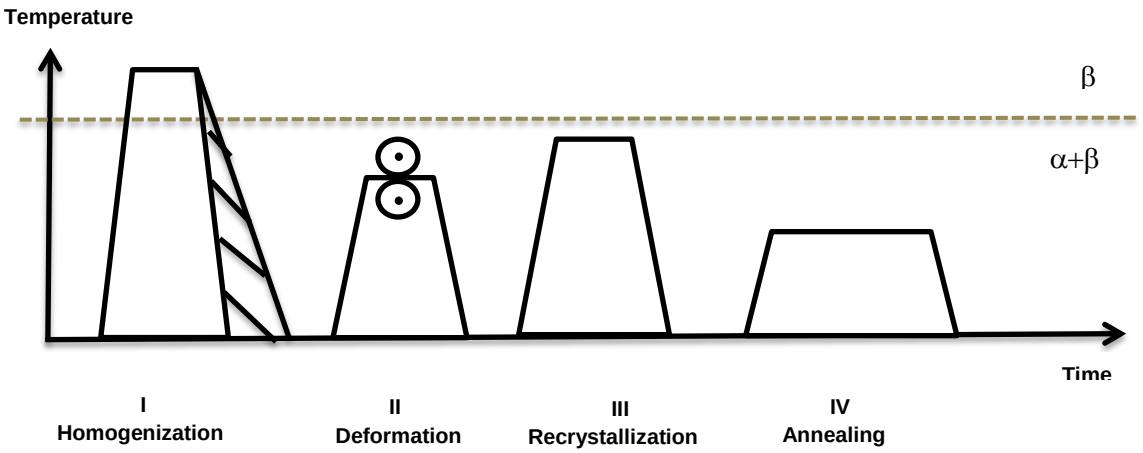

Figure 8 : Processing sequence for other route of producing fully equiaxed microstructure [based from ref. 17]

The important factors to be considered by both the process are the cooling rate in the homogenization step determines the size of α lamellae. The cooling rate in the recrystallisation step should be slow and the recrystallisation annealing temperature should be low. Both of these help in achieving a fully equiaxed microstructure [20].

Fully equiaxed microstructures can be changed to bi-modal structures by heating the material high in the α+β phase field and there by allowing it to cool at a faster rate such that a lamellae are formed in the beta matrix and a vice-versa can also be done

where in bi-modal structure is heated in the α+β field so that all the a recrystallises into β grains and cooling the material at a slow rate [17].

Figure 9 shows an equiaxed microstructure.

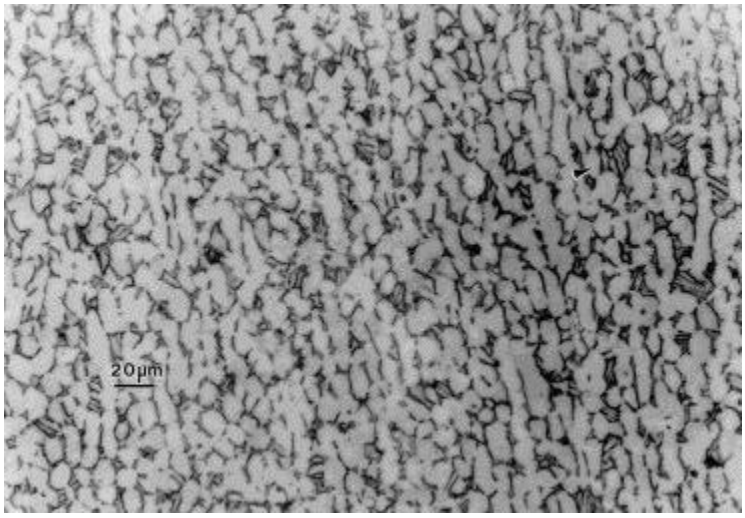

Figure 9: Equiaxed Microstructure [19]

Chapter 3

Material and Experimental Setup

3.1 Material

For this research, Ti-6Al-4V alloy with four different processing histories were used. The materials were provided by RTI-International Metals Inc., Niles, OH. The composition of all the alloys is given in Table 3. The alloys were initially processed either above the β transus in the β phase or below the β transus in the α+β range. The alloys were then hot isostatically pressed (HIPed) at 940^{o}C at a pressure of 103.42 MPa (15ksi) for four hours. The processing histories were:

- Alloy PH 3-1 preHIP
- Alloy PH 3-2 preHIP
- Alloy 3-1 HIPed
- Alloy 3-2 HIPed

Table 3: Chemical Composition of the materials used for experiments

	Al	V	Fe	C	O	H_2 (ppm)	N	Ti
Ti-6Al-4V	5.84	3.85	0.23	0.032	0.12	7.5	0.005	Balance

The thermo-mechanical processing route followed for the alloys can be seen in Figure 10. The left of the figure shows the processing of the α+β forged materials which is the same for pre HIPed and the post HIPed materials, the right side of the figure denotes the processing for the pre and post HIPed β processed materials. Compression test samples having dimensions of 32 mm in length and 16 mm in diameter were extracted from the billet. Figure 11 shows the un-deformed samples. Microstructures of the as received material can be seen in Figure 12.

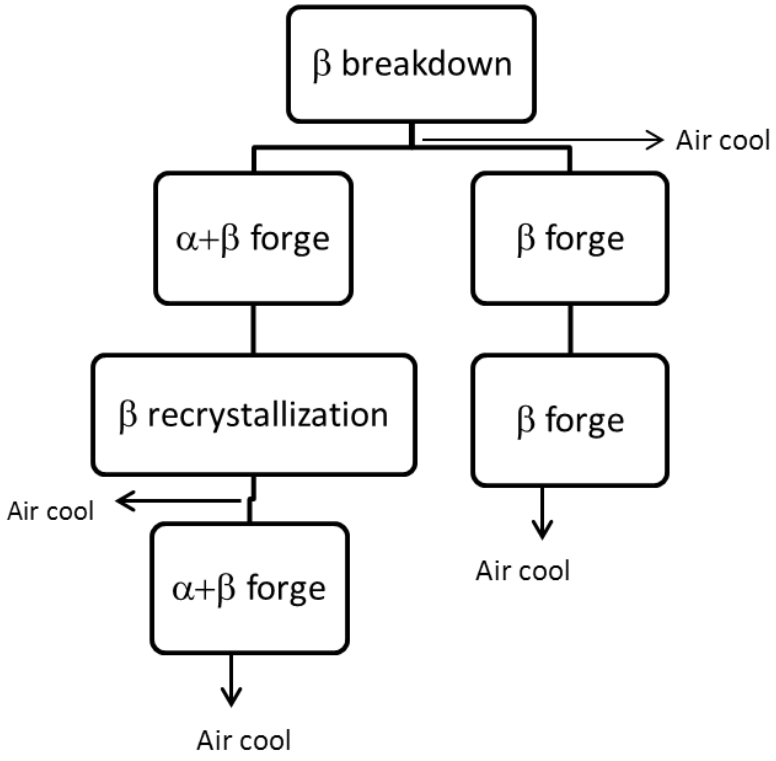

Figure 10 : Thermo mechanical processing routes

A closer look at the starting microstructures shows that all of the materials have distinctive microstructures which are due to the different themo-mechnical processing routes the material is processed through.

From the microstructures of the undeformed samples it is seen that the α+β processed material had an initial microstructure of kinked lamellae (Figure 12 (a)) and when the material was subjected to hot isostatic pressing (HIP), the lamellae got coarser (Figure 12 (b)). The β processed material had a basket weave structure also known as Widdmanstatten structure (Figure 12 (c)), after the HIP was done to this material the lamellae got coarser (Figure 12 (d)) since the process of HIP is a kind of annealing treatment given to the material.

The difference between α+β processing and β processing is that for α+β processed material most of the working on the alloy is done below the β transus temperature and the resulting microstructure is always a combination of both the α and β phases and the amount of each individual phase present is a function of forging temperature. On the other hand β processing is a technique in which the alloy is always deformed above the beta transus temperature [2].

The yield strength of a β processed alloy is lower than that of a α+β processed alloy but the tensile strength and fracture toughness of β processed alloy are greater than that of a α+β processed alloy [21].

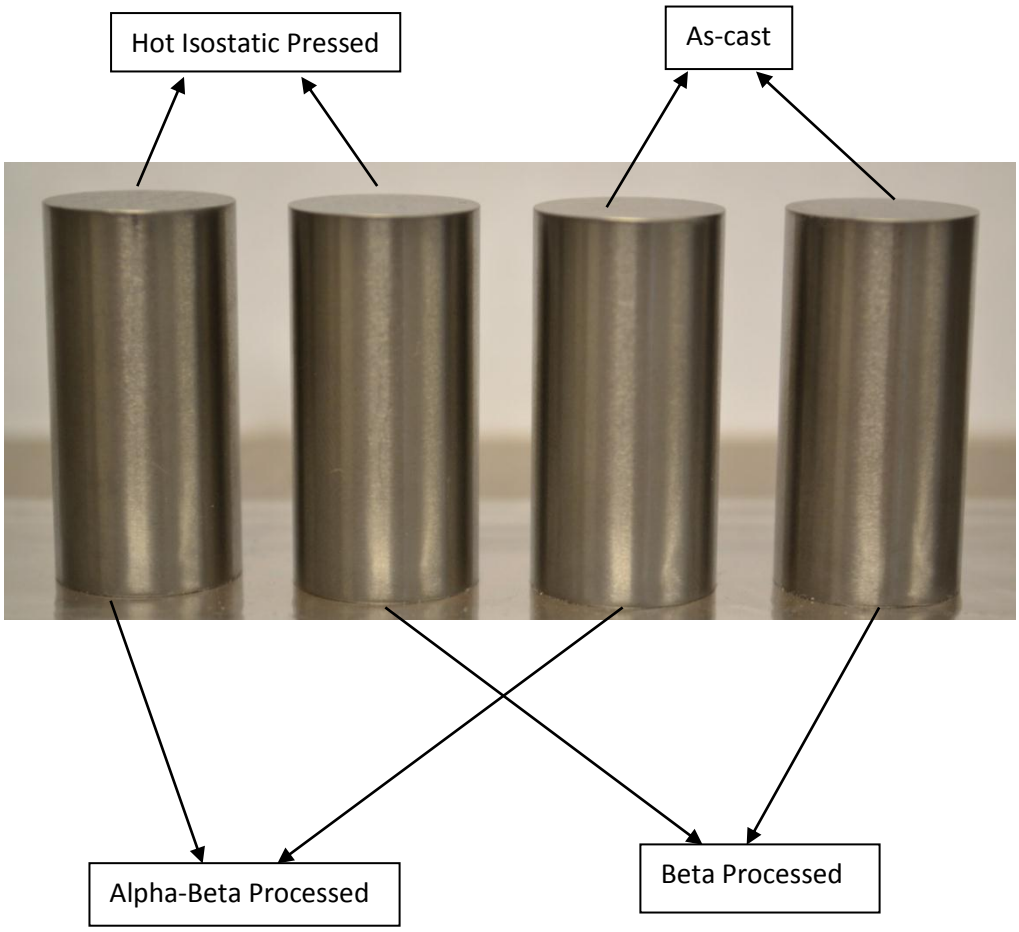

Figure 11: Undeformed Samples

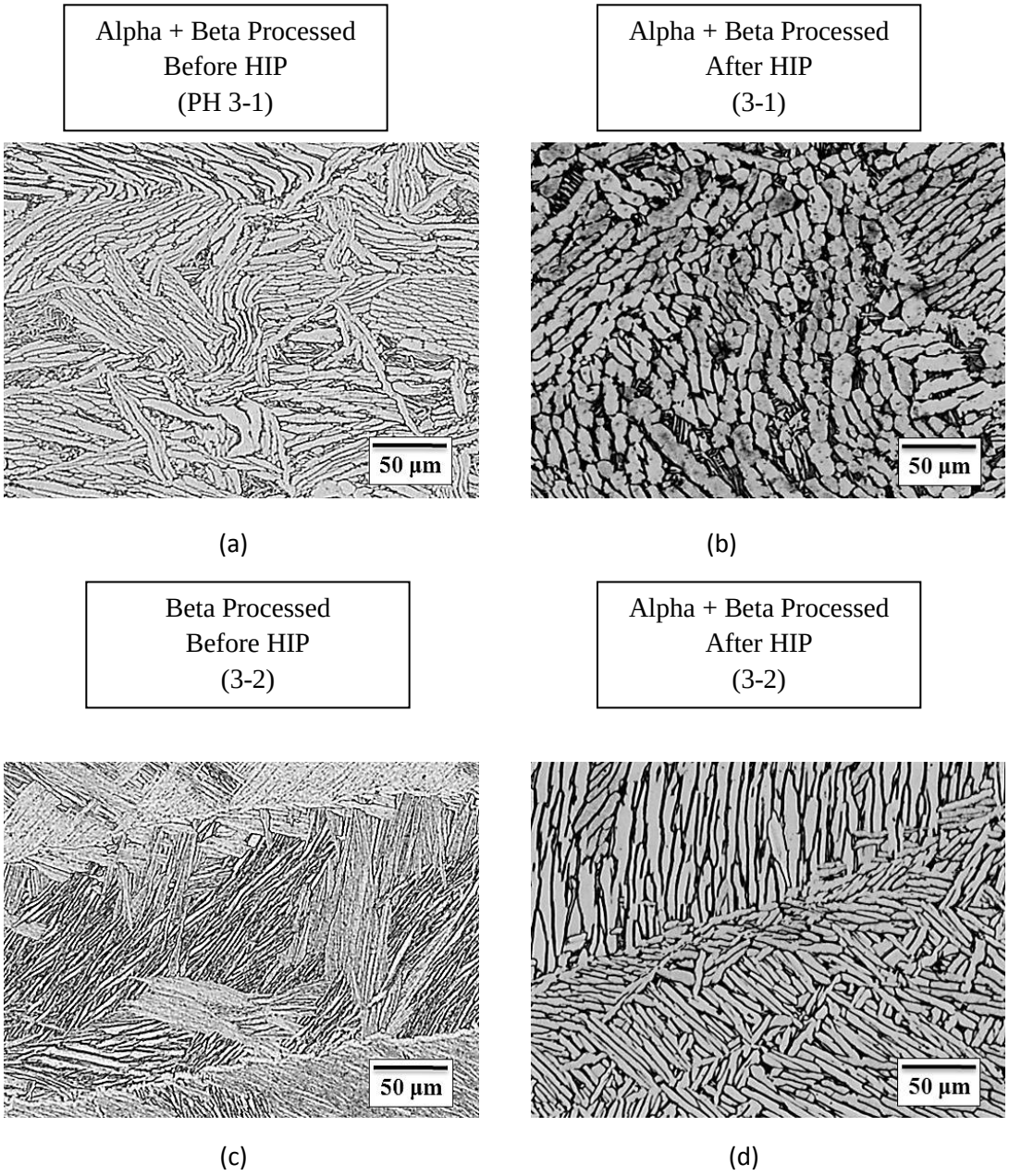

Figure 12 : Microstructures of Undeformed Samples (Microstructures provided by Dr. B. Cherukuri, RTI Intl. Niles, OH)

3.2 Experimental Determination of Flow Stress

Isothermal constant strain rate testing of the materials was done at different temperatures of 829^{o}C, 885^{o}C, 941^{o}C and 996^{o}C (1525^{o}F, 1625^{o}F, 1725^{o}F & 1825^{o}F) and at strain rates of 10^{-2} s^{-1}, 10^{-1} s^{-1} and 10^{0} s^{-1}.

3.2.1 Test Facility

The test facility at Wright State University consists of a servo-hydraulic test machine, which is controlled via a computer. The test frame consists of a heating element controlled atmospheric radiant furnace with a tungsten mesh surrounded by water-cooled copper jackets. A high vacuum chamber surrounds the heating setup connected to the mechanical and diffusion pumps. High vacuum levels to the order of 10^{-5} torr were reached during the testing of the samples. Two load cells with a capacity of 200 Kip and 20 Kip (890 kN and 89kN) are available and most of the tests were performed using the 200 Kip load cell. The test frame was also capable of attaining a wide range of strain rates ranging from 10^{-4} s^{-1} to 10 s^{-1}.

3.2.2 Load – Stroke Data Acquisition

The MTS test frame was connected to a computer controller, which would collect the load and displacement signals, and then the load v/s extension data was used to obtain the true stress v/s true strain curves (flow curves).

3.2.3 Tooling

The push rods used for the compression testing of the samples used in this study were made of a molybdenum alloy TZM, which can be used up to a temperature of 1250^{o}C. Other materials can also be used as tooling material depending on the temperature and strain rate requirements.

3.3 Testing Procedure

3.3.1 Calibration of Furnace

Before the compression testing of the samples, the furnace had to be calibrated in order to ensure that the testing was done at appropriate temperatures. The following procedure shows how the calibration was done.

A cylindrical test specimen with dimensions of 32mm in length and 16mm in diameter was chosen for the calibration of the furnace. A 1.6mm (1/16 in) diameter hole of about 8mm in depth was drilled at mid height of the specimen into which a Type K thermocouple was inserted. The other end of the thermocouple was connected to a digital display and another thermocouple was used to record the temperature inside the furnace and the end of this thermocouple was connected to an analog display. The specimen was placed between the push rods and a small load of 500N was applied. The reason for this was to hold the sample and thermocouple in place. The specimen was then heated to set point temperature while a constant load was being applied to the specimen. The same procedure was carried out for various set points and a regression fit between specimen temperature and furnace set point temperature was obtained. The regression coefficient r

> 0.999 indicated it is possible to control the specimen temperature to an accuracy of less than $\pm 5^{o}C$ over the test temperature range. Figure 13 shows the calibration curve done for this study.

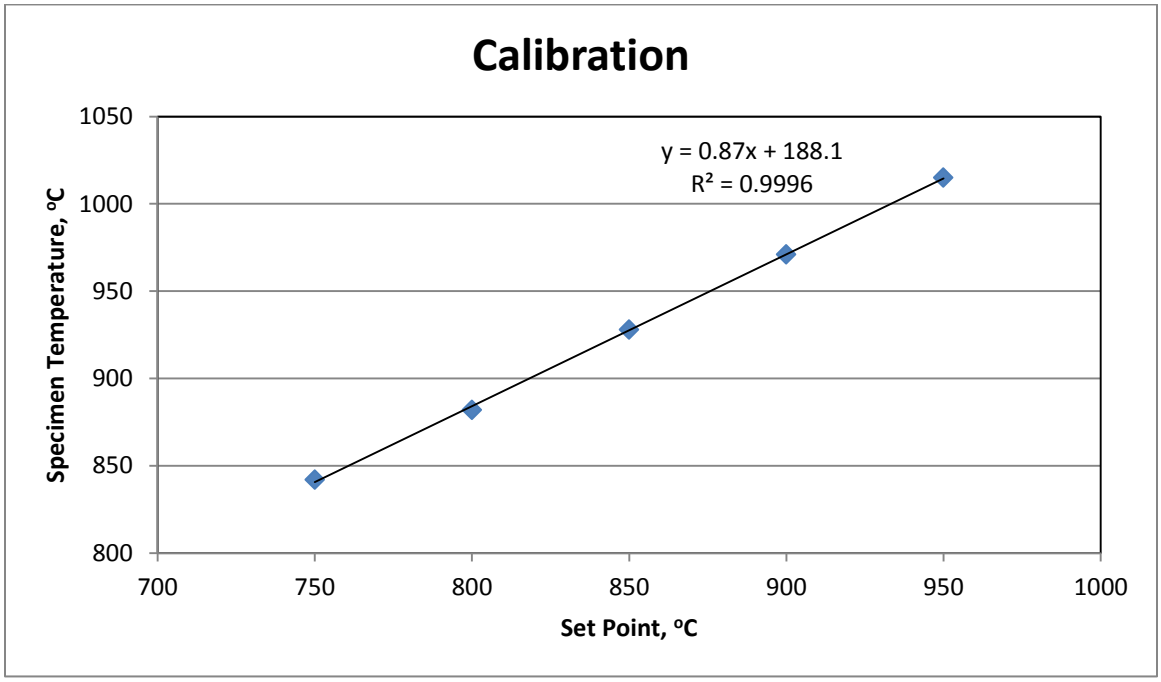

Figure 13: Calibration Curve

The calibration was good for a given tooling and temperature range and if any of the parameters was changed then the whole calibration would have to be carried out again.

3.3.2 Compression Testing

The test specimens and the tooling were coated with a high temperature graphite based lubricant that would lower the friction between the tooling surface and the test specimen.

The specimen was loaded and the furnace was evacuated to a pressure of 10^{-5} torr. The specimen was then heated to the test temperature in vacuum and was allowed to soak at the desired test temperature for a period of 15 minutes. A signal from the computer will take the length of the specimen and then move the actuator exponentially to maintain a constant strain rate. After the specimen is deformed the heating elements are switched off and high purity helium is let into the furnace to cool the sample and as well as the tooling. Once the furnace temperature reaches below 50^{o}C the sample is removed. For the tests with strain rates of 0.1 s^{-1} and 1 s^{-1}, the furnace was switched off prior to the testing to get rid of the noise from the furnace controller but for the slow speed test having a strain rate of 0.01 s^{-1}, the furnace was switched off after the testing was completed.

Load stroke data collected from the computer were converted to true stress – true strain plots (flow curves). All the tests in this study were conducted for a 50% reduction in height, which resulted in a final strain of 0.693. All the flow curves were corrected for deformation heating.

3.4 Metallographic Study

Metallographic study was performed to study the effect of deformation patterns such as temperature and strain rate on the microstructure of the specimen. Standard metallographic techniques such as sectioning, mounting, grinding, polishing and etching were performed on the as received and as well as the deformed specimens and a Kroll's reagent (92ml Distilled water, 6ml HNO_3, 2ml HF) was used as an etchant to reveal the microstructure for an etching time of 20 seconds.

Chapter 4

Results and Discussions

4.1 Flow Curve Analysis

The load versus elongation curves obtained from the compression tests were converted into true stress – true strain curves (flow curves). All the flow curves obtained were corrected for deformation heating. The temperature rise due to deformation heating can be calculated using equation below:

$$\Delta T = \frac{\eta\, 0.95 \int \sigma\, d\epsilon}{\rho\, Cp}$$

where ΔT is the temperature rise, η is the strain rate correction factor, $\int \sigma\, d\varepsilon$ is the area under the stress strain curve (work of deformation per unit volume), ρ is the density of the material and C_p is the specific heat (ρC_p is the heat capacity of the material) [22]. Percentage of deformation work converted to heat is often assumed as 95% and hence a factor of 0.95 has been used. The value η is governed by the strain rate and the value varies between 0 and 1. For strain rates $\geq 10^0$ s^{-1} the value of η is 1, since most of the energy is converted into heat and for strain rates $\leq 10^{-3}$ s^{-1} the value of η is 0, since most of the energy is dissipated into surroundings. In this study for a strain rate of 10^{-2} s^{-1} the value of η = 0.333, for 10^{-1} s^{-1} the value of η = 0.666 and for a strain rate of 10^0 s^{-1} the value of η = 1 [23].

A plot of log (True Stress) versus temperature (Kelvin) was done after the temperature correction was done and this resulted in obtaining the corrected stress values and as expected the temperature rise in the sample tested at lowest temperature and at the highest strain rate was the highest.

The corrected flow curves were used for constitutive modeling and for finite element (FE) modeling of the compression test.

The shape of a flow curve can be used to predict different microstructural conditions. For example if the flow curve shows an initial peak stress and then a gradual decrease in the stress value then such kind of a curve implies that there is some flow softening taking in the material and if the flow curve has an oscillatory kind of pattern then it exhibits a dynamic recrystallization [16].

Uncorrected flow curves of HIPed (3-1) and pre HIPed (PH 3-1) $\alpha+\beta$ processed alloys at different strain rates and temperatures are shown in Figures 14 to 19.

Observations made from the $\alpha+\beta$ processed (3-1 and PH 3-1) flow curves were:

1. At slower strain rate of 0.01 s^{-1} and at all the temperatures, the flow curves show a steady-state type behavior.
2. At faster strain rates of 0.1 s^{-1} and 1 s^{-1} the samples which were tested below beta transus (829^{o}C & 885^{0}C) showed a peak stress at a low strain followed by rapid flow softening whereas samples tested above and near beta transus (940^{o}C & 996^{o}C) show a peak stress followed by a steady state deformation.

Note: For the tests performed at temperatures of 829^{o}C and 885^{o}C had a problem and hence some variance can be seen in the plots. Due to unavailability of the samples the tests could not be repeated.

The uncorrected flow curves of HIPed (3-2) and pre HIPed (PH 3-2) β processed alloys at different temperatures and strain rates are shown in Figures 20 to 25.

Observation made from the β processed (3-2 and PH 3-2) flow curves were:

- At all strain rates the samples tested below the beta transus (829^{o}C & 885^{o}C), showed a peak stress followed by rapid flow softening and for samples tested near and above beta transus (940^{o}C & 996^{o}C), showed a peak stress followed by gradual flow softening.

Figure 26 and Figure 27 show the uncorrected and corrected true stress true strain plots at different temperatures and strain rates for α+β processed materials. The effect of adiabatic temperature is almost the same in all the samples except for the samples tested at low temperatures of 829^{o}C & 885^{o}C and at a strain rate of 10^{0} s^{-1}. For these two curves the HIPed sample shows strain hardening which means it has a peak stress at relatively low strain followed by gradual flow softening. The pre HIPed sample showed a gradual flow softening which is a characteristic of dynamic recrystallization.

Temperature un-corrected and corrected flow curves of β processed HIPed and pre HIPed curves can be seen in Figures 28 and 29. True stress true strain curves look the same at all temperatures and strain rates except for samples tested at 996^{o}C and at strain rates of 10^{-1} s^{-1} and 10^{-2} s^{-1}. The HIPed samples showed strain hardening whereas on the other hand the pre HIPed samples exhibited flow softening.

Overall analysis shows that there is a significant difference in the flow curves at different temperatures and strain rates. Both the α+β processed and β processed showed similar behavior where in the HIPed samples exhibited strain hardening and the pre HIPed samples showed flow softening.

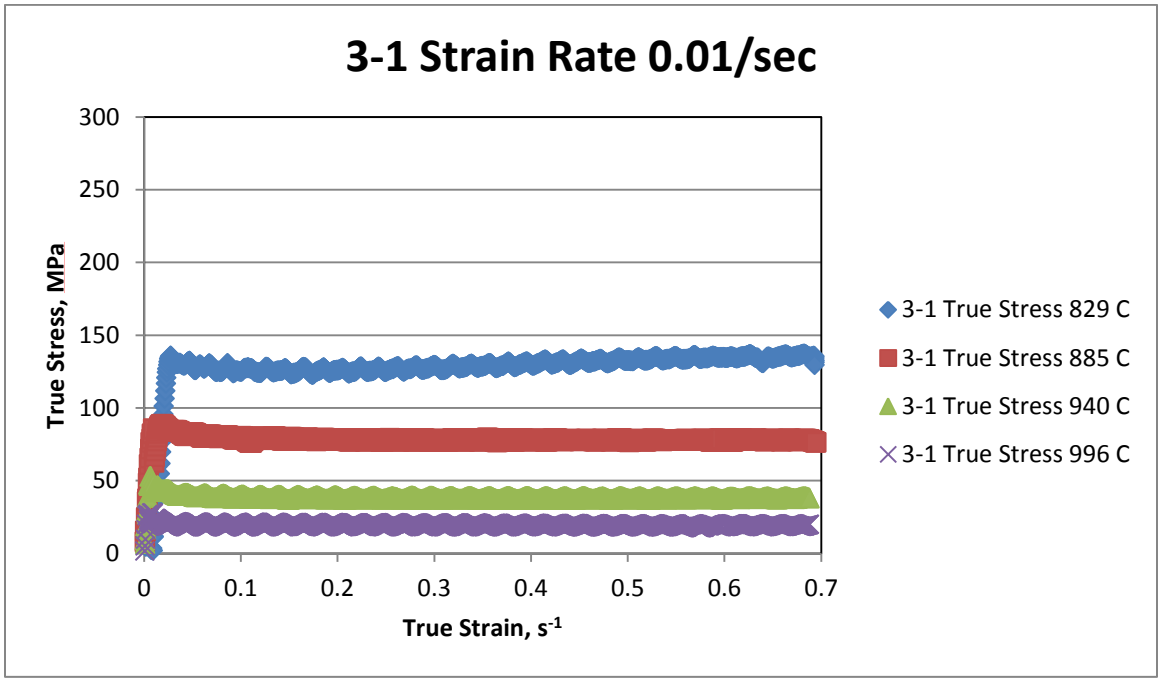

Figure 14: True stress - True strain curves for 3-1 at a strain rate of 10^{-2} s^{-1} and at different temperatures (uncorrected for deformation heating)

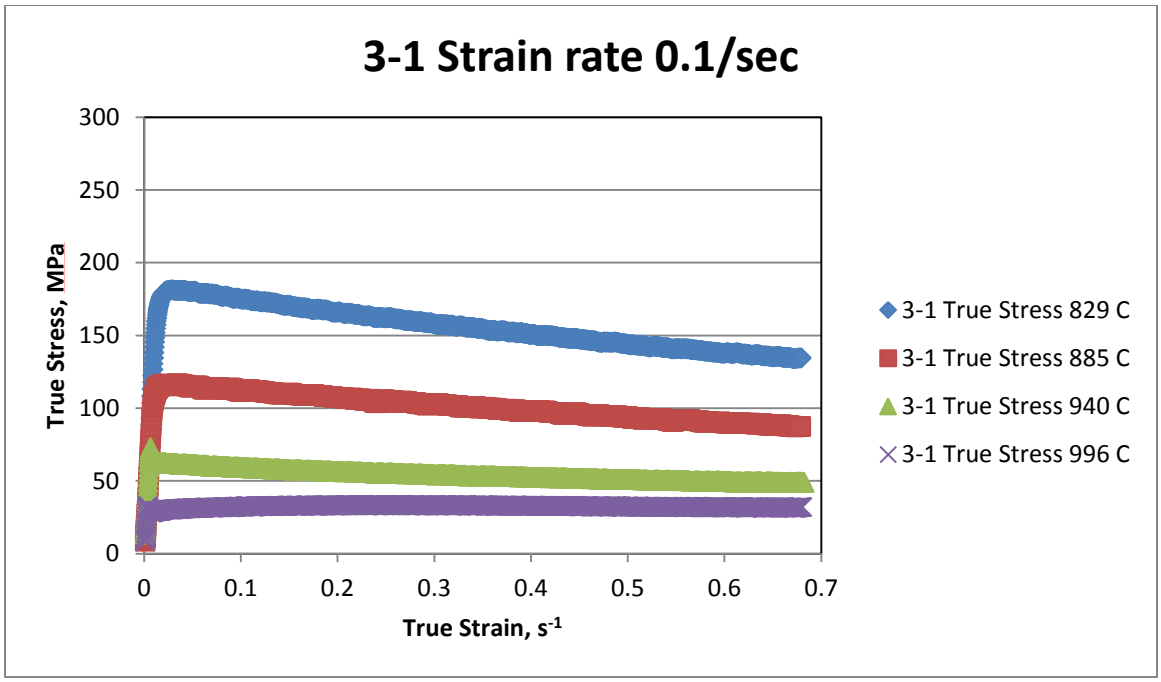

Figure 15: True stress - True strain curves for 3-1 at a strain rate of 10^{-1} s^{-1} and at different temperatures (uncorrected for deformation heating)

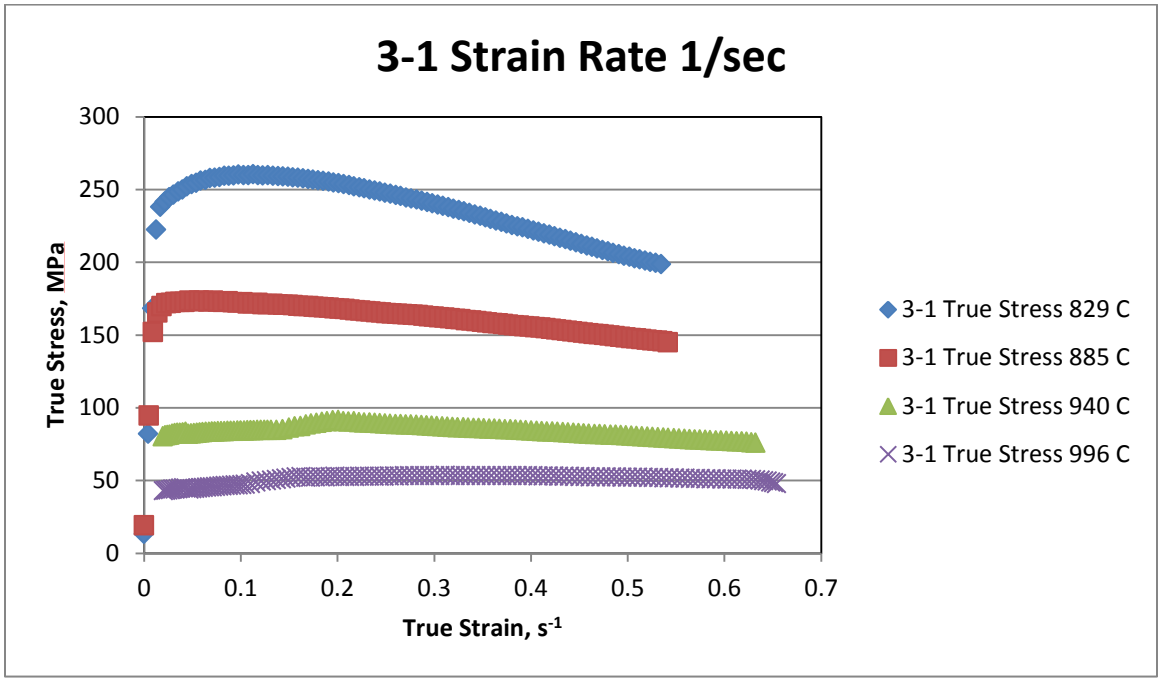

Figure 16: True stress - Trues strain curves for 3-1 at a strain rate of 10^{0} s^{-1} and at different temperatures (uncorrected for deformation heating)

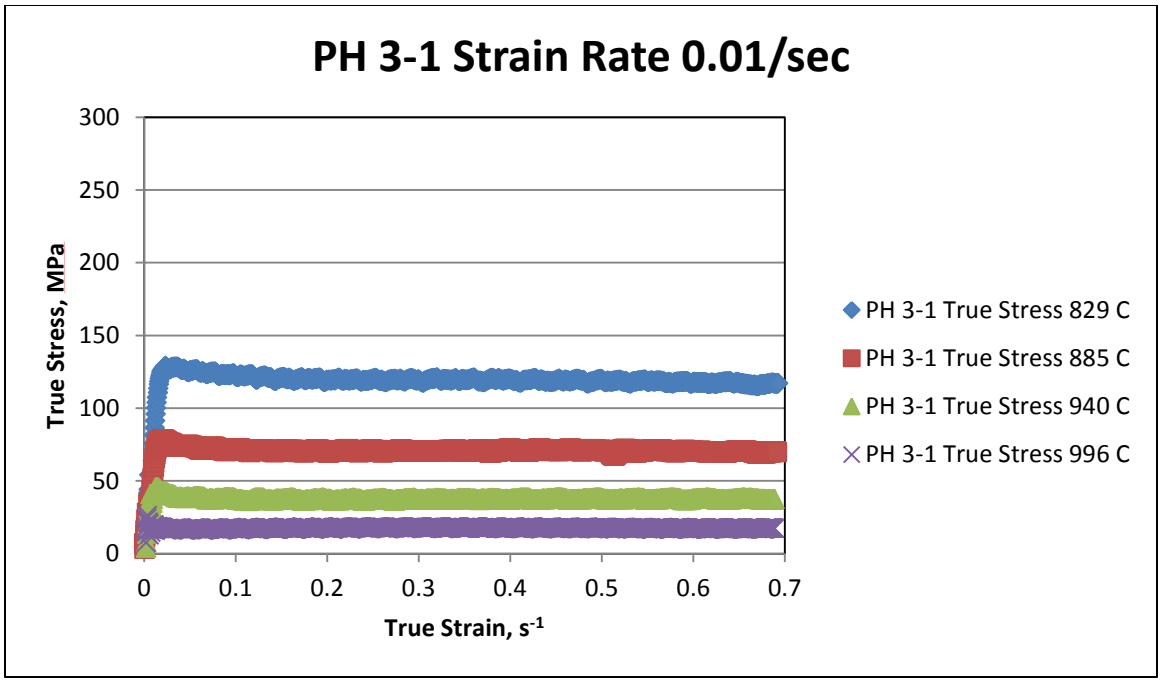

Figure 17: True stress - Trues strain curves for PH 3-1 at a strain rate of 10^{-2} s^{-1} and at different temperatures (uncorrected for deformation heating)

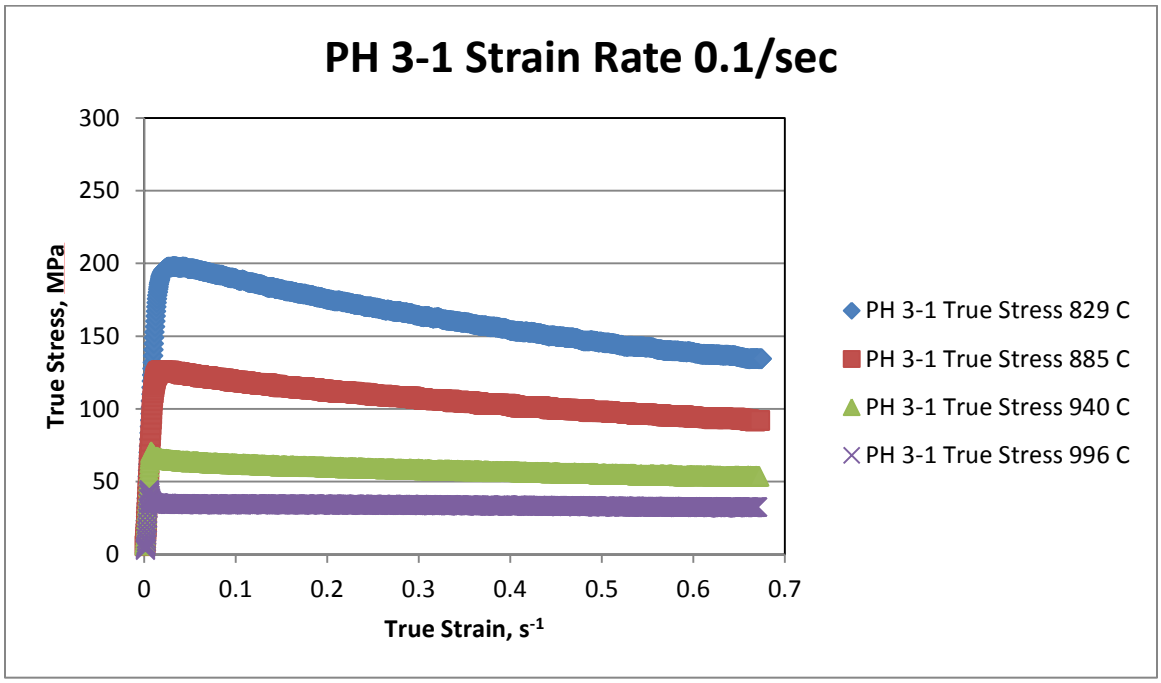

Figure 18: True stress - Trues strain curves for PH 3-1 at a strain rate of 10^{-1} s^{-1} and at different temperatures (uncorrected for deformation heating)

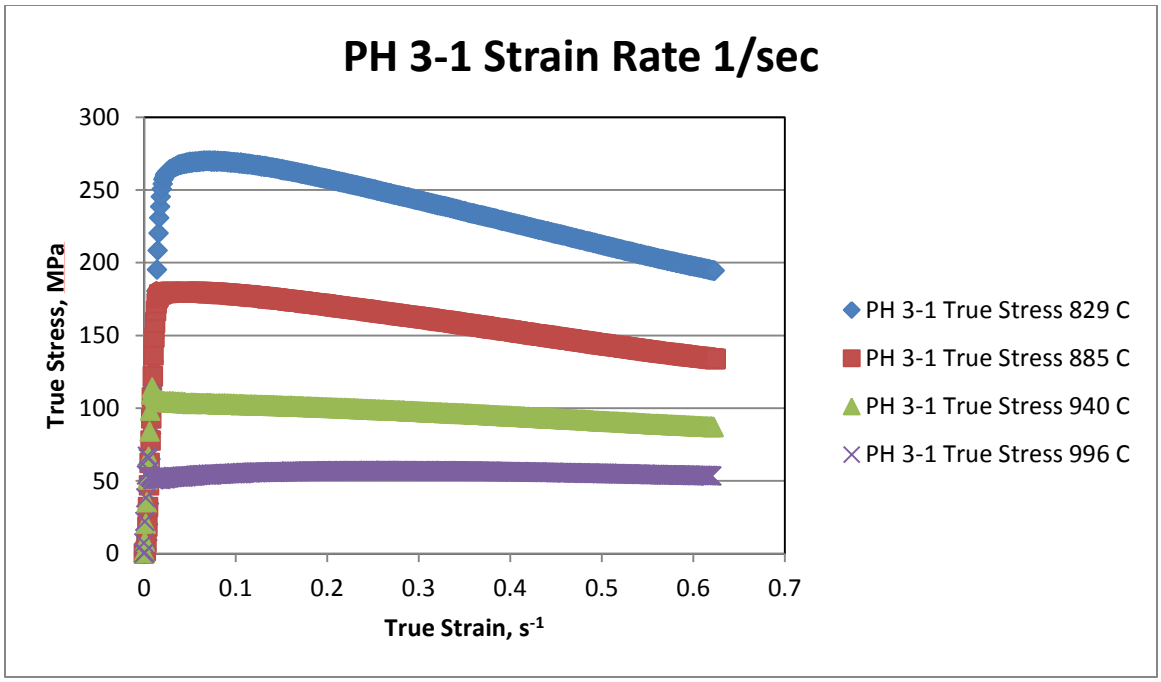

Figure 19: True stress - Trues strain curves for PH 3-1 at a strain rate of 10^0 s^{-1} and at different temperatures (uncorrected for deformation heating)

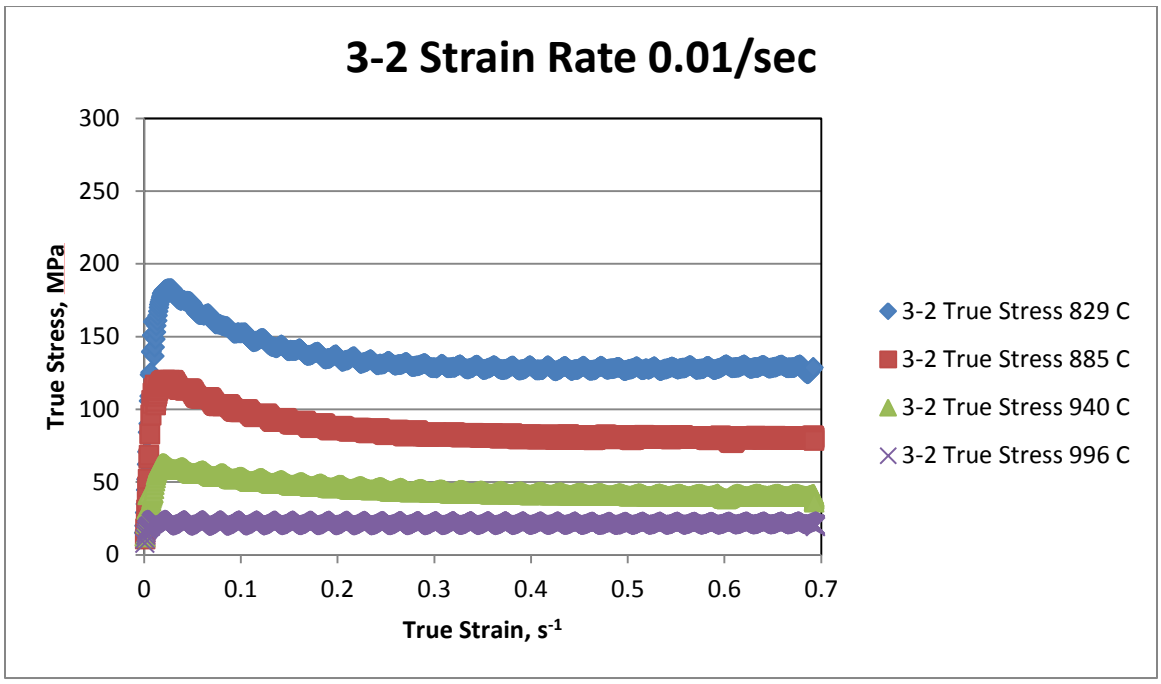

Figure 20: True stress - Trues strain curves for 3-2 at a strain rate of 10^{-2} s^{-1} and at different temperatures (uncorrected for deformation heating)

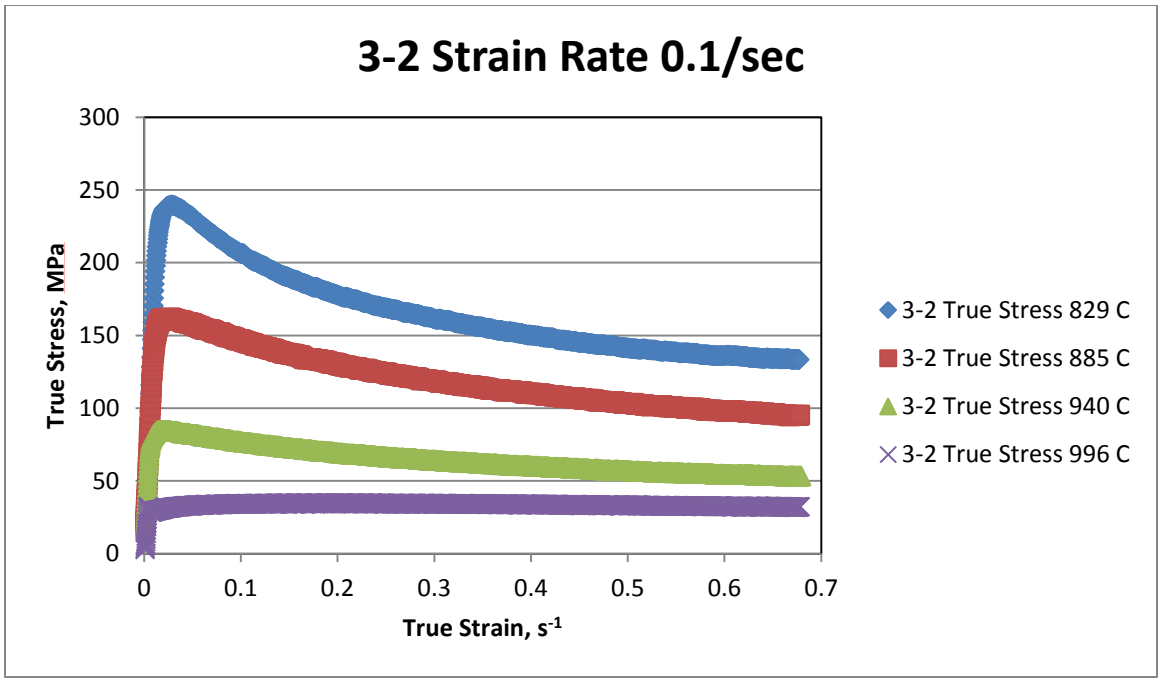

Figure 21: True stress - Trues strain curves for 3-2 at a strain rate of 10^{-1} s^{-1} and at different temperatures (uncorrected for deformation heating)

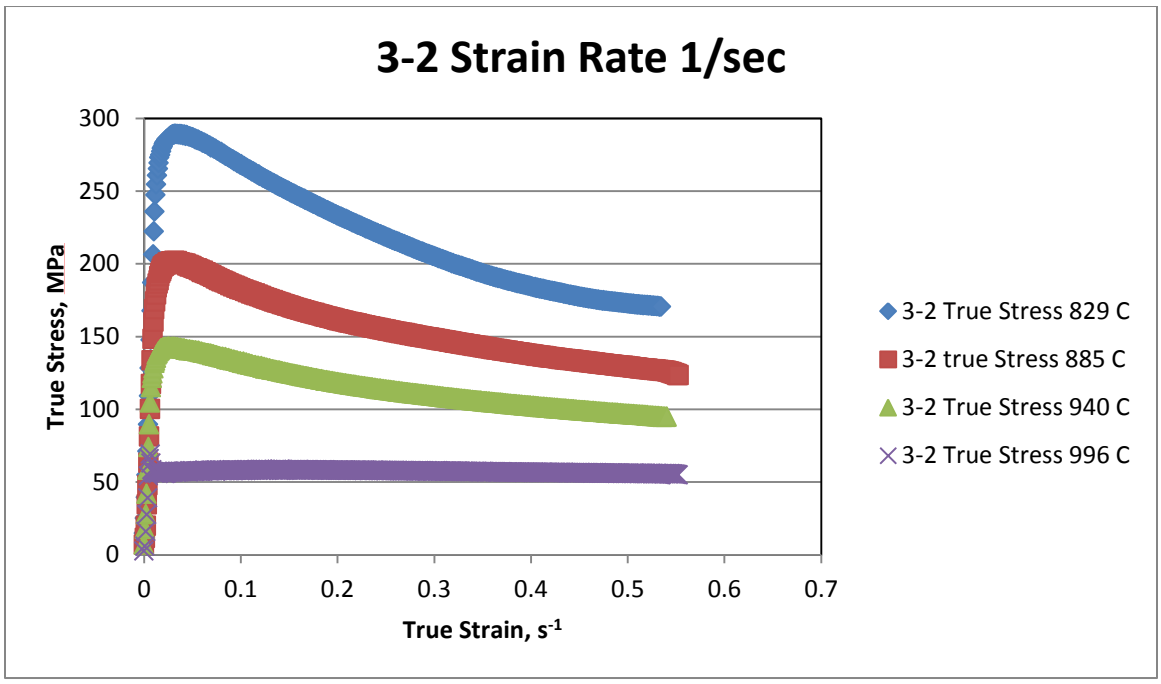

Figure 22 : True stress - Trues strain curves for 3-2 at a strain rate of 10^{0} s^{-1} and at different temperatures (uncorrected for deformation heating)

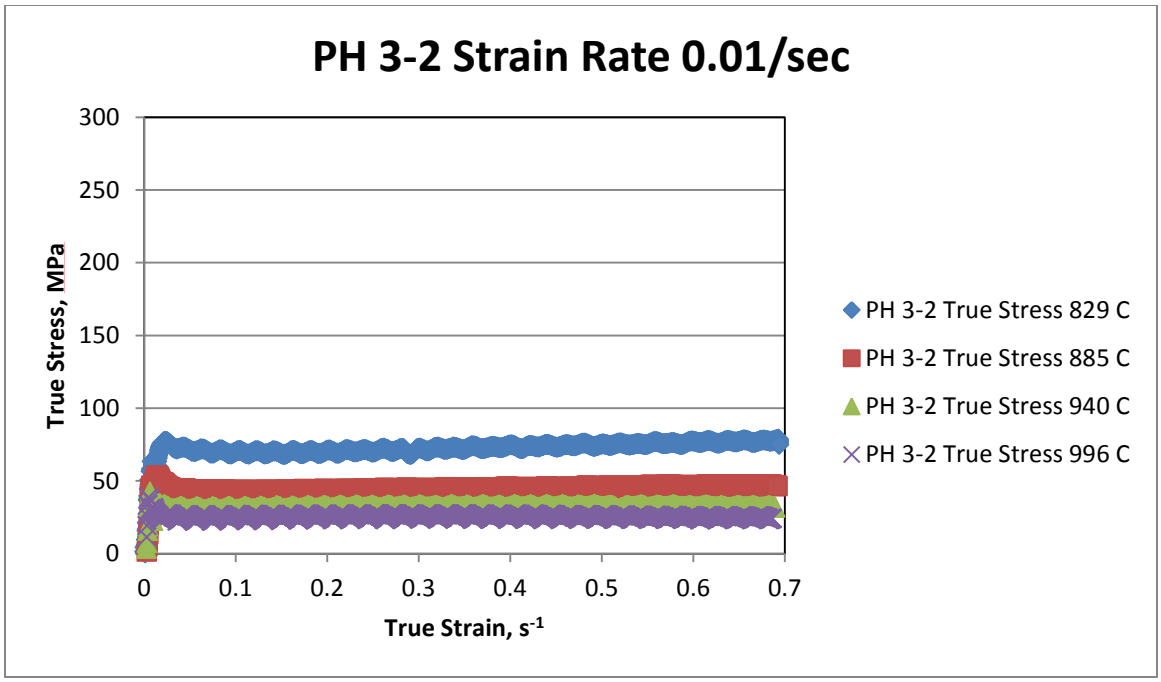

Figure 23: True stress - Trues strain curves for PH 3-2 at a strain rate of 10^{-2} s^{-1} and at different temperatures (uncorrected for deformation heating)

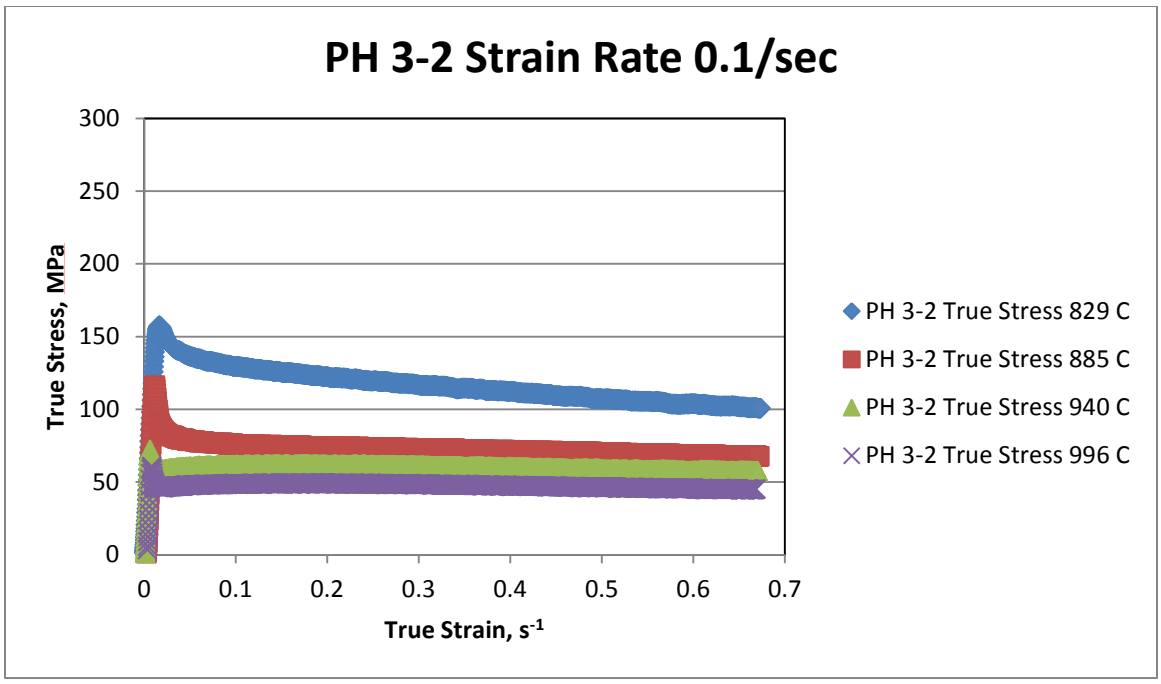

Figure 24: True stress - Trues strain curves for PH 3-2 at a strain rate of 10^{-2} s^{-1} and at different temperatures (uncorrected for deformation heating)

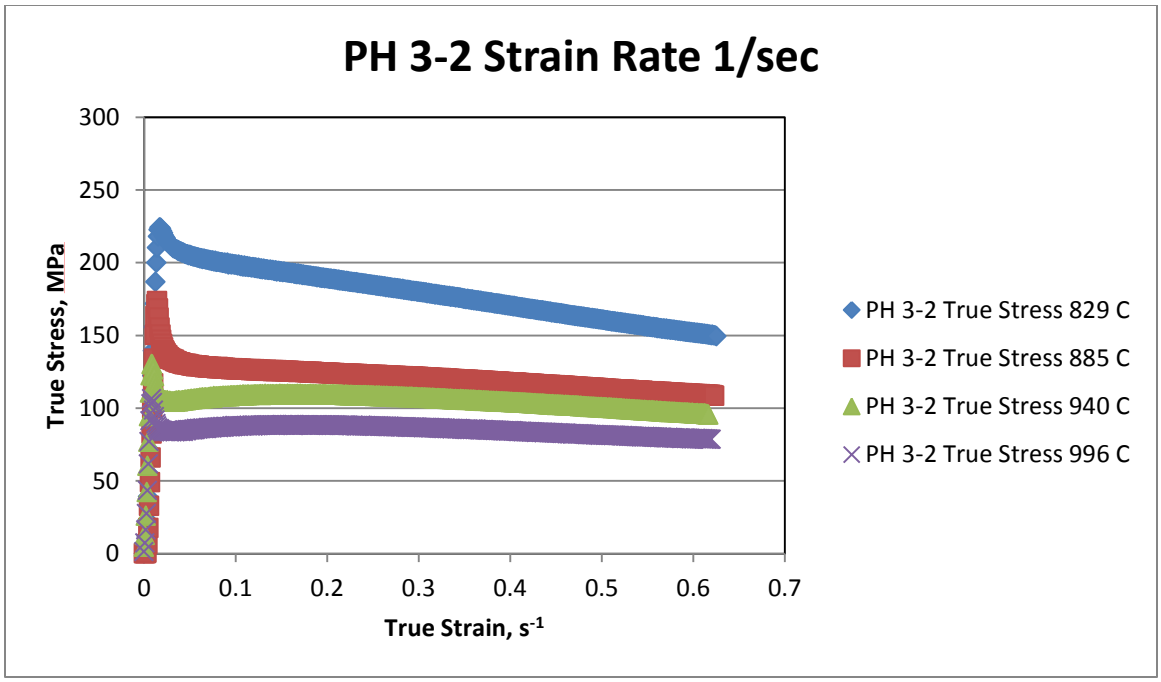

Figure 25: True stress - Trues strain curves for PH 3-2 at a strain rate of 10^0 s^{-1} and at different temperatures (uncorrected for deformation heating)

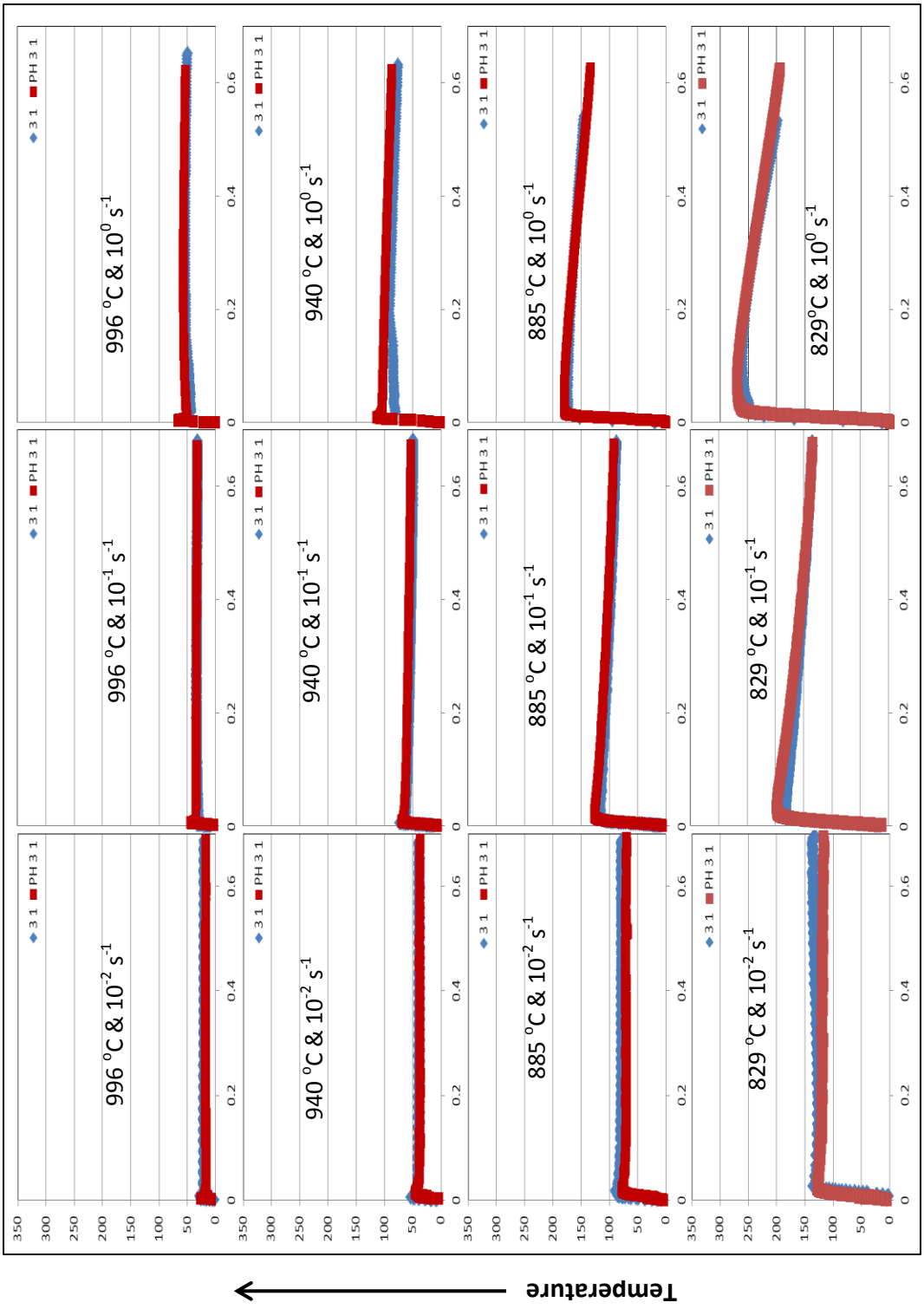

Note: X axis: True Strain, Y axis: True Stress in MPa, 3 1: HIPed alloy and PH 3 1: Pre HIPed alloy

Figure 26 : True stress - True Strain plots for 3-1 and PH 3-1 at different temperatures and strain rates (uncorrected for deformation heating)

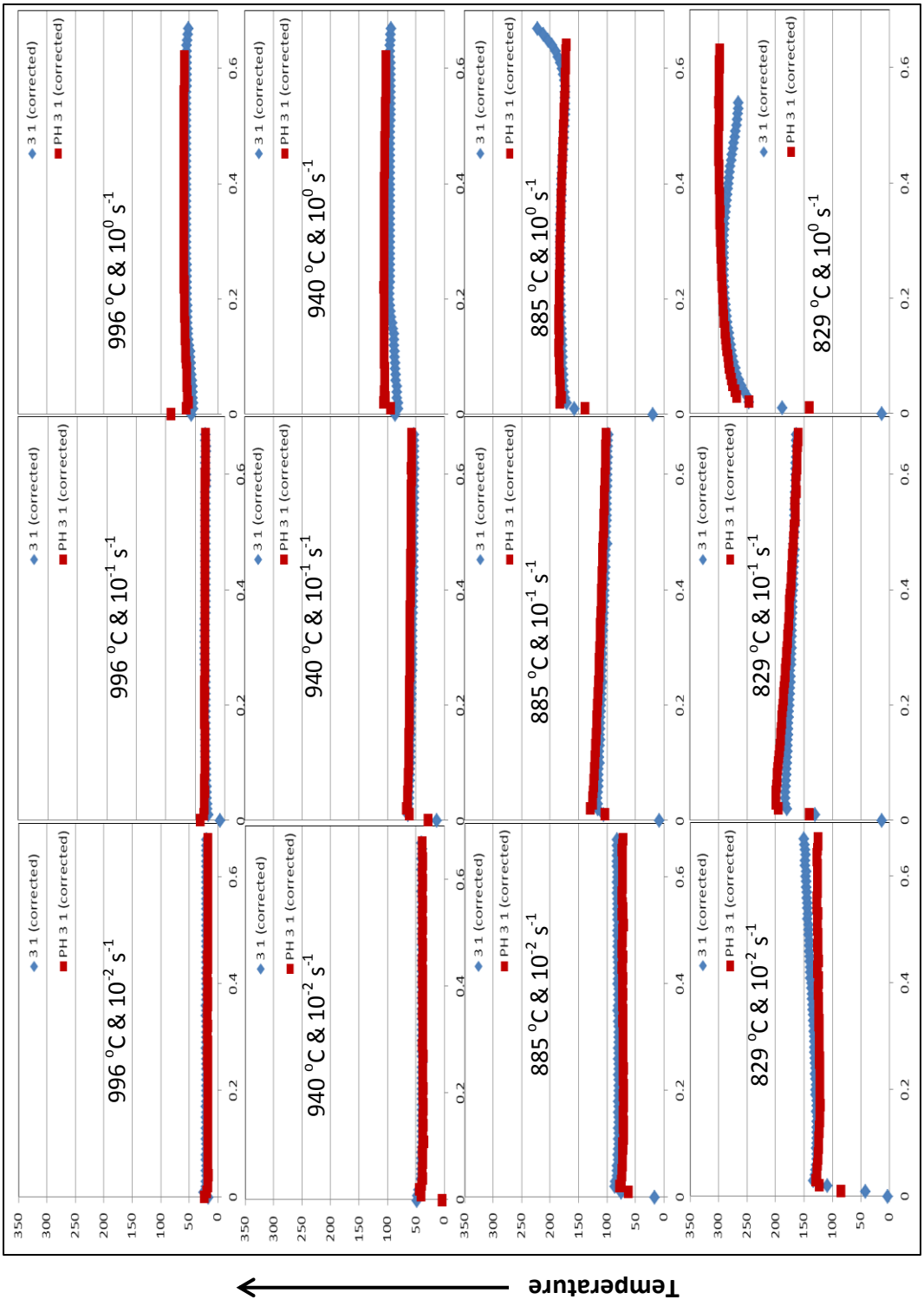

Figure 27: True stress - True Strain plots for 3-1 and PH 3-1 at different temperatures and strain rates (corrected for deformation heating)

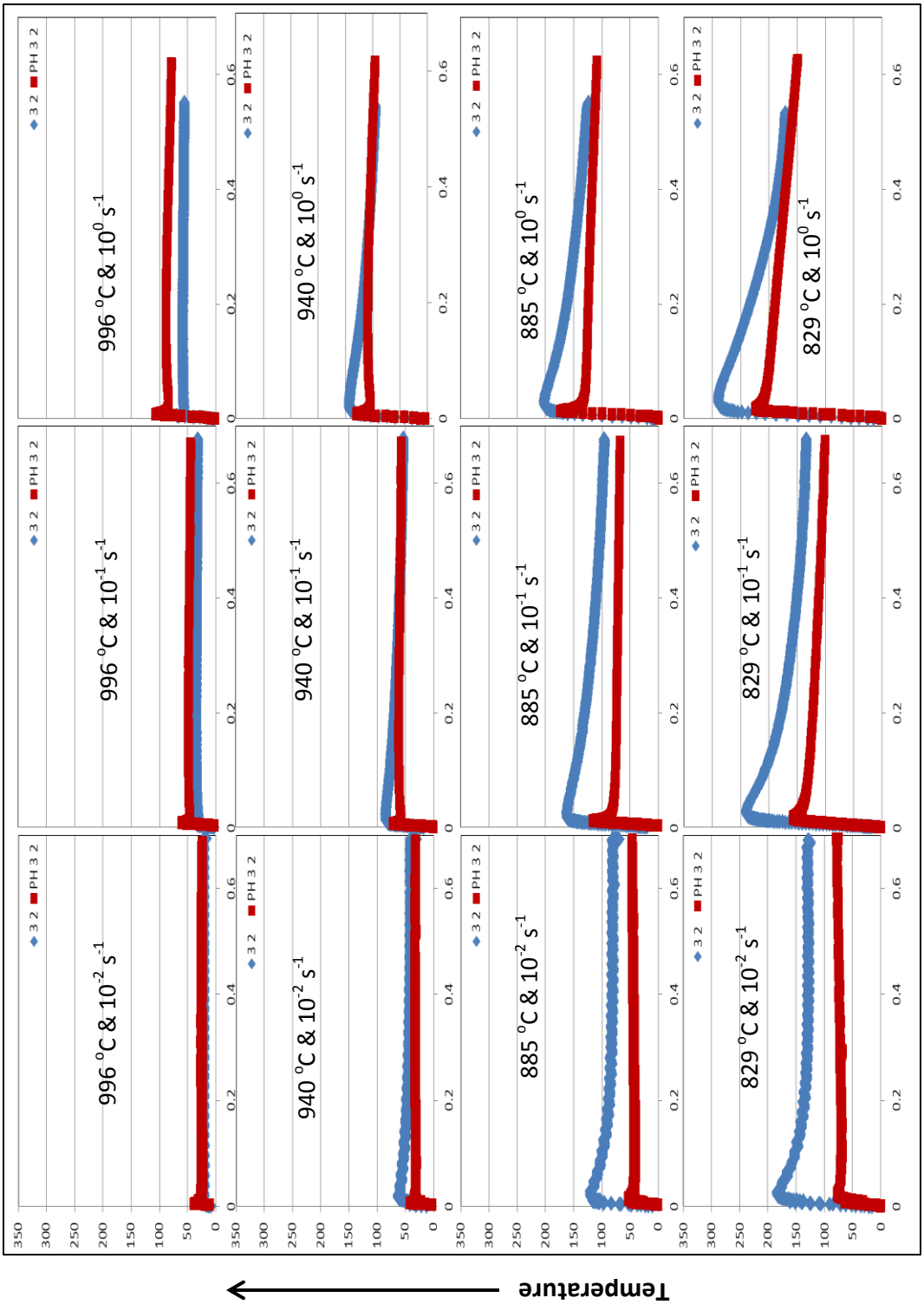

Figure 28: True stress - True strain plots for 3-2 and PH 3-2 at different temperatures and strain rates (uncorrected for deformation heating)

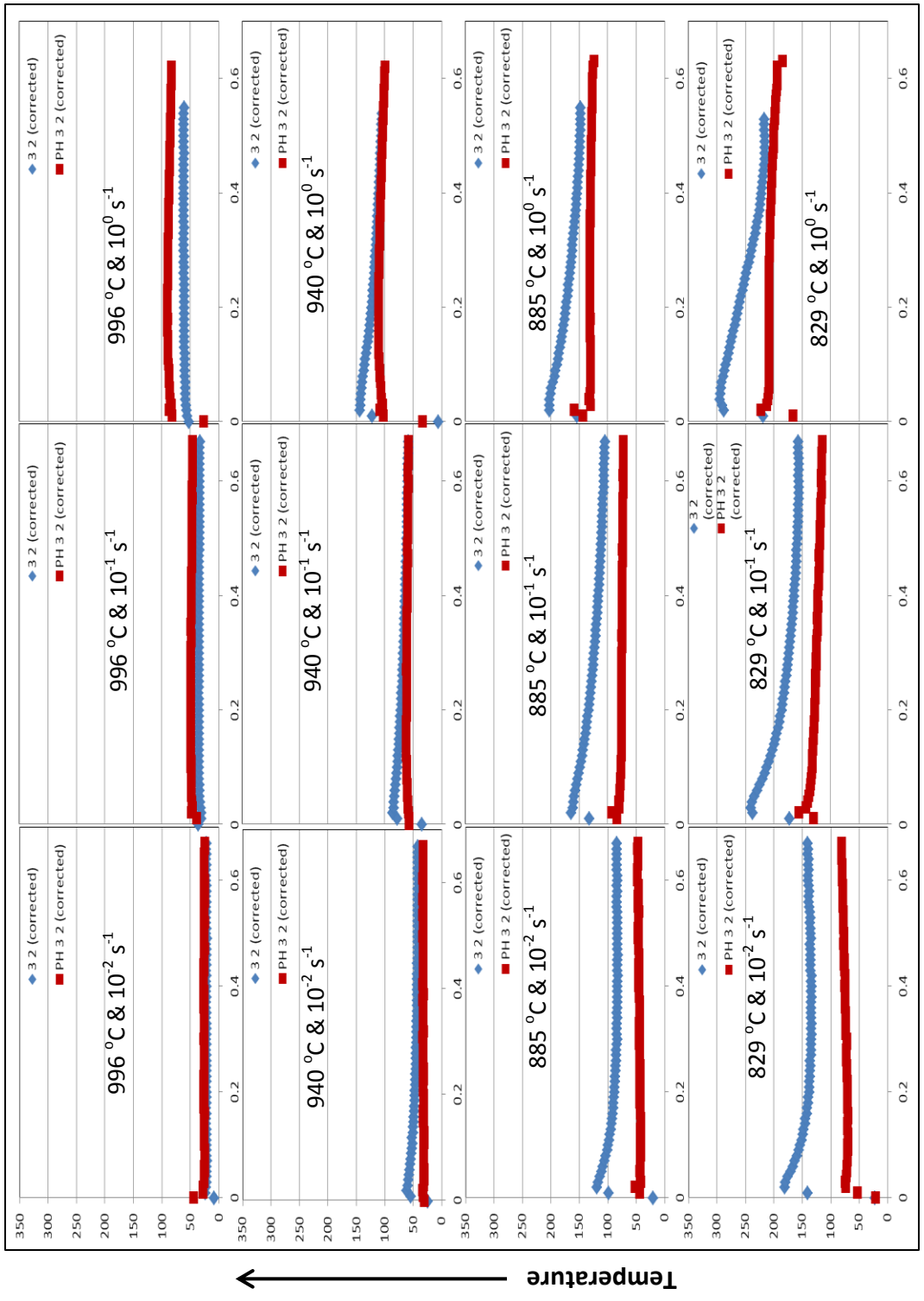

Figure 29: True stress - True strain plots for 3-2 and PH 3-2 at different temperatures and strain rate (Corrected for deformation heating)

4.2 Constitutive Modeling

To analyze the high temperature behavior of the HIPed and pre HIPed samples of the α+β processed and β processed alloys, the constant strain rate flow curves at four different temperatures of 829^{o}C, 885^{o}C, 940^{o}C and 996^{o}C were used. In order to do this study a true strain value of 0.1 was considered at this strain. The deformation heating was small under all deformation conditions. Figures 30 to 33 show a log – log plot of true stress versus true strain at each temperature for all the alloys. From the Figures 34 to 37 it is seen that all the alloys have a high value of flow stress at a low temperature's and high strain rates. The variation of flow stress with respect to strain rate at constant temperature and true strain value gives strain rate sensitivity (m) which can be represented as:

$$m = \left.\frac{\delta\,(\log(\sigma))}{\delta\,(\log(\dot{\epsilon}))}\right|_{T,\epsilon}$$

The value of m increases with increase in temperature and at a given temperature the value of m decreases as the strain rate increases. Table 4 shows average values of m for different alloys at different test temperatures used in this study.

Table 4: Average Strain rate sensitivity (m) values obtained from temperature corrected flow curves

Material / Temperature (^{o}C)	PH 3 1	3 1	PH 3 2	3 2
829	0.1793	0.1676	0.2249	0.1326
885	0.2024	0.1775	0.2486	0.1382
940	0.2220	0.1745	0.2697	0.2066
996	0.2606	0.194	0.2722	0.2191

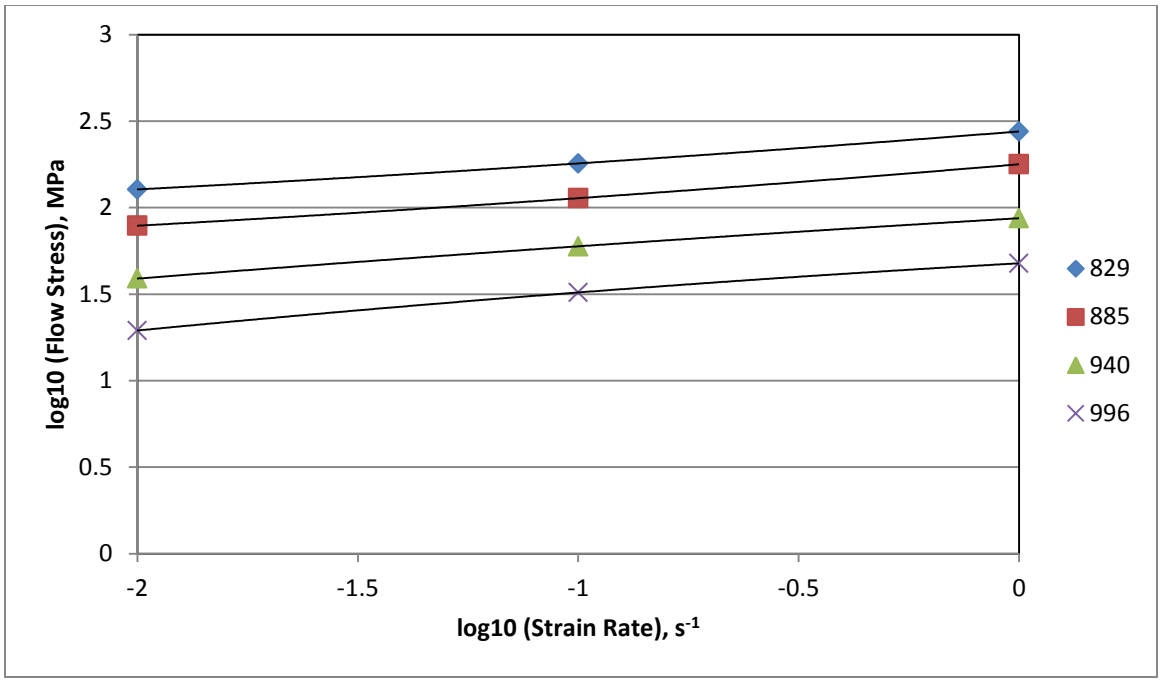

Figure 30: Variation of flow stress at different temperatures for 3-1

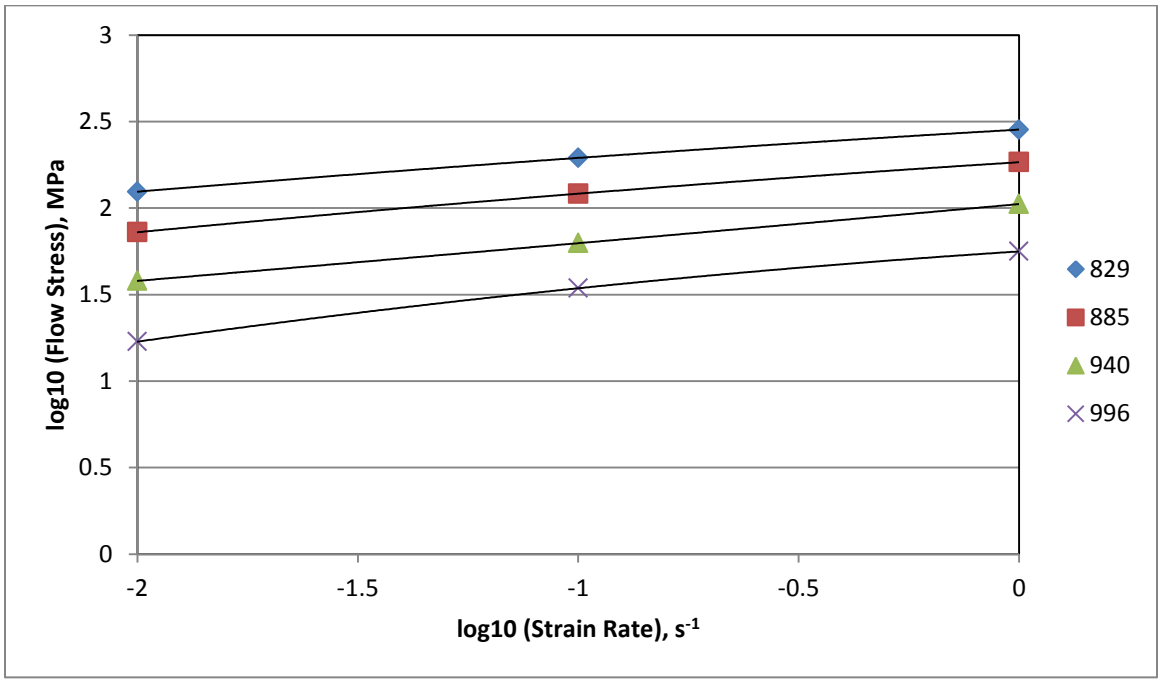

Figure 31: Variation of flow stress at different temperatures for PH 3-1

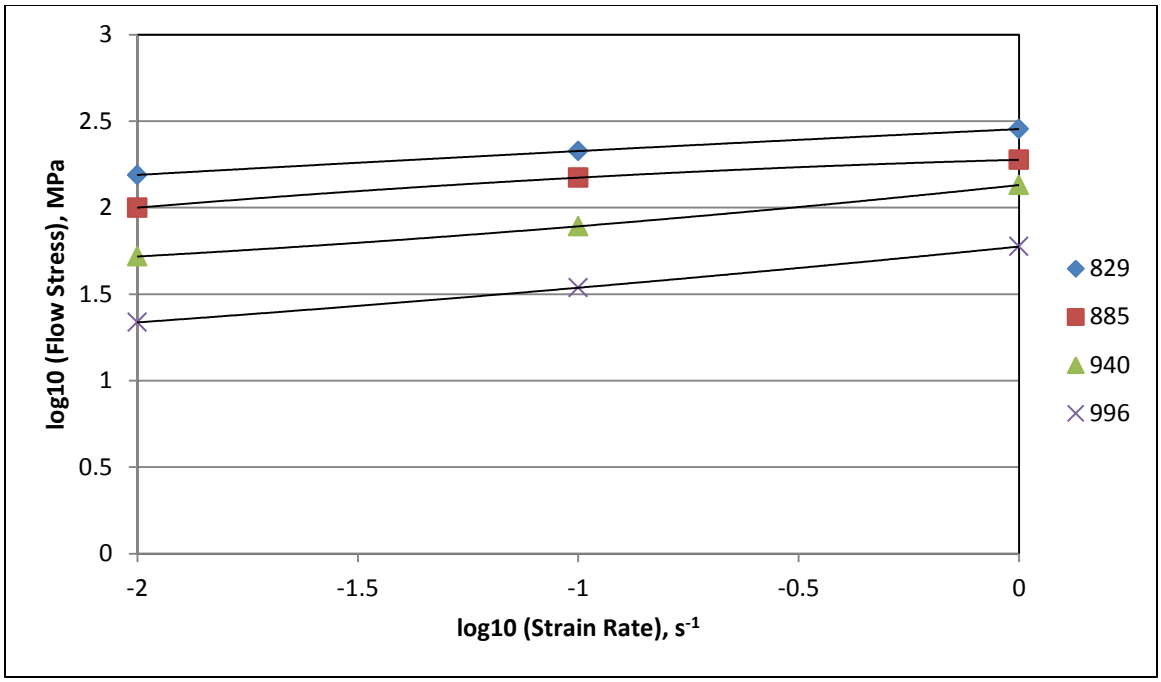

Figure 32: Variation of flow stress at different temperatures for 3-2

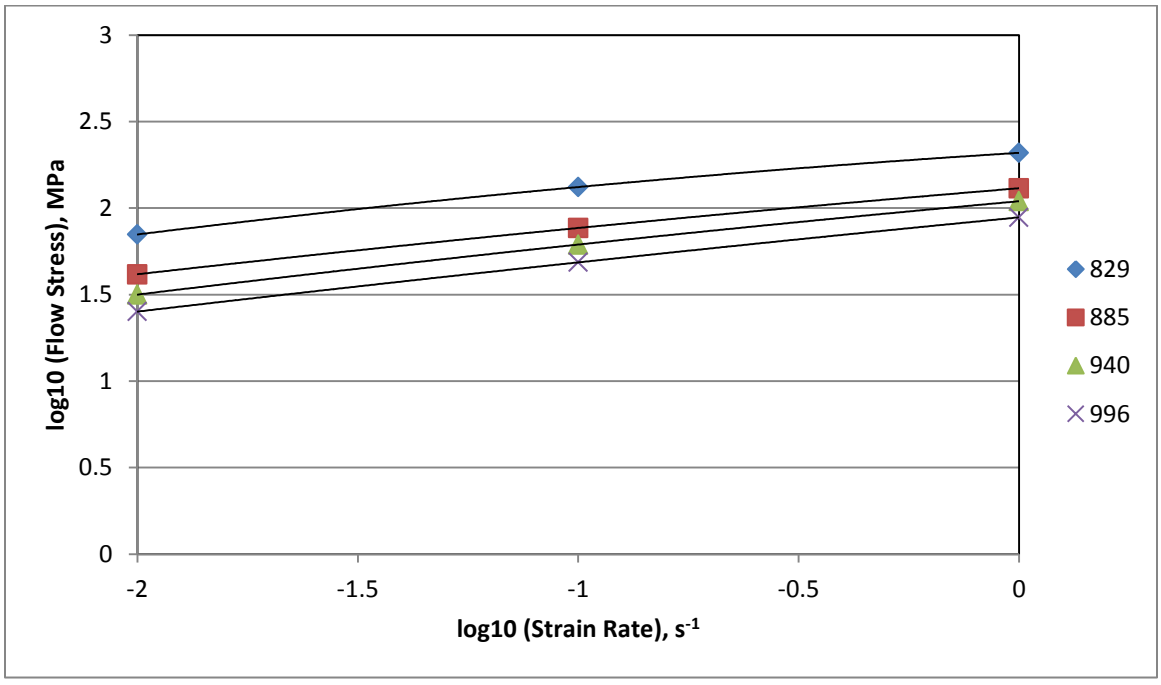

Figure 33: Variation of flow stress at different temperatures for PH 3-2

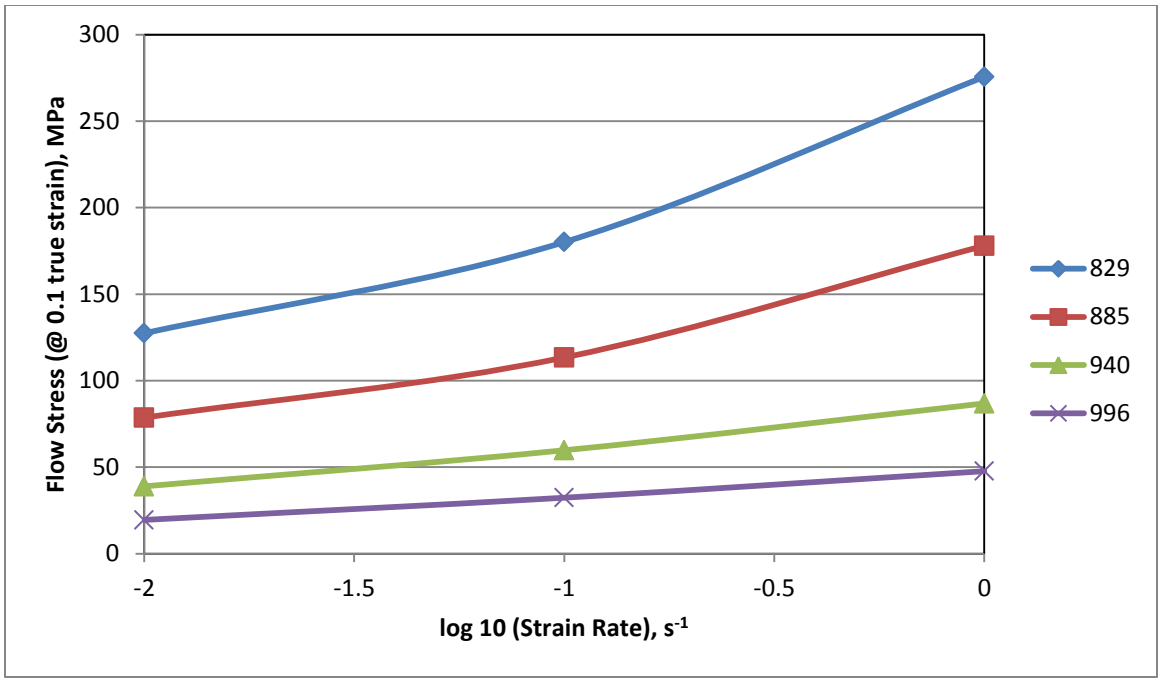

Figure 34: Flow Stress (MPa) vs. log (Strain rate, s^{-1}) plot for 3-1

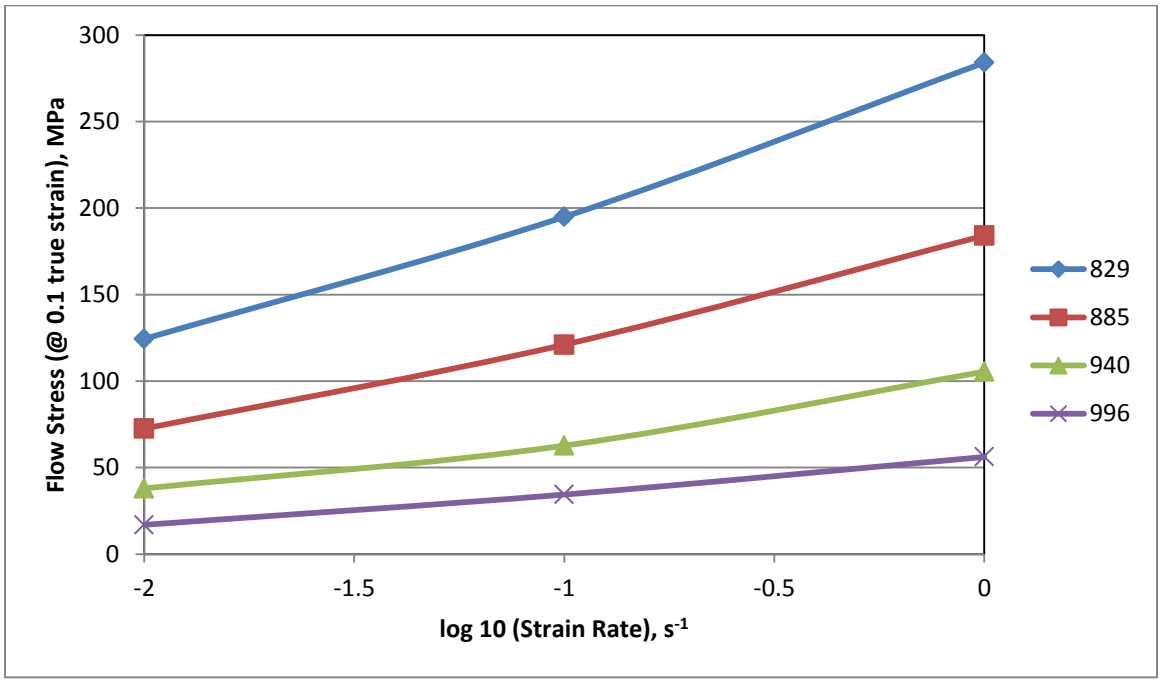

Figure 35: Flow Stress (MPa) vs. log (Strain rate, s^{-1}) plot for PH 3-1

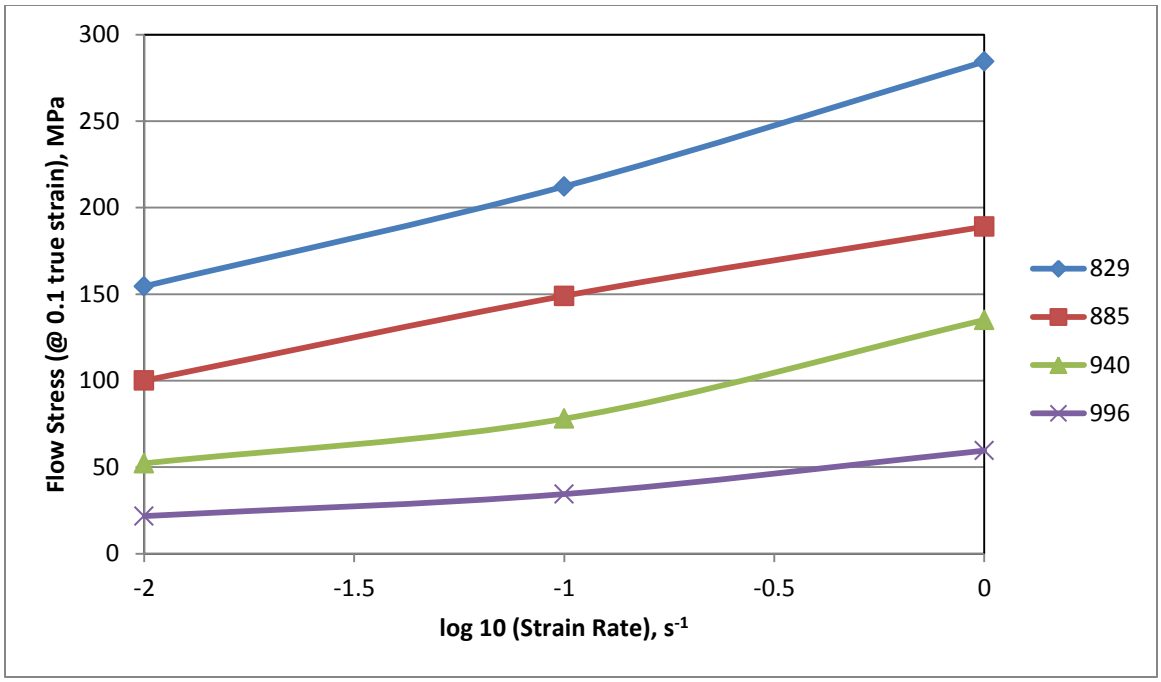

Figure 36: Flow Stress (MPa) vs. log (Strain rate, s^{-1}) plot for 3-2

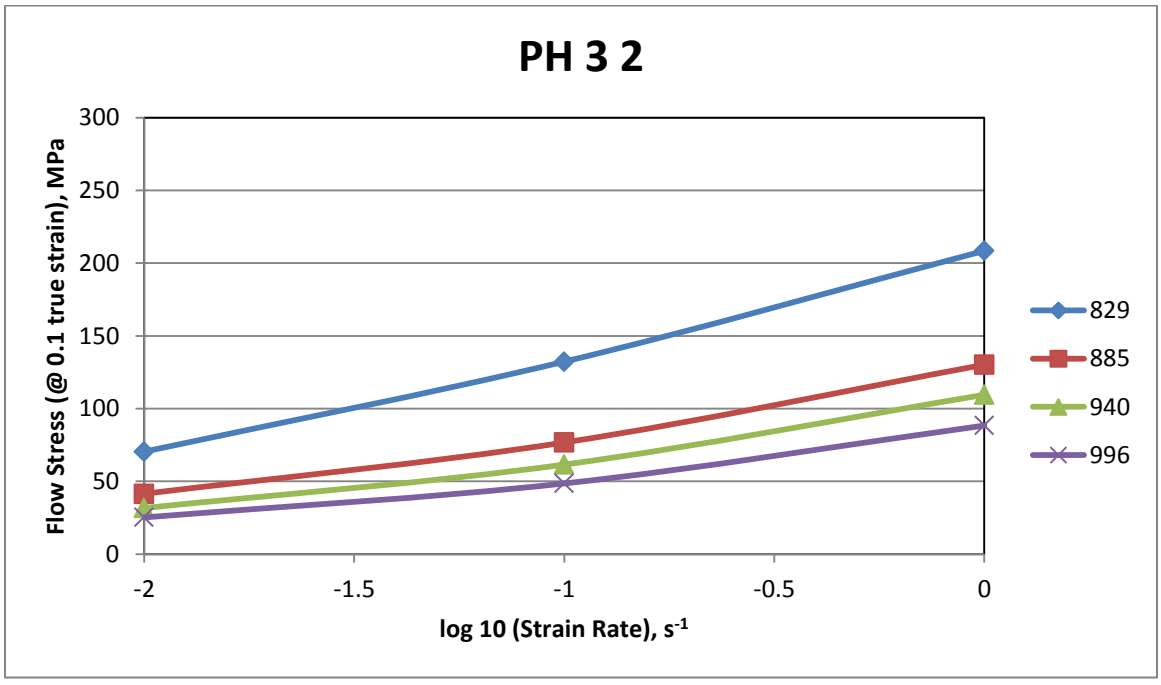

Figure 37: Flow Stress (MPa) vs. log (Strain rate, s^{-1}) plot for PH 3-2

The Zener – Hollomon equation was used to establish a relationship among the flow stress, strain rate and temperature [24].

In this approach, the temperature compensated strain rate Z:

$$Z = \dot{\varepsilon} \exp\left(\frac{Q}{RT}\right)$$

Is expressed as a function of flow stress

$$Z = A[\sinh \alpha\sigma]^{c}$$

Where A, α and c are experimental constants and

$$\alpha = \frac{\beta}{n}$$

Here

$$\beta = \frac{2.303}{slope\ ((Flow\ Stress)\ v/s \log(Strain\ Rate))}$$

at constant temperature. The flow stress vs. log (strain rate) plots used to calculate the value of β is show in Figures 38 to 41.

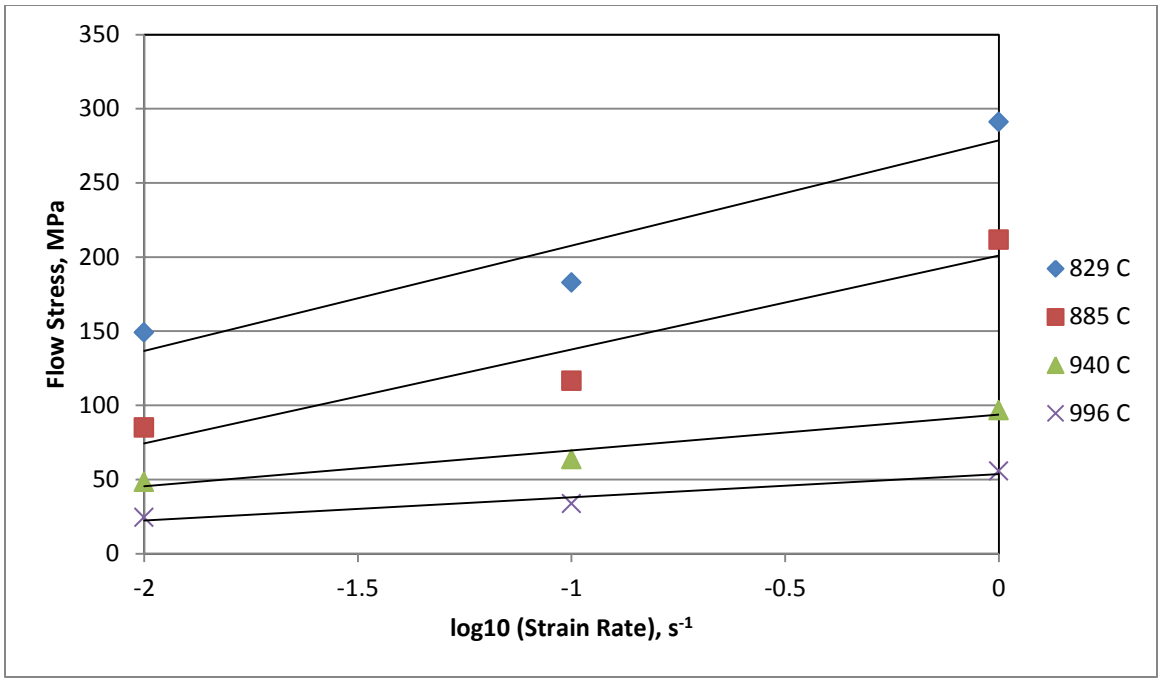

Figure 38: β value for 3-1 at different temperatures in ^{o}C

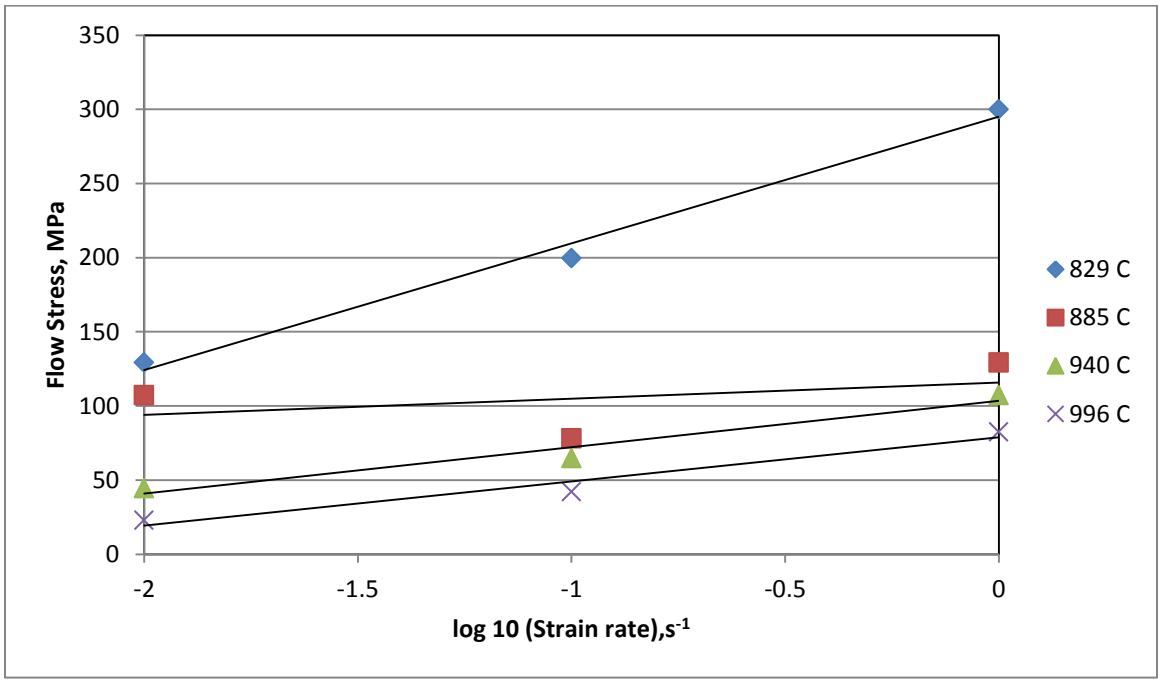

Figure 39: β value for PH 3-1 at different temperatures in ^{o}C

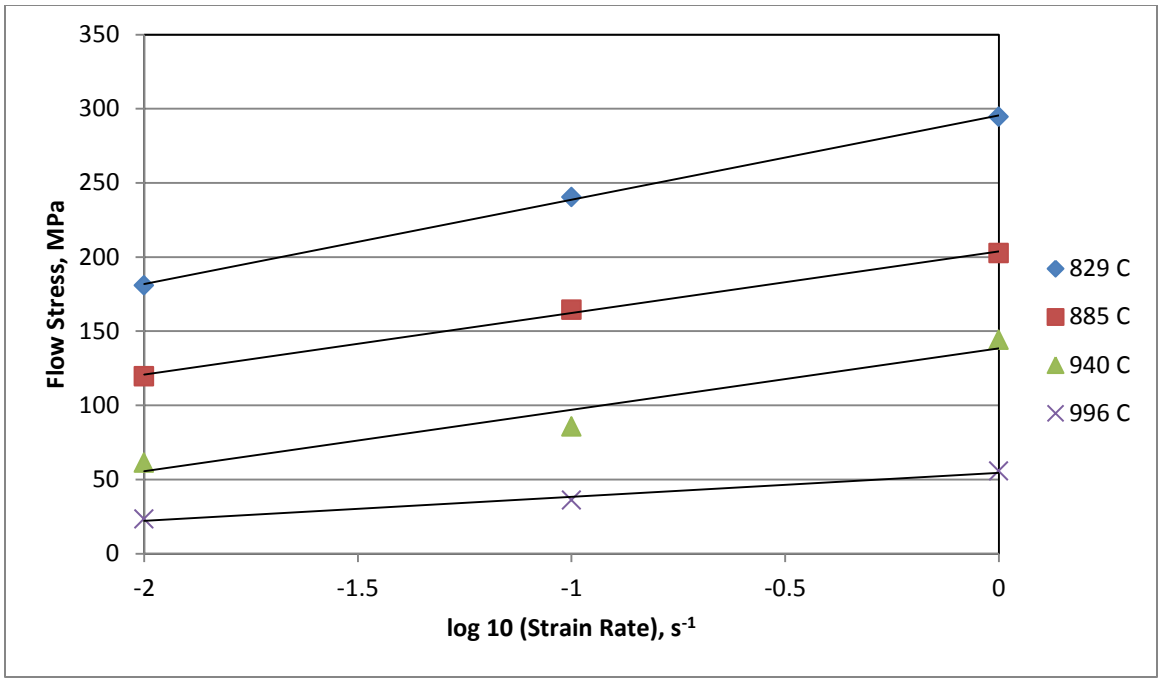

Figure 40: β value for 3-2 at different temperatures in ^{o}C

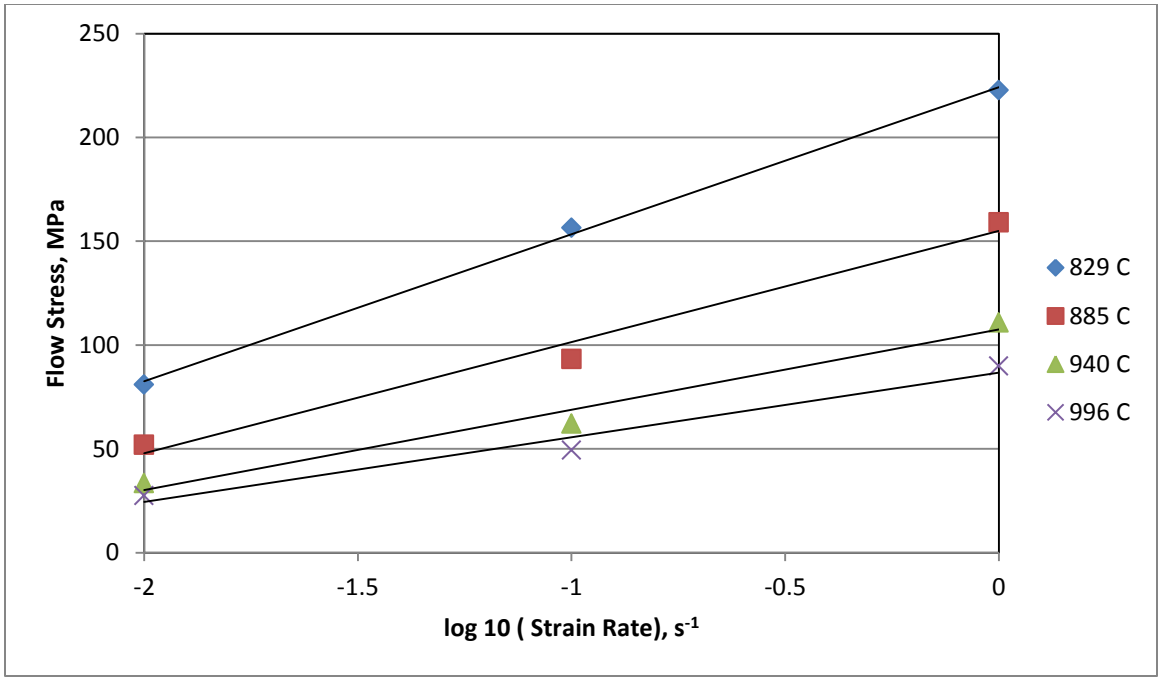

Figure 41: β value for PH 3-2 at different temperatures in ^{o}C

The value n is the reciprocal of m as shown in Table 4 and is denoted as

$$n = \frac{1}{m}$$

The value of n decreases as the temperature is decreased. Table 5 shows the values of n at different temperatures for different materials.

Table 5: Values of strain rate hardening exponent at different temperatures for different materials

Material / Temperature (^{o}C)	PH 3 1	3 1	PH 3 2	3 2
829	5.58	5.97	4.45	7.54
885	4.94	5.63	4.02	7.24
940	4.5	5.73	3.71	4.84
996	3.84	5.15	3.67	4.56

Table 6 shows the average values of m, n, β and α for all the experimental materials used.

Table 6: Average values of m, n, β and α for different materials

	m	n	β	α (MPa^{-1})
3-1	0.1784	5.6208	0.0776	0.0151
PH 3-1	0.2161	4.7149	0.0553	0.0125
3-2	0.1741	6.0454	0.0733	0.0139
PH 3-2	0.2539	3.9626	0.0522	0.0135

Iso stress lines were drawn on Figures 30 to 33 to obtain the values of strain rates which had the same flow stress value at different temperatures. The obtained strain rates were plotted as a function of temperature and these plots can be seen in Figures 42 to 45. A linear fit was obtained for log (strain rate) vs. 1/T plot. The slope of the curve was Q/R.

$$Q = -R \frac{\delta \ln(\dot{\epsilon})}{\delta(\frac{1}{T})}\Bigg|_{\sigma}$$

Where R is the universal gas constant.

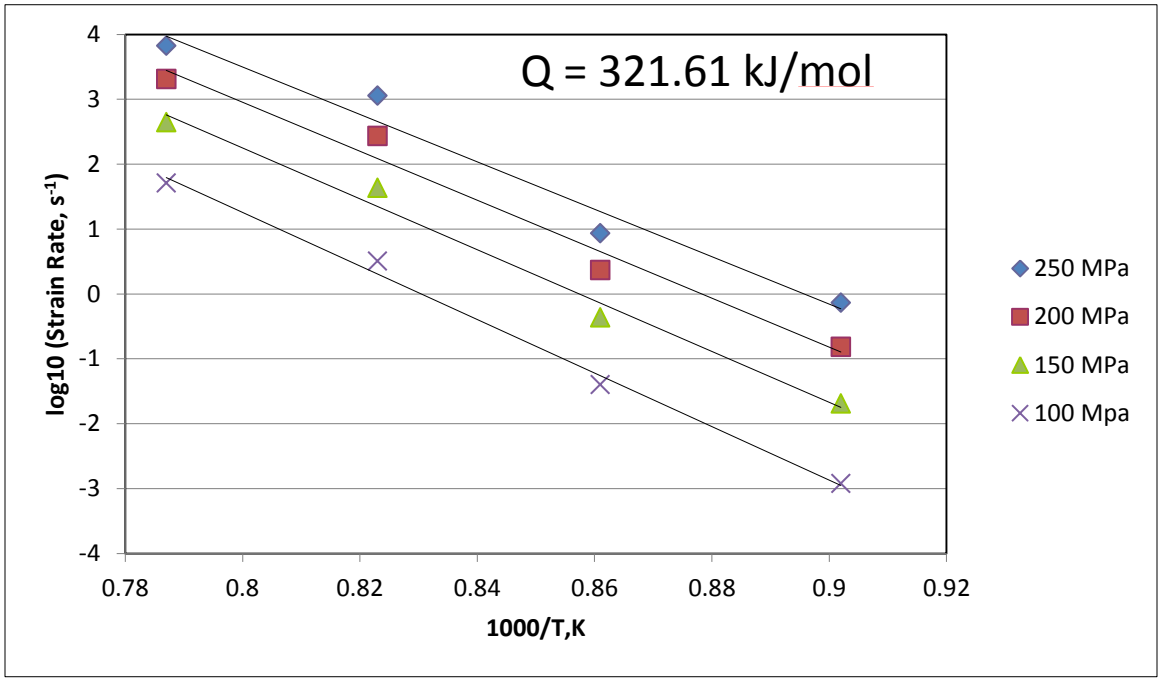

Figure 42: Activation energy plot of 3-1

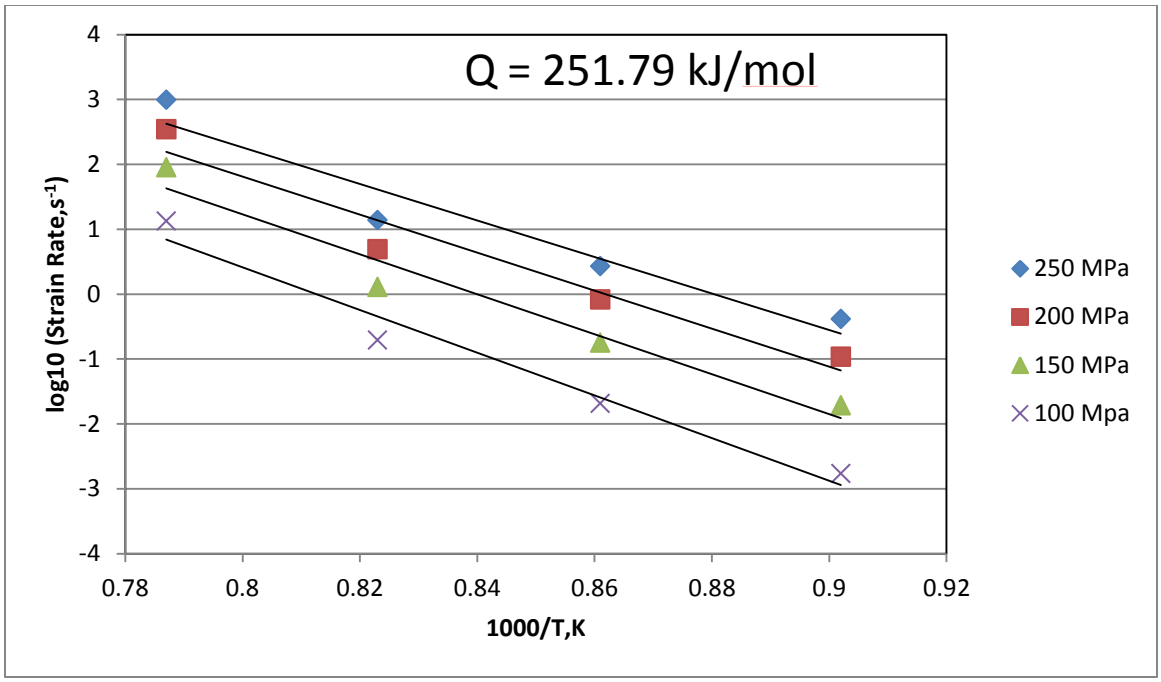

Figure 43: Activation energy plot of PH 3-1

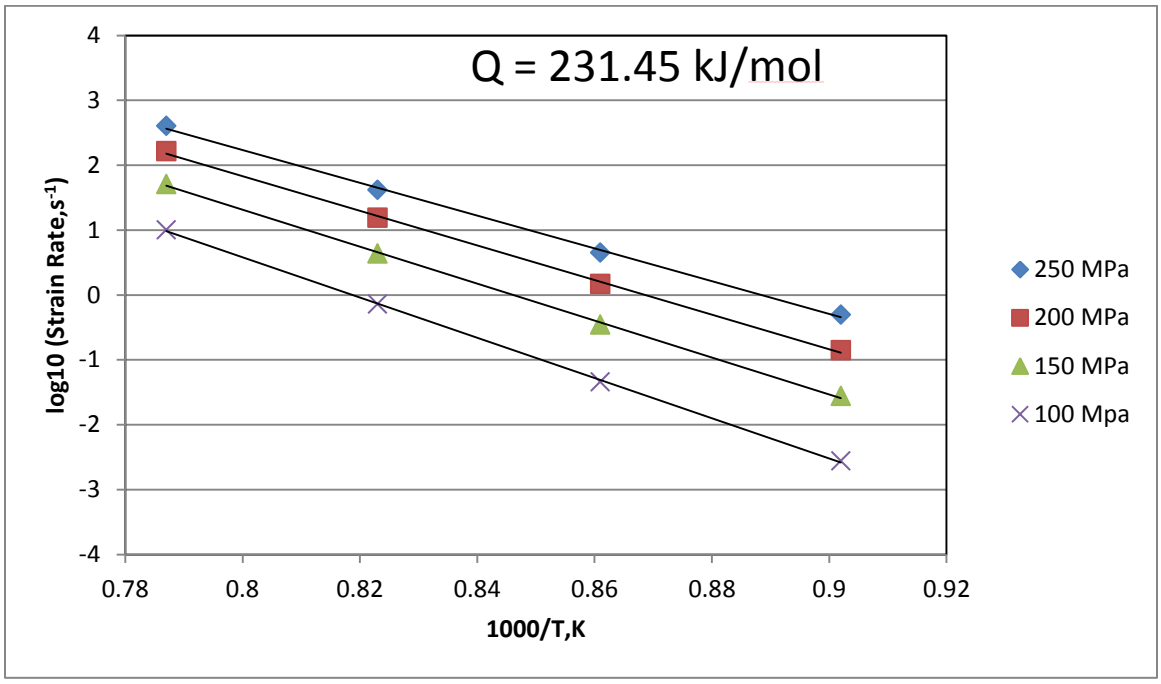

Figure 44: Activation energy plot of 3-2

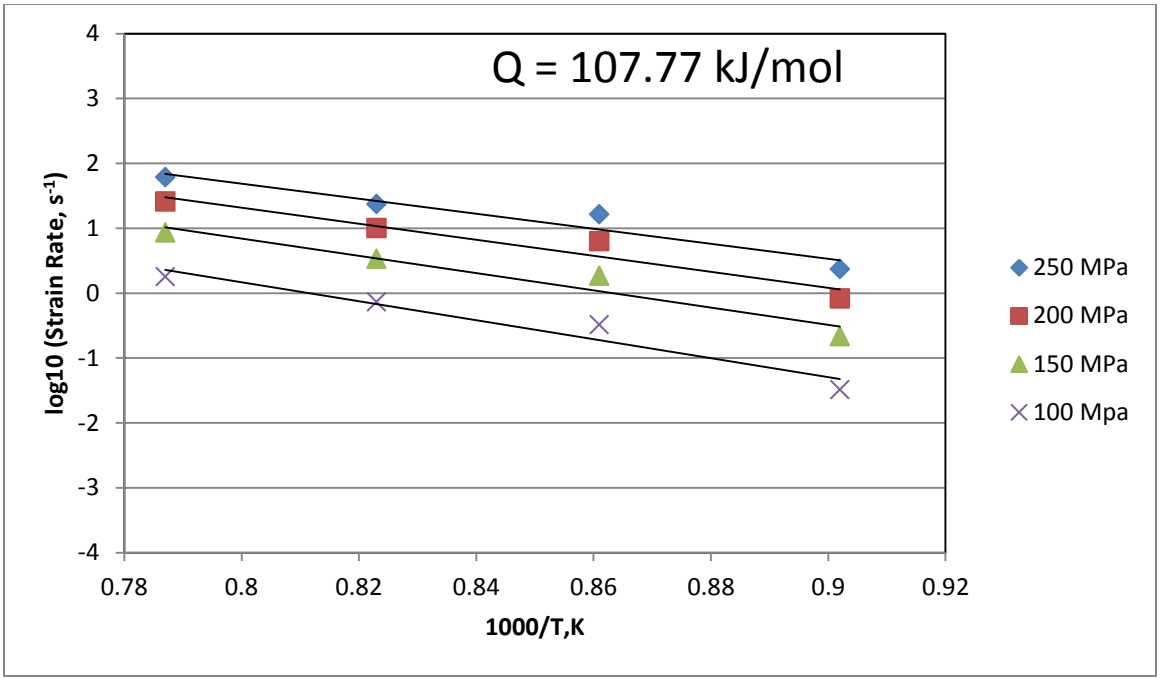

Figure 45: Activation energy plot of PH 3-2

Table 7 shows the activation energy of the alloys.

Table 7: Activations energies of different alloys

Alloy	Activation Energy (Q) in kJ/mol
3 1	321.61
3 2	251.79
PH 3 1	231.45
PH 3 2	107.77

The activation energies of the HIPed and pre HIPed α+β processed alloys are estimated from the plot are around 320 kJ/mol and 231.45 kJ/mol respectively and are in argument with the results given in literature [16]. This value is almost twice the amount of self-diffusion of α – Ti whose value is 150 kJ/mol. The activation energies of the

HIPed and pre HIPed β processed alloys are 251.79 kJ/mol and 107.77 kJ/mol respectively and these values are close that of self-diffusion in β (153 kJ/mol) [16].

Continuing the analysis a relationship between flow stress at a true strain of 0.1 and temperature compensated strain rate Z (Zener Hollomon Parameter) was developed between temperatures 829°C to 996°C and Figures 46 to 49 shows the plots. All the plots show a good fit of the data which implies that the kinetic rate equation is obeyed in the temperature range and at all strain rates.

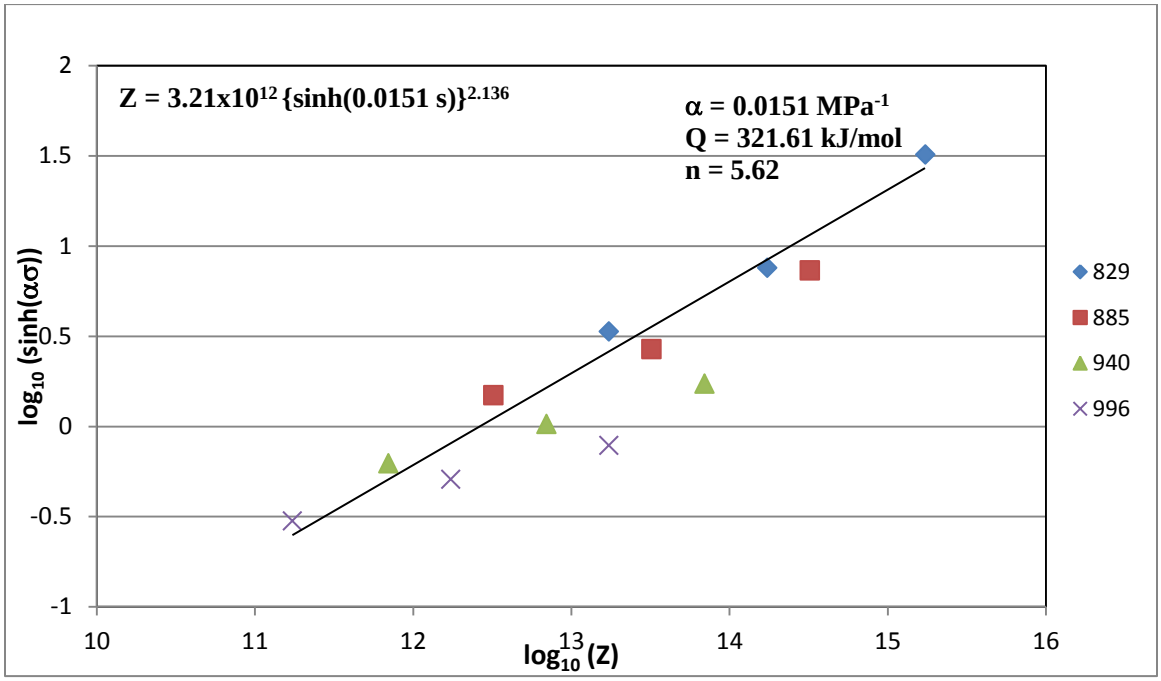

Figure 46: Zener Hollomon relationship for 3-1 at different temperatures in °C

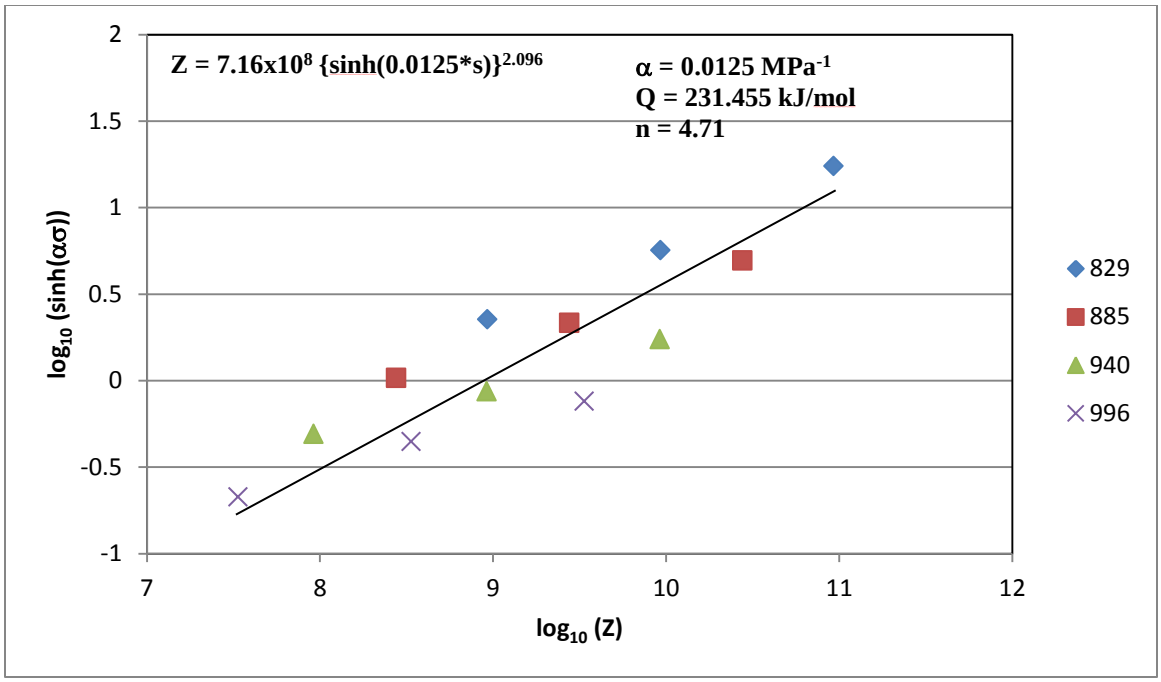

Figure 47: Zener Hollomon relationship for PH 3-1 at different temperatures in ^{o}C.

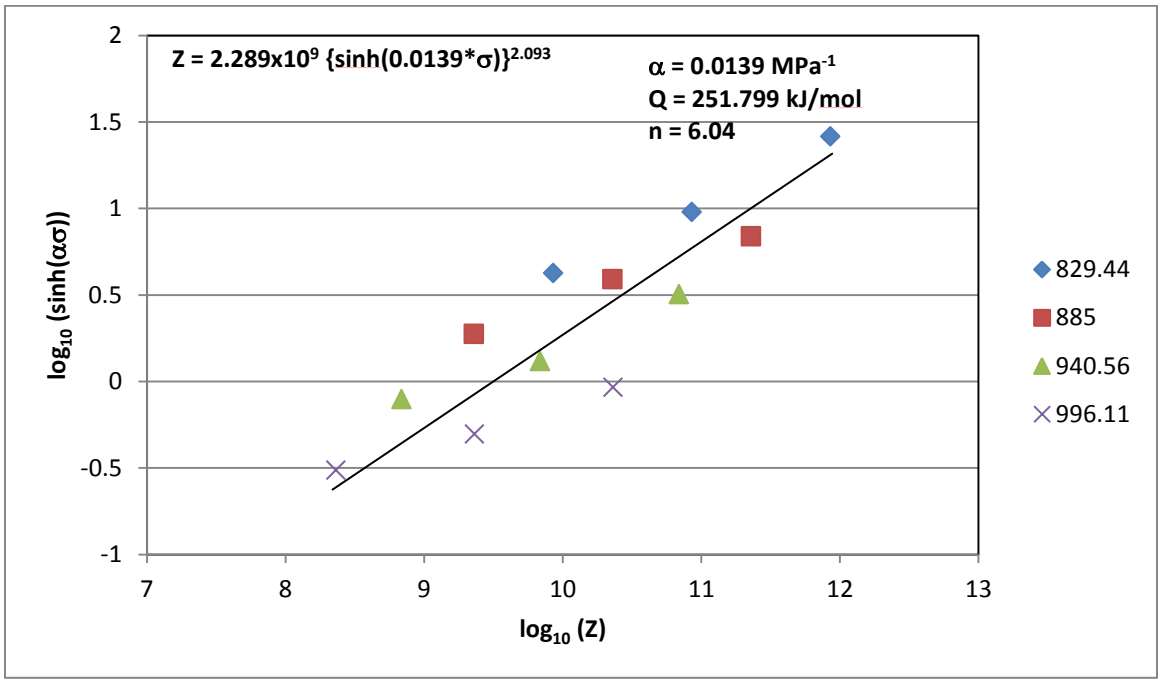

Figure 48: Zener Hollomon relationship for 3-2 at different temperatures in ^{o}C

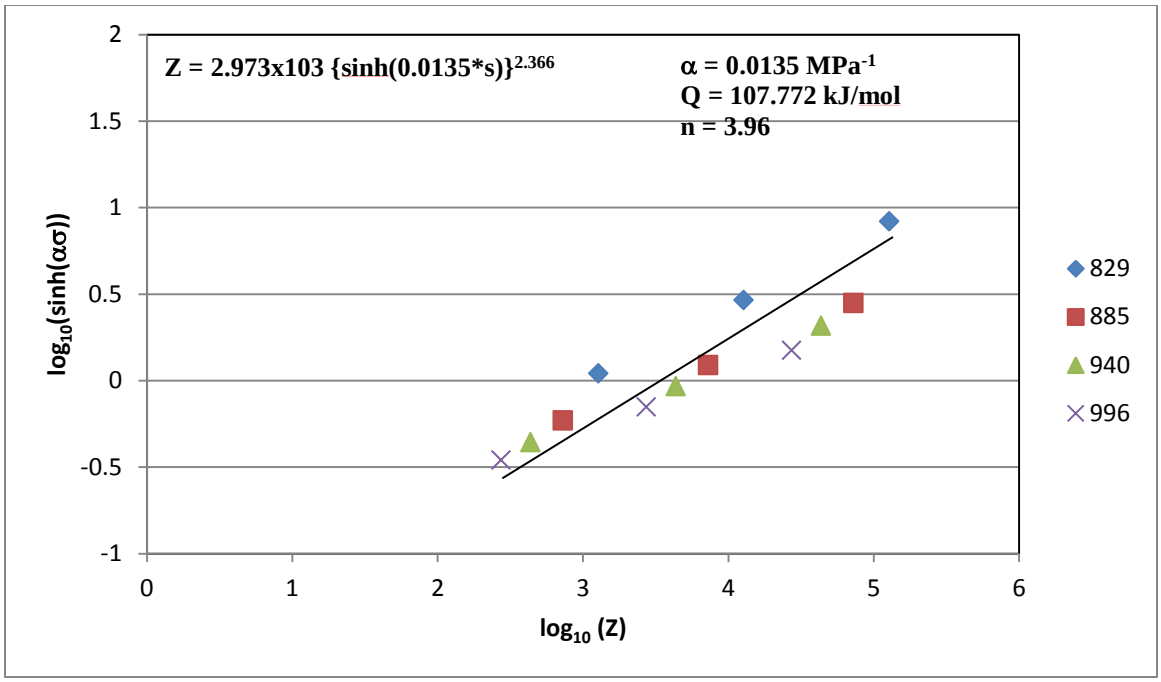

Figure 49: Zener Hollomon relationship for PH 3-2 at different temperatures in ^{o}C

4.3 Microstructural Analysis

4.3.1 HIPed and pre HIPed α+β processed alloys

Optical microscope images of the compressed samples of HIPed and pre HIPed α+β processed alloys were used to study the effect of deformation and processing on the microstructure of those alloys. Figures 50 to 53 show the microstructures of α+β processed at different stain rates tested at temperatures of 829^{o}C, 885^{o}C, 940^{o}C and 996^{o}C respectively.

Comparing Figures 12 (a) and 50 (a), (b) and (c), it is seen that for the undeformed sample kinked lamellae is observed. For the deformed samples at all strain rates the lamellae seem to have reoriented to a direction that is perpendicular to the compression direction. From Figures 50 (a) (b) and (c) it is seen that for the samples

deformed at 829^{o}C as the strain rate is decreased the lamellae got coarser. For the samples deformed at 885^{o}C (Figures 51 (a) (b) and (c)), coarser lamellae were observed as compared to that of the lamellae observed at 829^{o}C and as the strain rate decreased, coarsening of the lamellae took place and the orientation of lamellae to the compression direction got more perpendicular. For the samples deformed at 940^{o}C (Figures 52 (a) (b) and (c)) as the temperature of deformation was nearing the beta transus temperature a fine lamellar regions are observed between larger α plates in the microstructures and the lamellae was much more coarser than compared to the samples deformed at 885^{o}C and the width of the lamellae increased as the strain rate was decreased, this is because at a slower strain rate deformation more time is available for the growth of α lamellae. For the samples deformed at 996^{o}C which was a little above the beta transus temperature for the test material, the microstructure consisted of transformed beta in addition to some amounts of retained α phase.

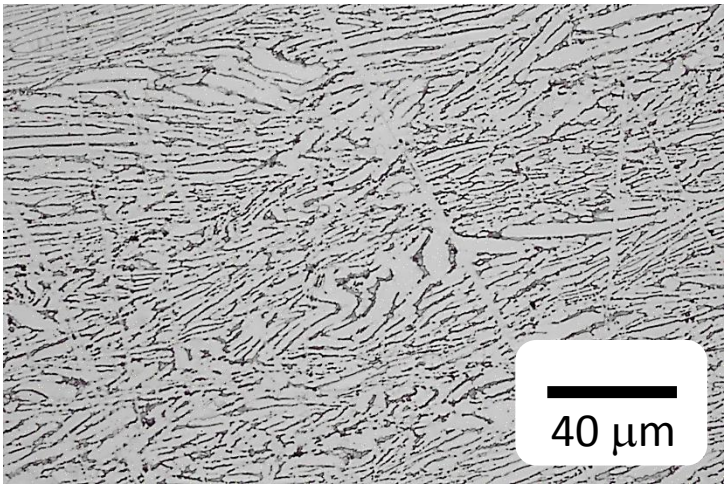

(a) 1/sec

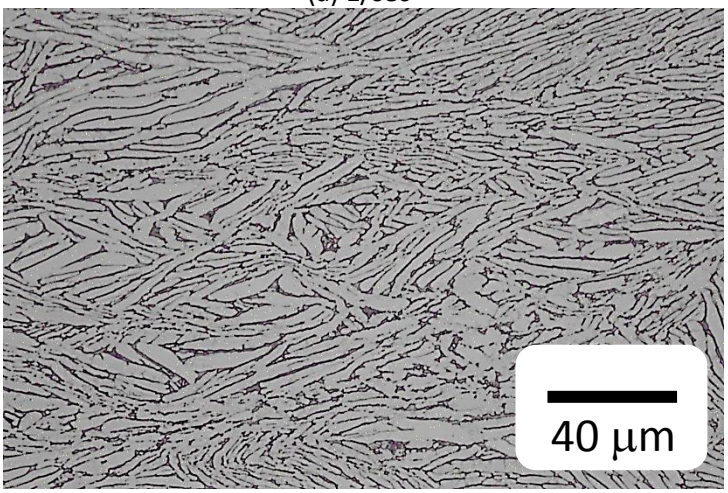

(b) 0.1/sec

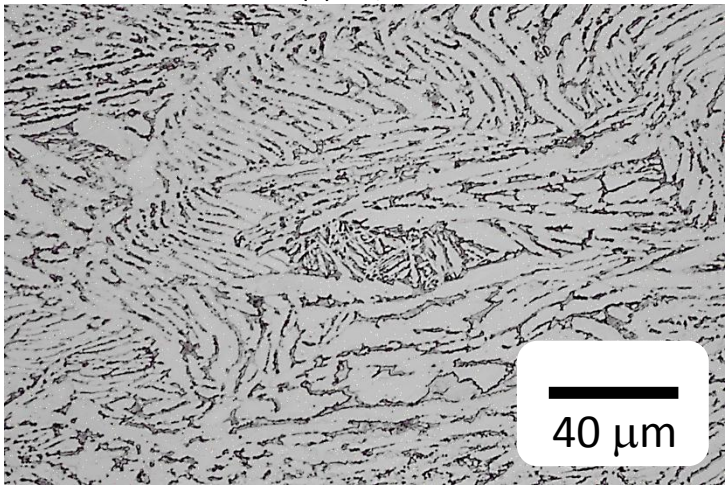

(c) 0.01/sec

Figure 50: Optical Micrographs of PH 3-1 at 829°C and at different strain rates (compression direction is vertical)

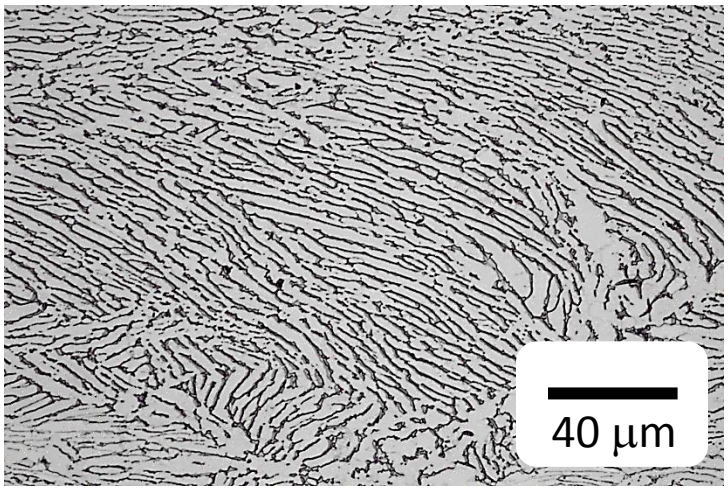

(a) 1/sec

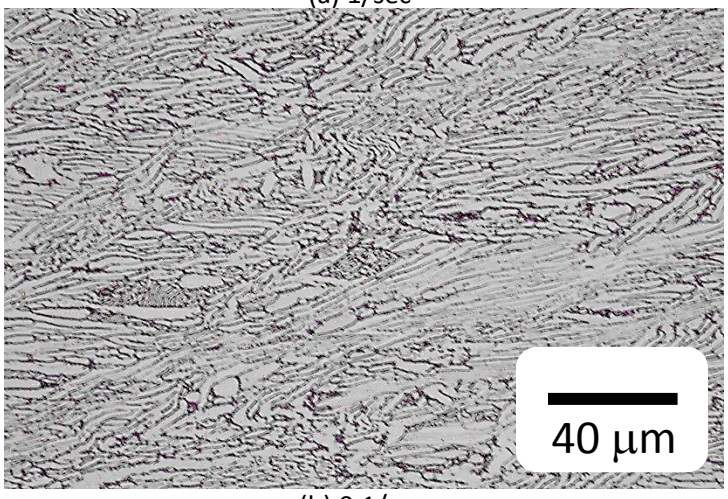

(b) 0.1/sec

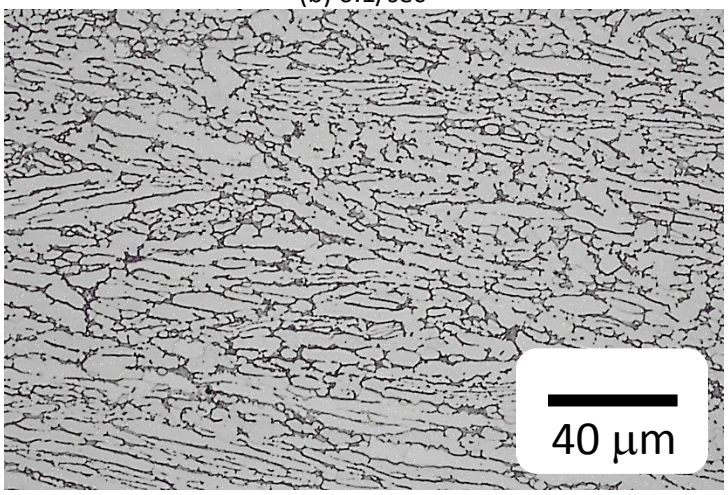

(c) 0.01/sec

Figure 51: Optical Micrographs of PH 3-1 at 885°C and at different strain rate (compression direction is vertical)

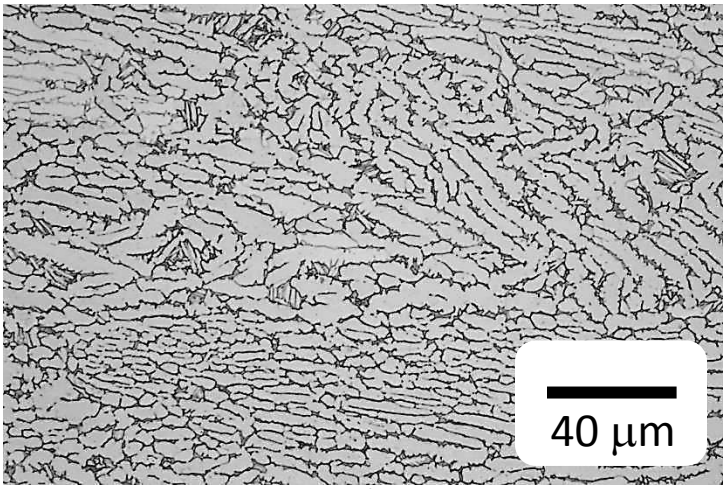

(a) 1/sec

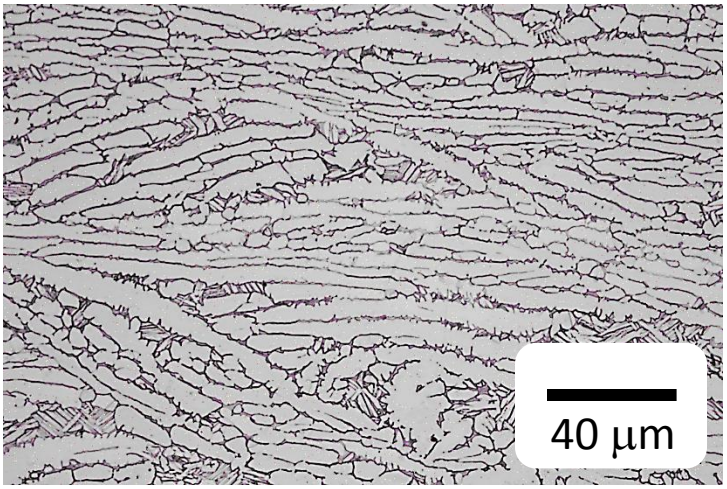

(b) 0.1/sec

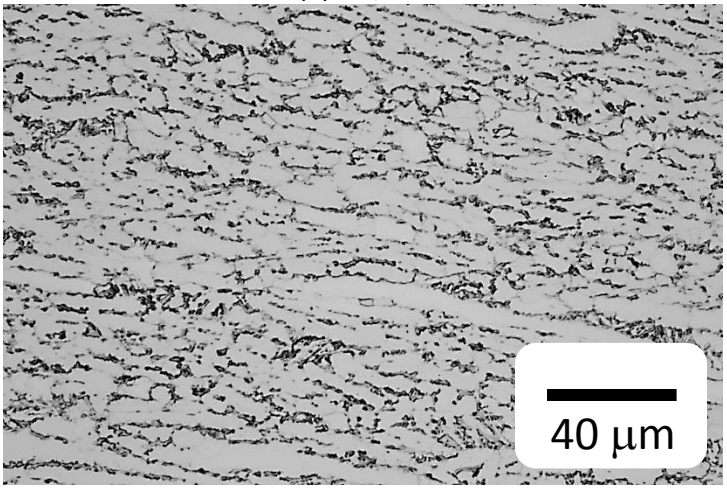

(c) 0.01/sec

Figure 52: Optical Micrographs of PH 3-1 at 940°C and at different strain rates (compression direction is vertical)

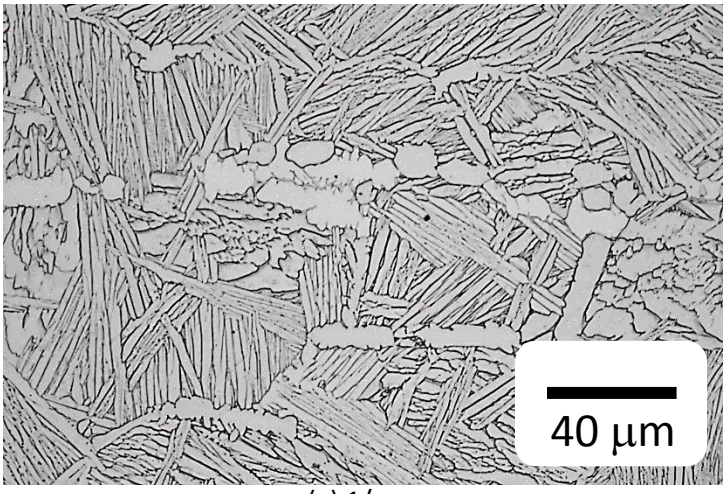

(a) 1/sec

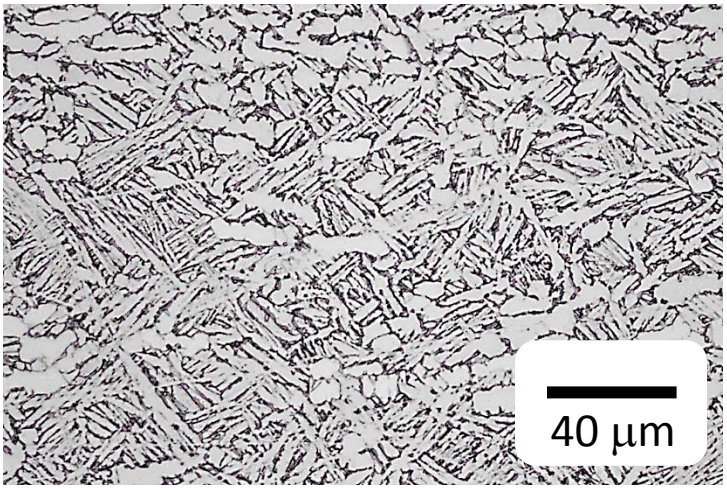

(b) 0.1/sec

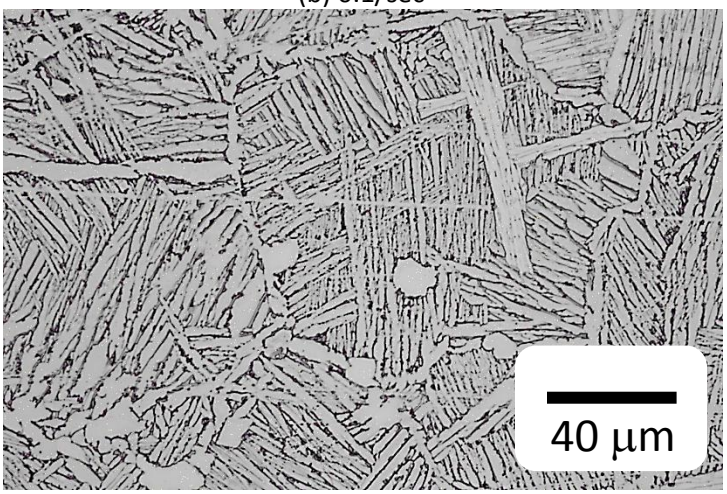

(c) 0.01/sec

Figure 53: Optical Micrographs of PH 3-1 at 996°C and at different strain rates (compression direction is vertical)

Figures 54 to 57 show the optical microscope images of the α+β processed + HIPed samples deformed at different strain rates and at temperatures of 829^{o}C, 885^{o}C, 940^{o}C and 996^{o}C.

Figure 12(b) shows the undeformed microstructure of the α+β processed + HIPed material and Figures 54 (a) (b) and (c) show the microstructures of the same material which was deformed at a temperature of 829^{o}C and at different strain rates. Comparing the figures it is observed that before the deformation the α lamellae were oriented in several directions. After the deformation the orientation of the α lamellae became more perpendicular to the compression axis at all strain rates and it is also observed that as the strain rate was reduced the width of α lamellae increased. Figures 55 (a) (b) and (c) show the microstructures of the α+β processed sample deformed at a temperature of 885^{o}C and at different strain rates. From the figures it is observed that the degree of coarsening of the α lamellae is higher than compared to the samples deformed at 829^{o}C (Figure 54) and it is also observed that at this temperature the width of α lamellae increased as the strain rate was decreased. Figures 56 (a) (b) and (c) show the microstructures of the samples deformed at temperature of 940^{o}C. As this temperature is closer to the beta transus temperature of the material, the microstructure consists of small amounts of β along with α lamellae at all strain rates and as in the earlier cases the width of the α lamellae increased as the strain rate was decreased. The microstructures of the samples deformed at 996^{o}C and at different strain rates can be seen in Figures 57 (a) (b) and (c), as this temperature was close to the beta transus temperature of the material the microstructure consists of β lamellae in addition to some amounts of retained α phase.

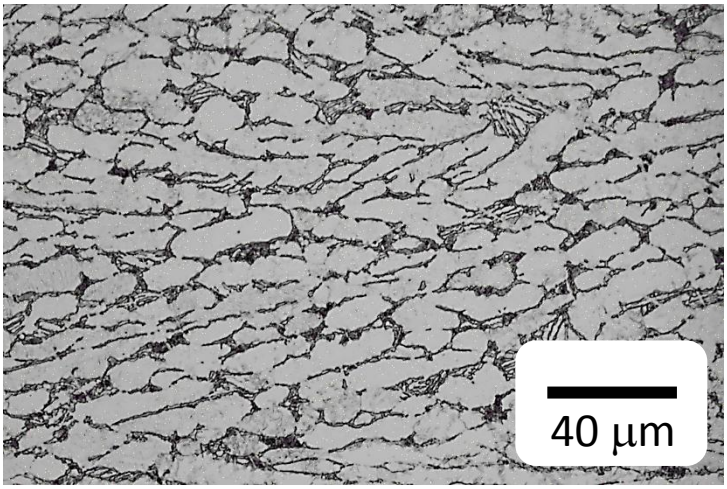

(a) 1/sec

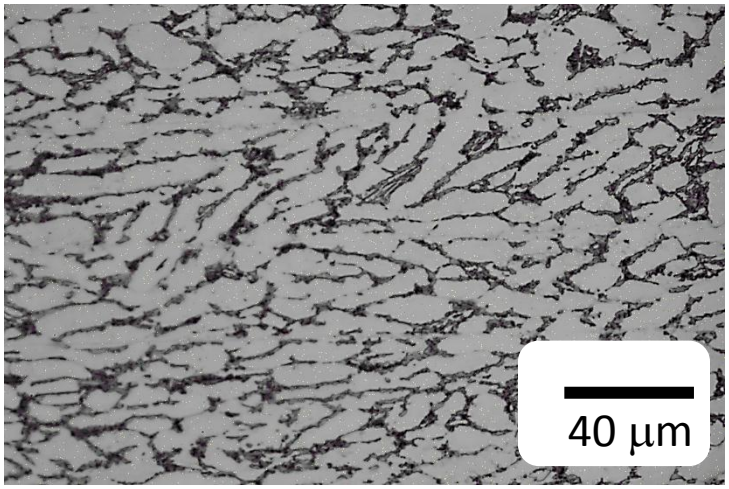

(b) 0.1/sec

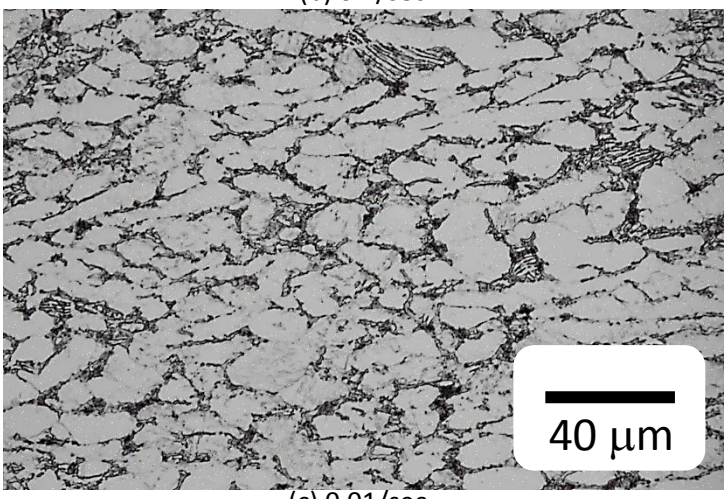

(c) 0.01/sec

Figure 54: Optical Micrographs of 3-1 at 829°C and at different strain rates (compression direction is vertical)

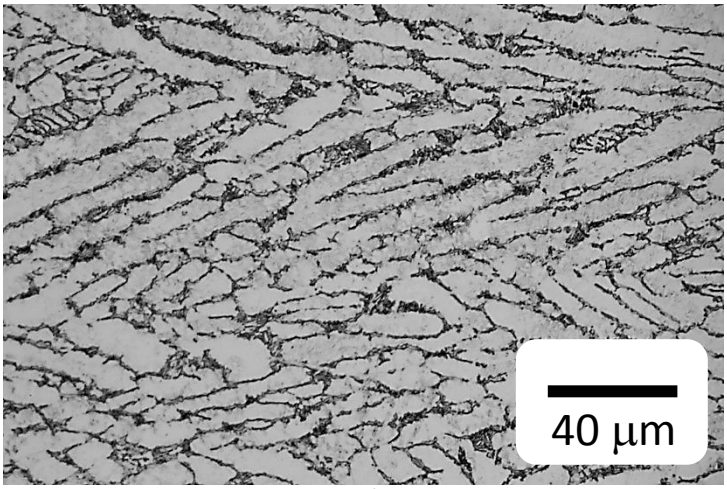

(a) 1/sec

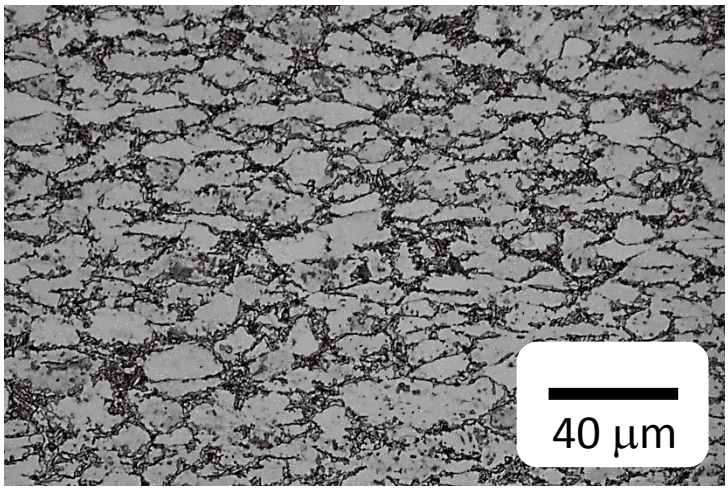

(b) 0.1/sec

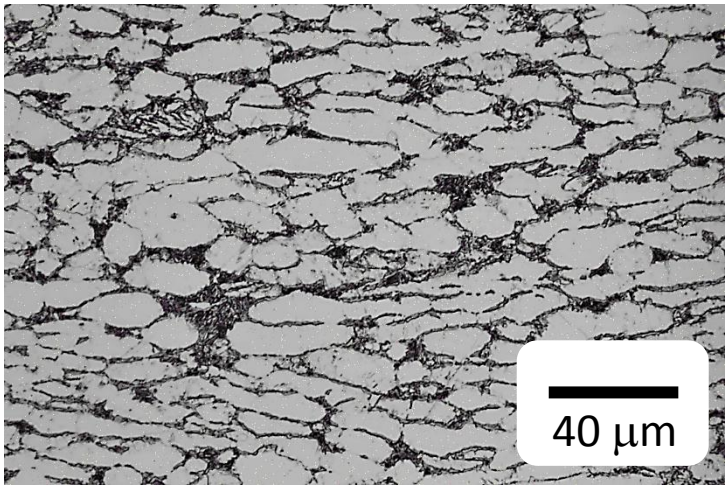

(c) 0.01/sec

Figure 55: Optical Micrographs of 3-1 at 885°C and at different strain rates (compression direction is vertical)

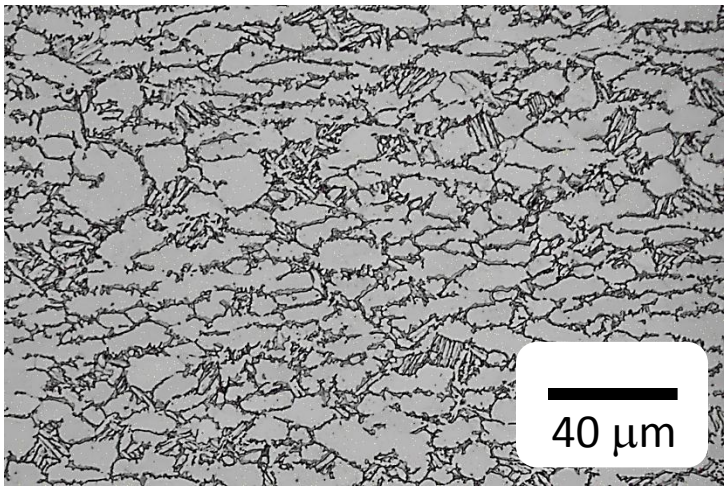

(a) 1/sec

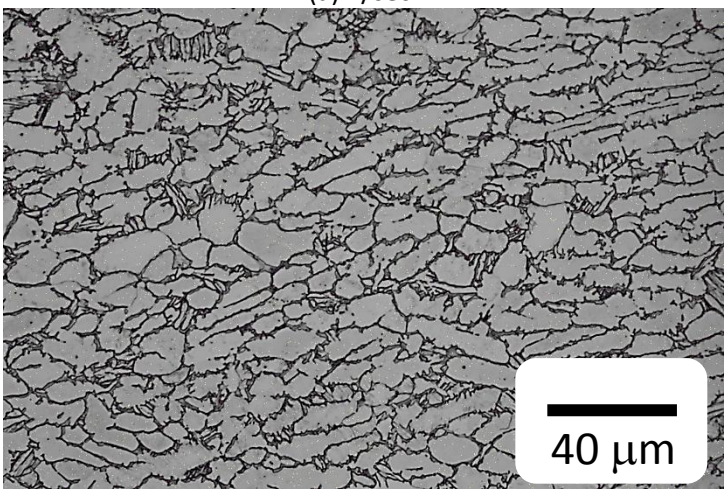

(b) 0.1/sec

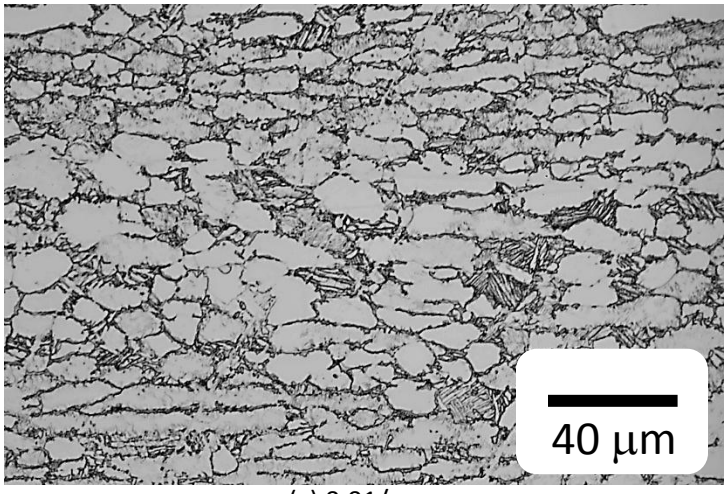

(c) 0.01/sec

Figure 56: Optical Micrographs of 3-1 at 940^{o}C and at different strain rates (compression direction is vertical)

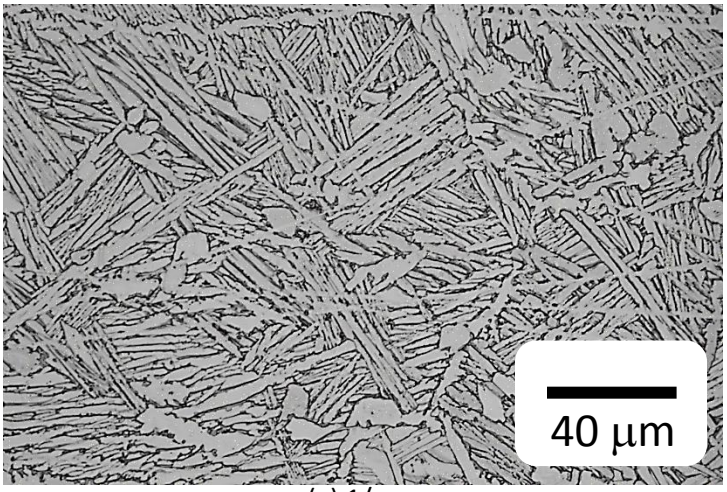

(a) 1/sec

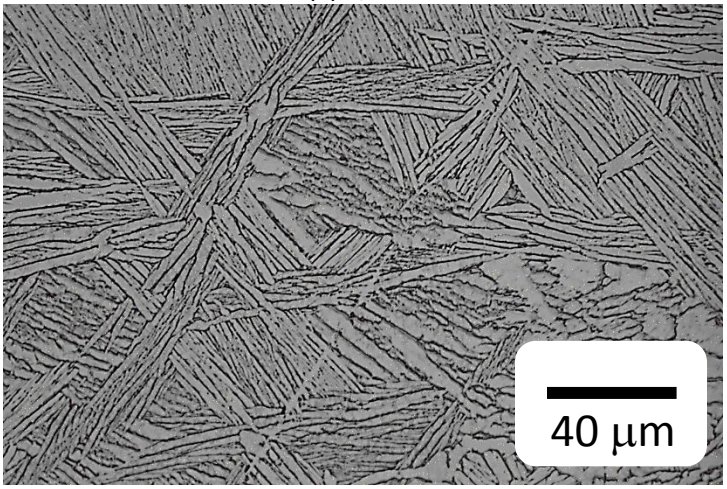

(b) 0.1/sec

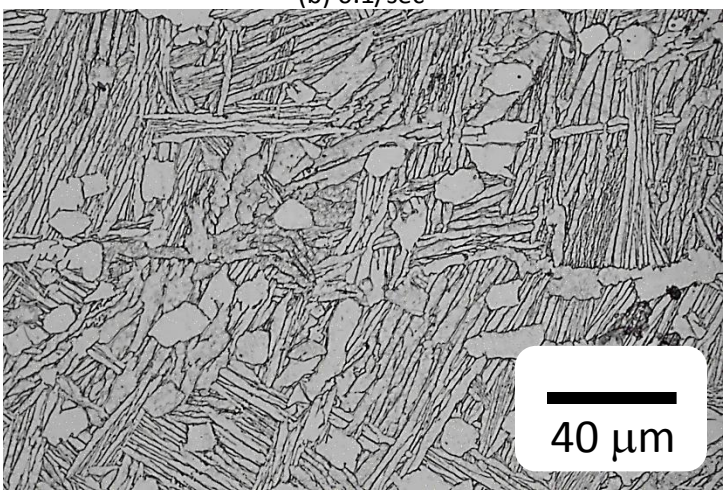

(c) 0.01/sec

Figure 57: Optical Micrographs of 3-1 at 996^{o}C and at different strain rates (compression direction is vertical)

4.3.2 HIPed and pre HIPed β processed alloys

Optical microscope images of the β processed samples tested at temperatures of 829^{o}C, 885^{o}C, 940^{o}C and 996^{o}C at different stain rates are shown in Figures 58 to 61.

Figure 12(c) shows the microstructure of the undeformed sample of the beta processed material. From the figure it is seen that the sample has a Widmanstatten structure. Figures 58 (a) (b) and (c) show the microstructures of the same sample deformed at 829^{o}C and at different strain rates. By comparing the microstructures it is seen that, the undeformed and the deformed microstructures are different to each other because the deformation of the sample was well below the beta transus temperature of the material. The microstructure therefore consists of relatively fine α+β lamellae. As the strain rate is reduced no significant difference in the microstructure is observed. Figures 59 (a) (b) and (c) show the microstructures of the samples deformed at 885^{o}C. From the figures it is seen that the microstructure is a combination of equiaxed α and lamellar α+β and it is also observed that as the strain rate reduced the degree of α lamellae coarsening increased. The bimodal structure observed in Figures 58 and 59 is essentially due to the deformation of the β processed sample in the α+β region, similar to the schematic shown in Figure 5. Figures 60 (a) (b) and (c) show the microstructures of the samples deformed at a temperature of 940^{o}C and it is observed that at all strain rates a Widmanstatten structure was observed. Figures 61 (a) (b) and (c) show the microstructures of samples deformed at 996^{o}C. From the figures it is seen that a Widmanstatten structure is observed at all temperatures and these microstructures when compared to the undeformed microstructure (Figure 12(c)) show that the deformed samples have a coarser lamellae.

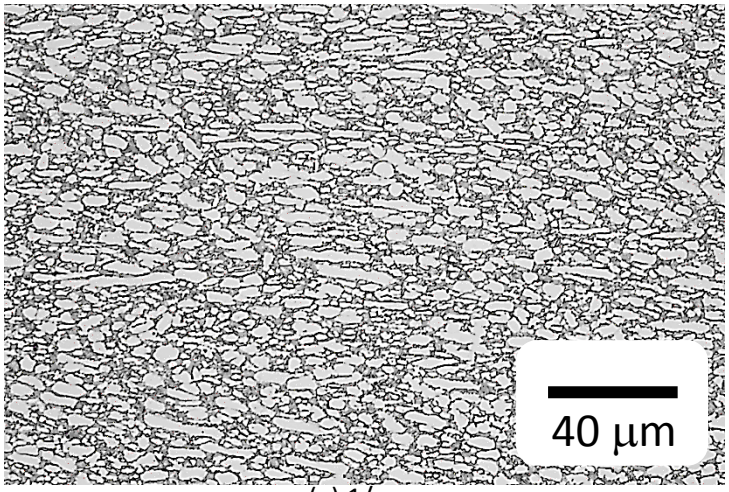

(a) 1/sec

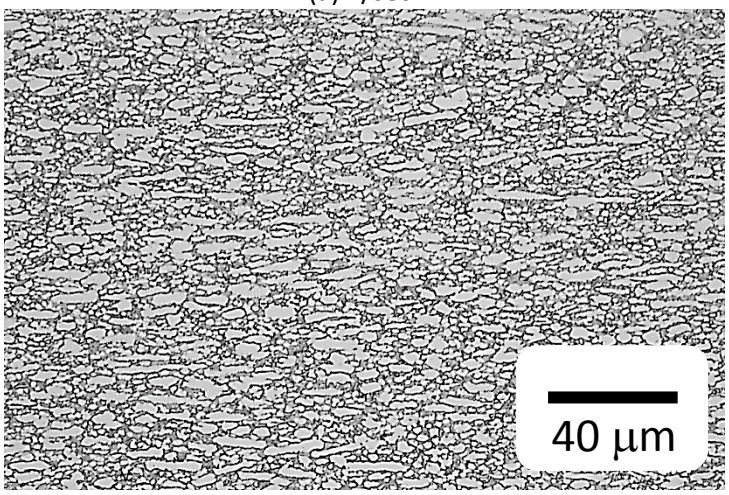

(b) 0.1/sec

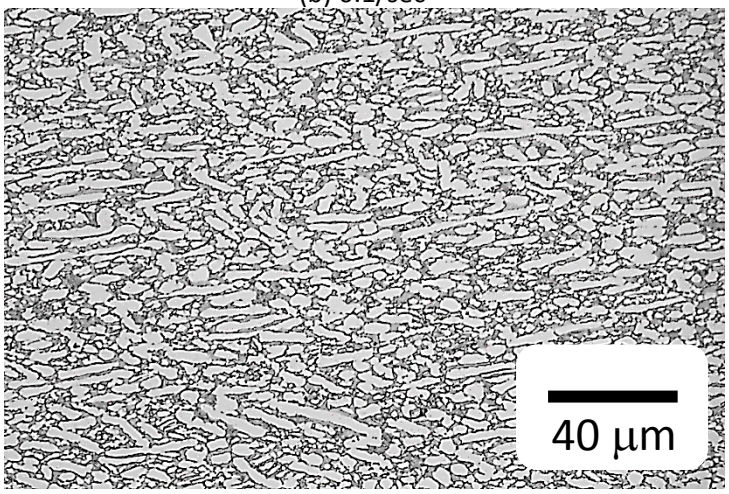

(c) 0.01/sec

Figure 58: Optical Micrographs of PH 3-2 at 829°C and at different strain rates (compression direction is vertical)

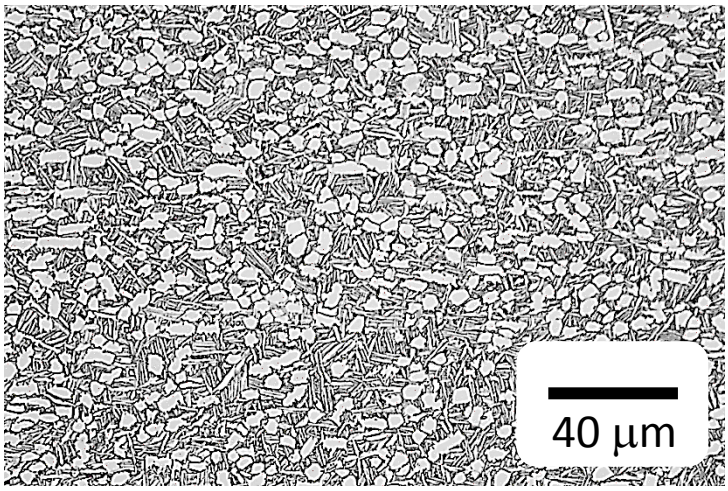

(a) 1/sec

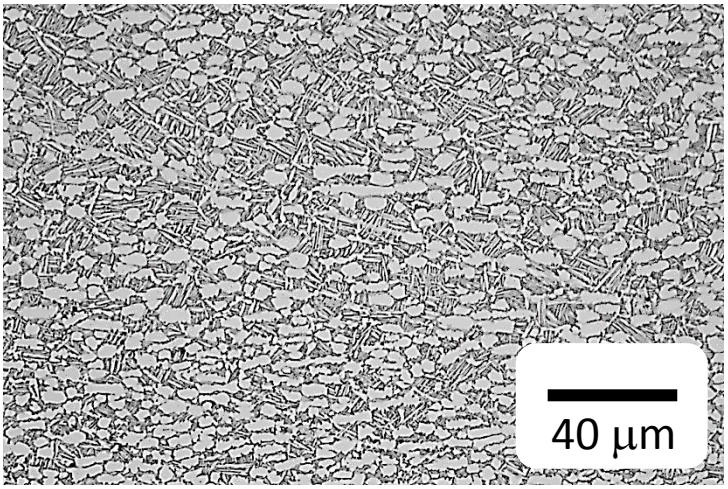

(b) 0.1/sec

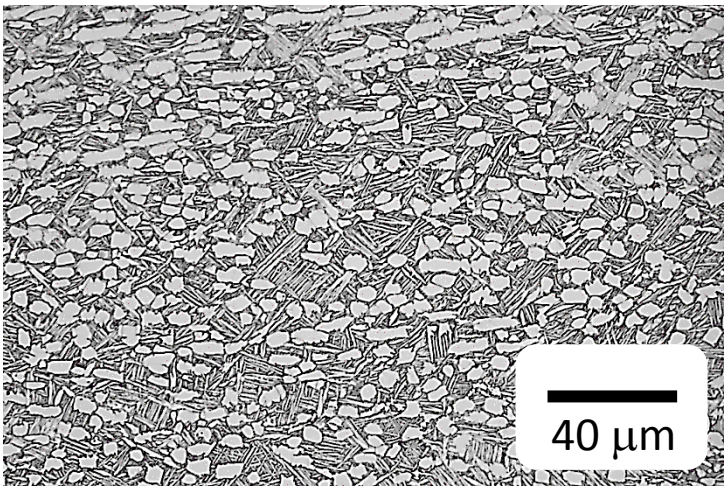

(c) 0.01/sec

Figure 59: Optical Micrographs of PH 3-2 at 885°C and at different strain rates (compression direction is vertical)

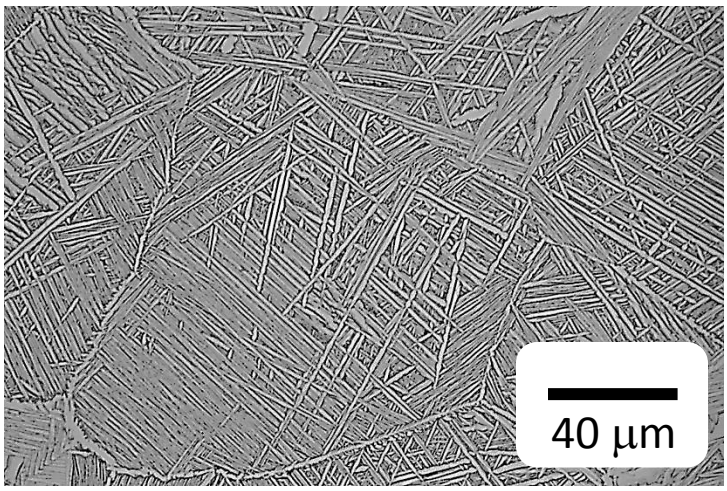

(a) 1/sec

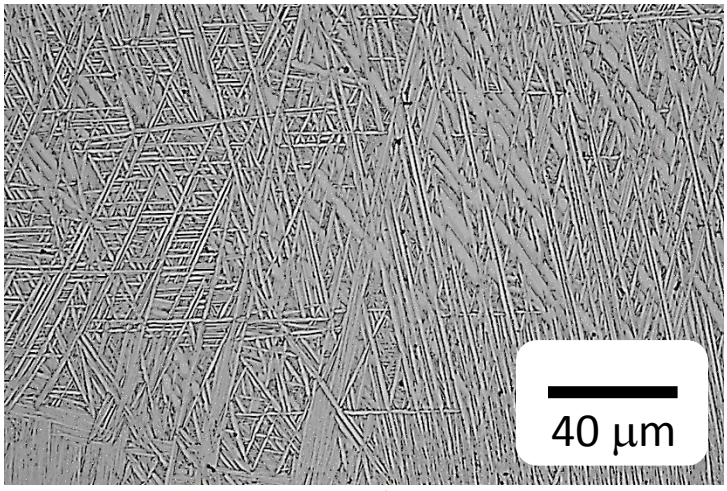

(b) 0.1/sec

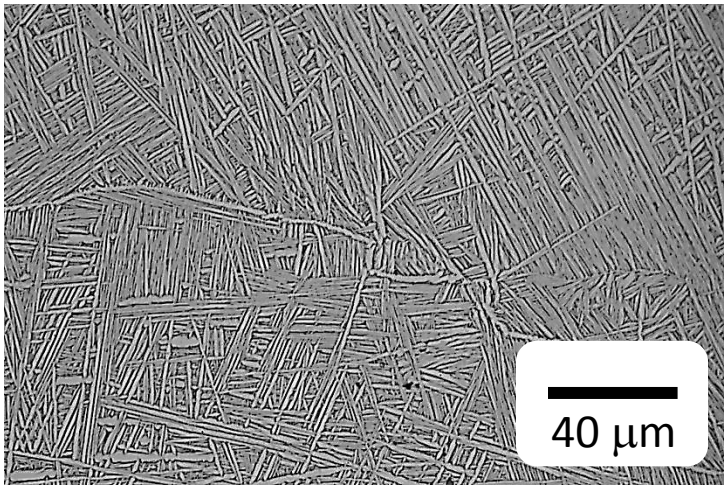

(c) 0.01/sec

Figure 60: Optical Micrographs of PH 3-2 at 940°C and at different strain rates (compression direction is vertical)

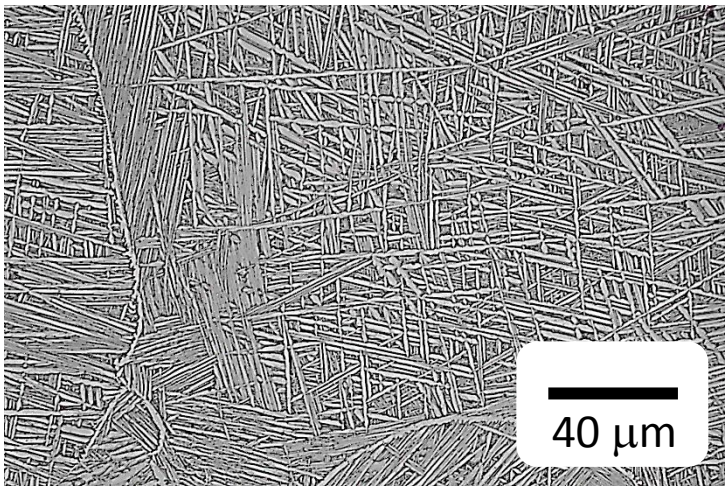

(a) 1/sec

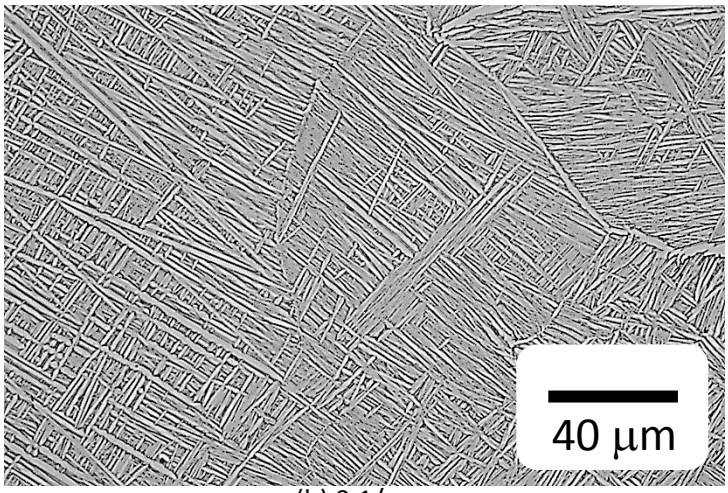

(b) 0.1/sec

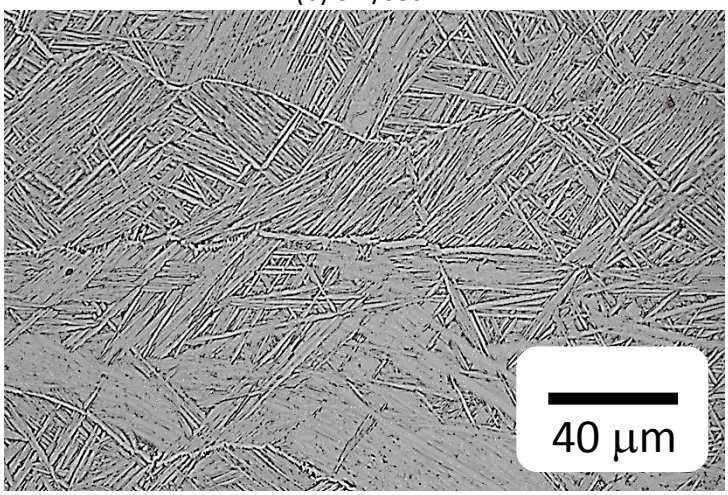

(c) 0.01/sec

Figure 61: Optical Micrographs of PH 3-2 at 996°C and at different strain rates (compression direction is vertical)

Figures 62 to 65 show the microstructures of the deformed samples of β processed + HIPed at different strain rates and at temperatures of 829^{o}C, 885^{o}C, 940^{o}C and 996^{o}C.

Figures 62 (a) (b) and (c) show the microstructures of the sample deformed at a temperature of 829^{o}C and at different strain rate. As compared to the microstructure of the undeformed sample (Figure 12(d)) it is observed that no much change in microstructure is observed except for the orientation of the α lamellae which was unoriented before the deformation and after the deformation the α lamellae were oriented perpendicular to the compression axis and it is seen that the α lamellae get coarsened as the strain rate is reduced. Figures 63 (a) (b) and (c) show the microstructures of the samples deformed at a temperature of 885^{o}C and from the figures it is seen that small amount of kinking is observed at all strain rates as compared to the microstructures of samples deformed at 829^{o}C. Figures 64 (a) (b) and (c) show the microstructures of the samples deformed at 940^{o}C and from the figures it is observed that the degree of coarsening of α lamellae is much higher than compared to undeformed microstructure (Figure 12(d)) and also the degree of α coarsening increases as the strain rate is decreased. Microstructures of the sample deformed at a temperature of 996^{o}C and at different strain rates are seen in Figures 65 (a) (b) and (c). A fully lamellar structure is seen at faster strain rate and as the strain rate is decreased small amounts of retained α in the lamellar transformed beta structure are observed.

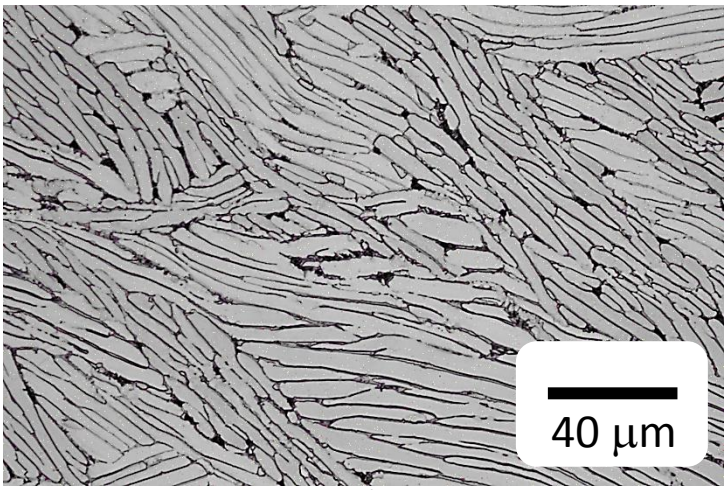

(a) 1/sec

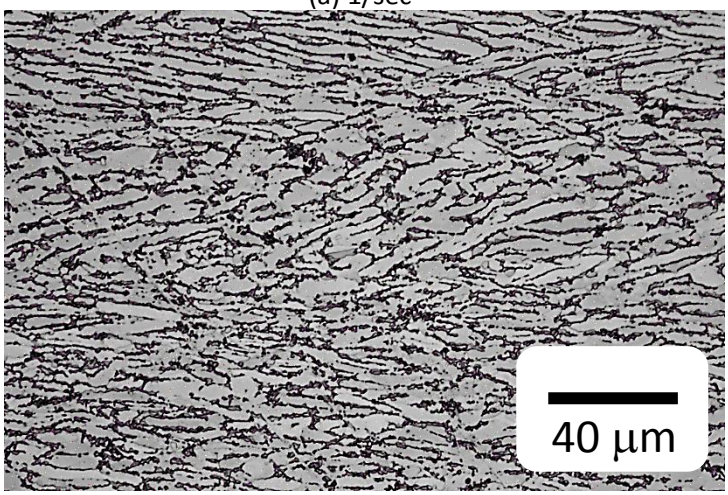

(b) 0.1/sec

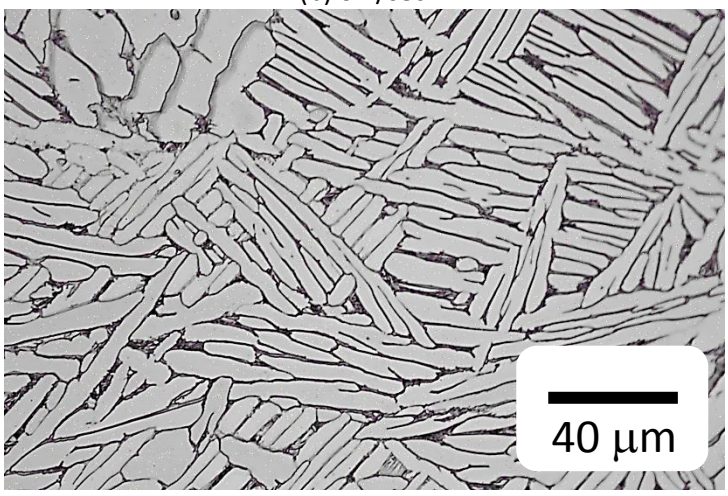

(c) 0.01/sec

Figure 62: Optical Micrographs of 3-2 at 829^{o}C and at different strain rates (compression direction is vertical)

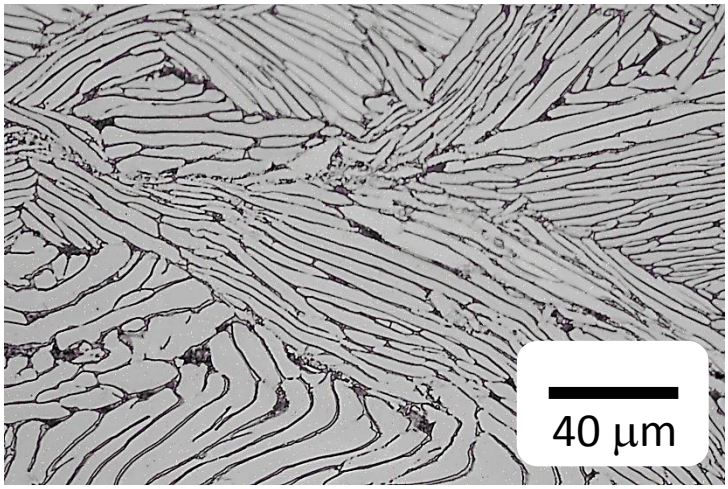

(a) 1/sec

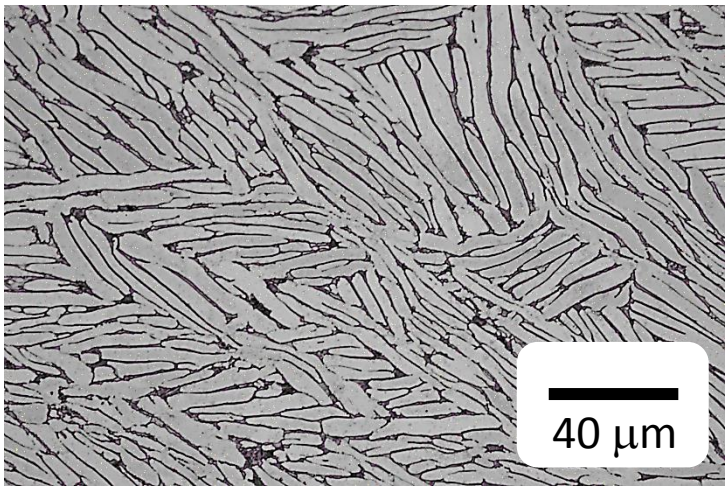

(b) 0.1/sec

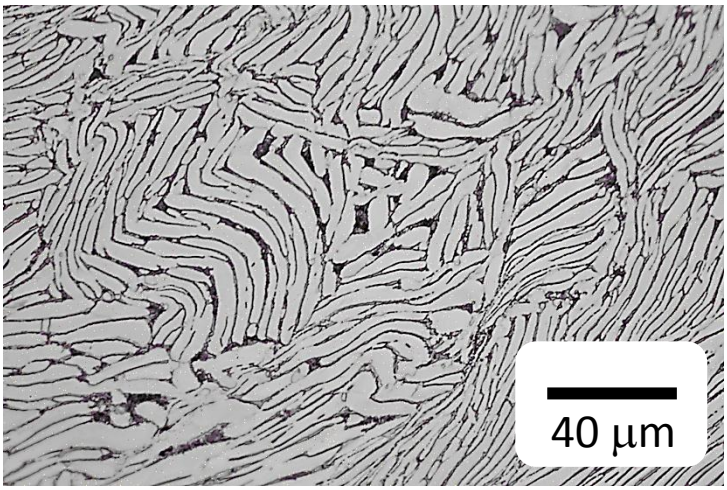

(c) 0.01/sec

Figure 63: Optical Micrographs of 3-2 at 885°C and at different strain rates (compression direction is vertical)

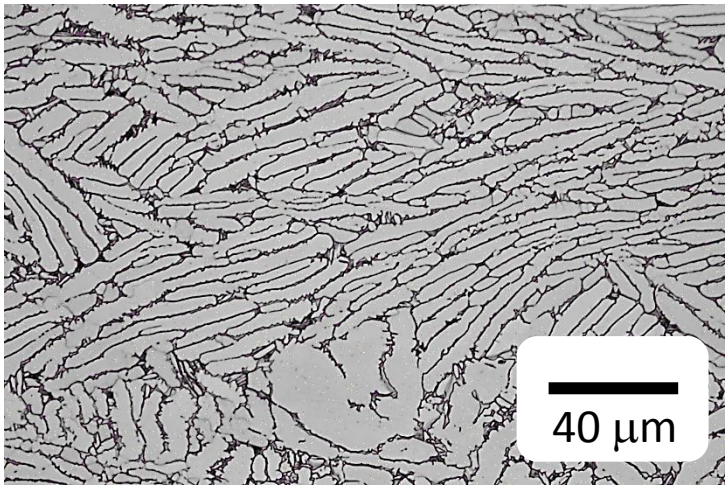

(a) 1/sec

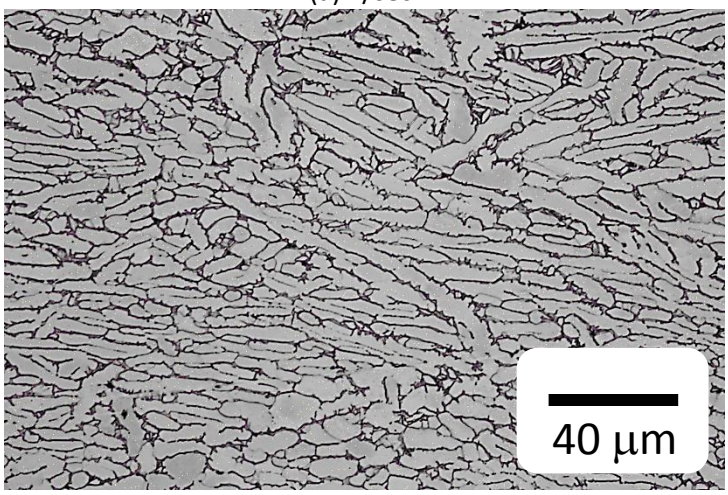

(b) 0.1/sec

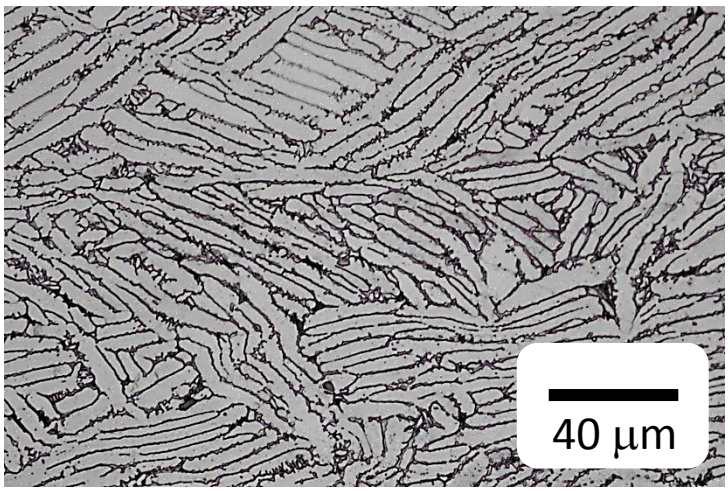

(c) 0.01/sec

Figure 64: Optical Micrographs of 3-2 at 940°C and at different strain rates (compression direction is vertical)

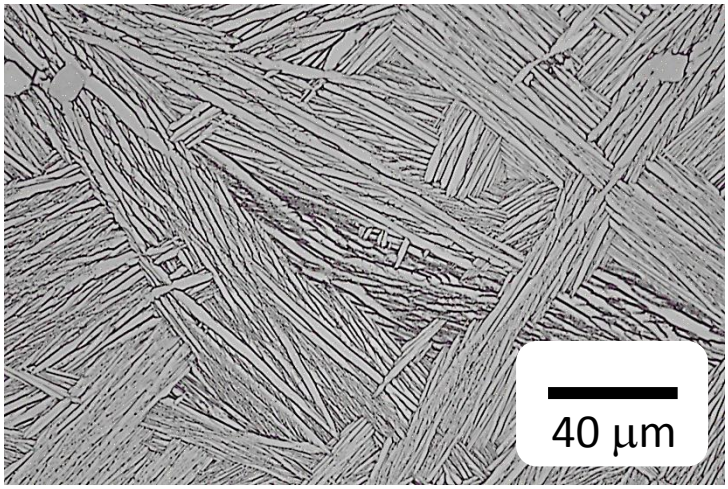

(a) 1/sec

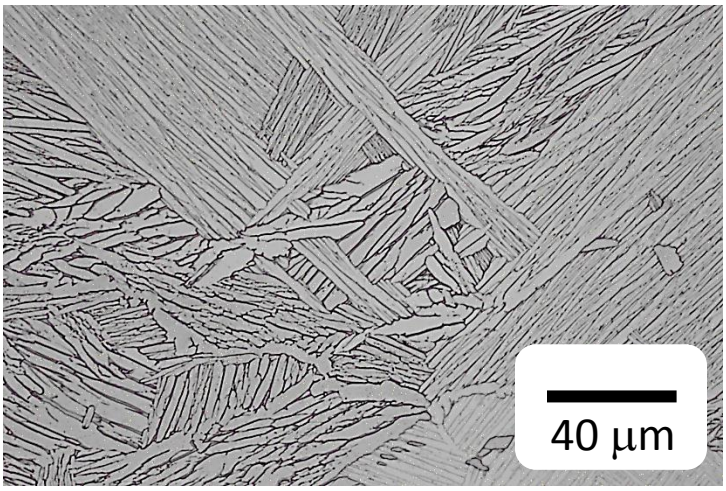

(b) 0.1/sec

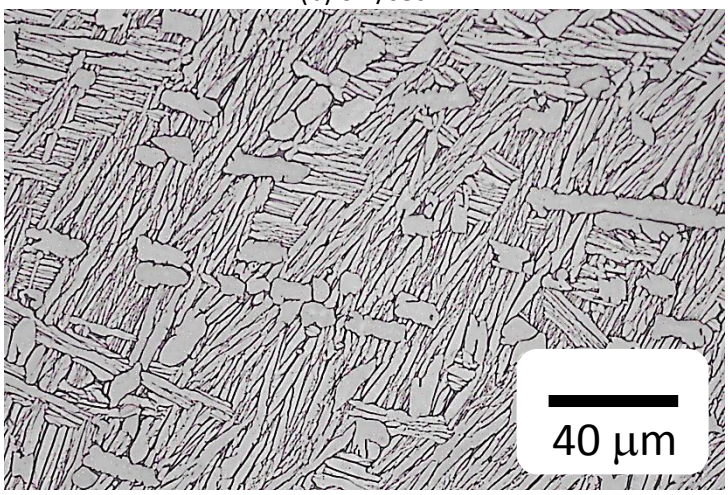

(c) 0.01/sec

Figure 65: Optical Micrographs of 3-2 at 996°C and at different strain rates (compression direction is vertical)

4.4 Finite Element Analysis

The process for estimating correction for deformation heating was described in section 4.1. In principle the corrected flow curves shown in Figures 27 and 29 can be used as an input for finite element simulation of the compression test and the load versus elongation curves of the simulations could be comparable to the experimental results. For this an axisymmetric finite element model was used to study the high temperature deformation. A schematic of the model is shown in Figure 66.

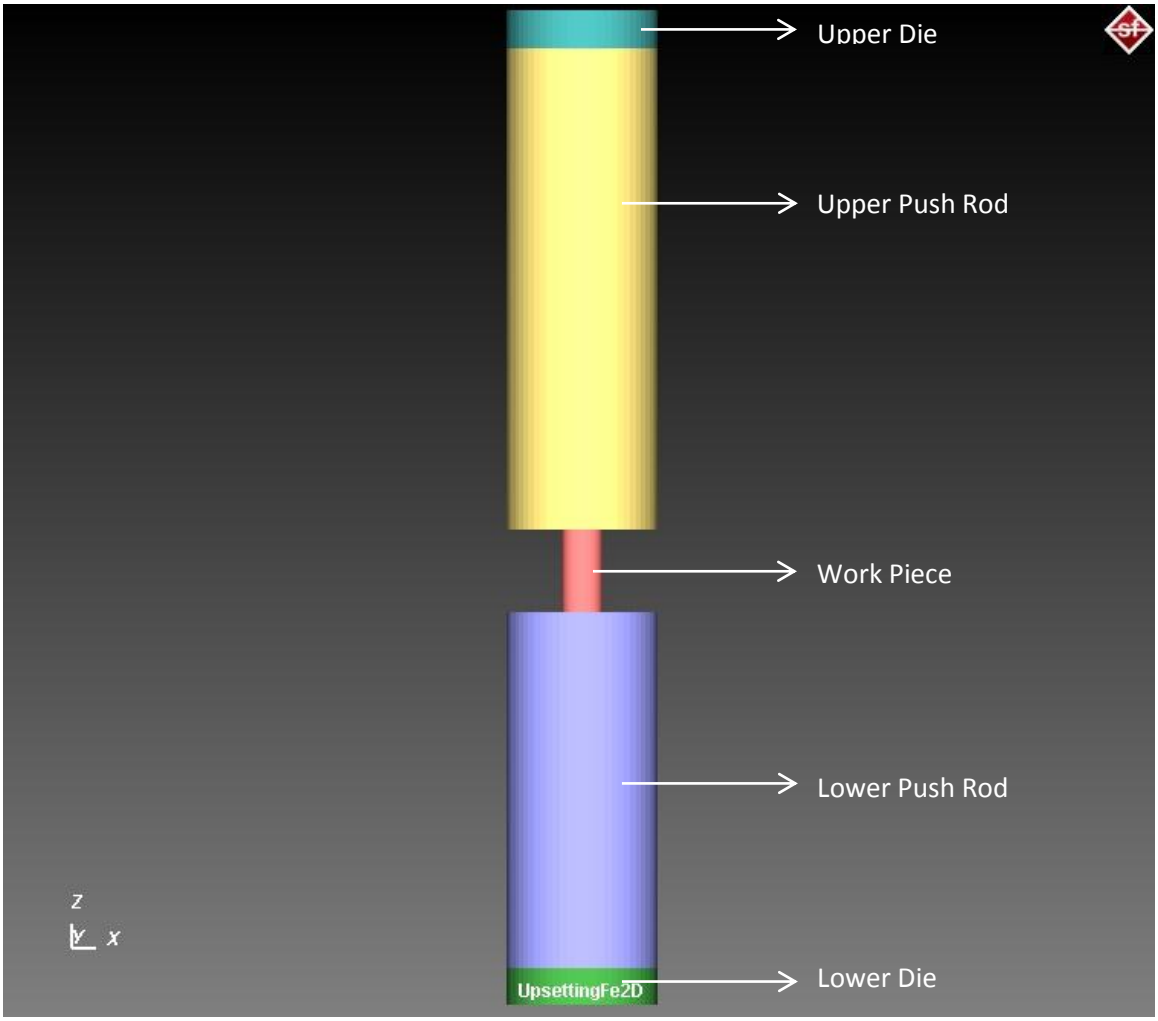

Figure 66: Schematic of finite element analysis model

Finite element analysis software called SIMUFACT FORMING was used in this study [25]. Table 8 shows the dimensions of the different parts used in the simulation. A total of twelve simulations (4 temperatures and 3 different strain rates) were carried out for the HIPed and α+β processed alloy and the same kind of behavior is assumed for the other alloys too. The elastic and plastic properties of the die materials and the sample are given in Table 9.

Table 8: Dimensions of different parts

Part	Dimensions
Specimen	32 mm X 16 mm Ø
Lower Die	15 mm X 60 mm Ø
Upper Die	15 mm X 60 mm Ø
Lower Push Rod	140 mm X 60 mm Ø
Upper Push Rod	190 mm X 60 mm Ø

The yield stress values varied for different temperatures and strain rates and were obtained from the compression test experiments. All the simulations were carried out to a 50% reduction in height of the samples. Figures 67 to 73 show the experimental versus simulated load versus elongation curves at different temperatures and strain rates. From the figures it is observed that at all temperatures and at all strain rates the flow curves of simulated and experimental flow curves are almost the same.

Table 9: Elastic and plastic values at room temperature

Property	Ti-6Al-4V	TMZ
Young's Modulus (GPa)	114	27
Poisson's Ratio	0.33	0.33
Density (kg/m^3)	4430	10200
Thermal Conductivity (W/m*K)	6.6	98
Specific heat (J/kg*K)	565	310
Coeff of Thermal Expansion (K^{-1})	1.1e-005	5.8e-006

Figures 70, 71 and 72 show the distribution of plastic strain, strain rate and temperature across the sample. From the figures it is seen that the distribution is not uniform throughout as assumed for the experimental analysis. However from figures 63 to 68 it is seen that by the use of temperature corrected values, a relatively good agreement is observed between the experimental and the simulated load extension curves.

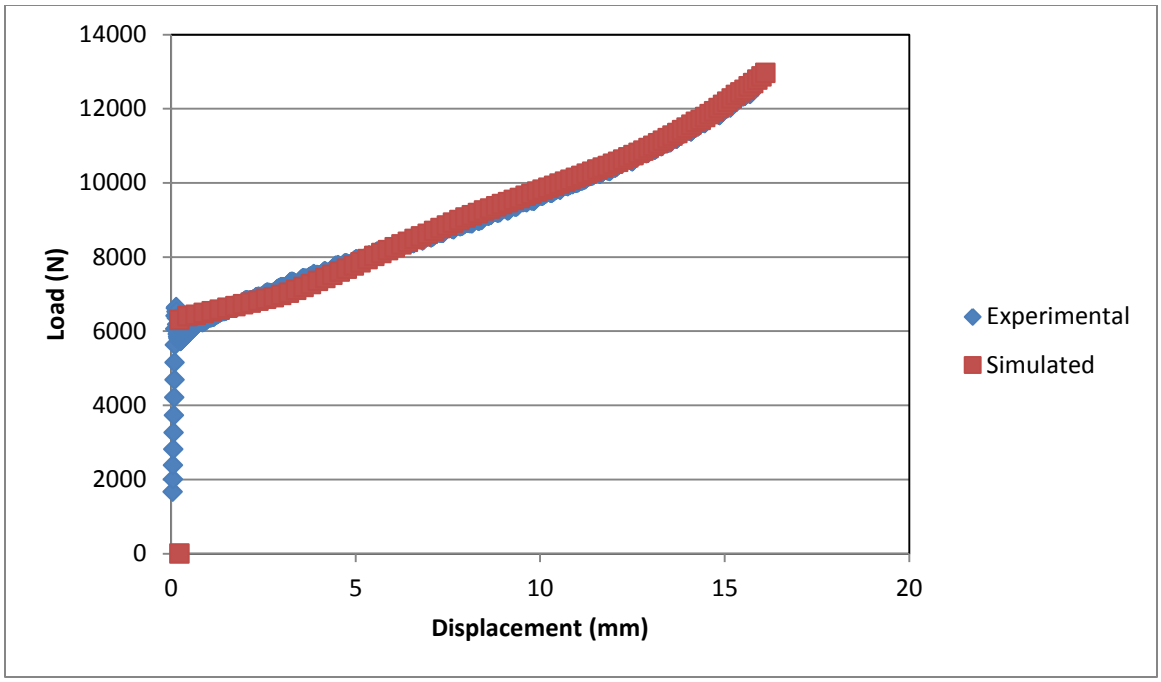

Figure 67: Experimental v/s Simulated load-displacement curve at 996^{o}C at a strain rate of 10^{-1} s^{-1}

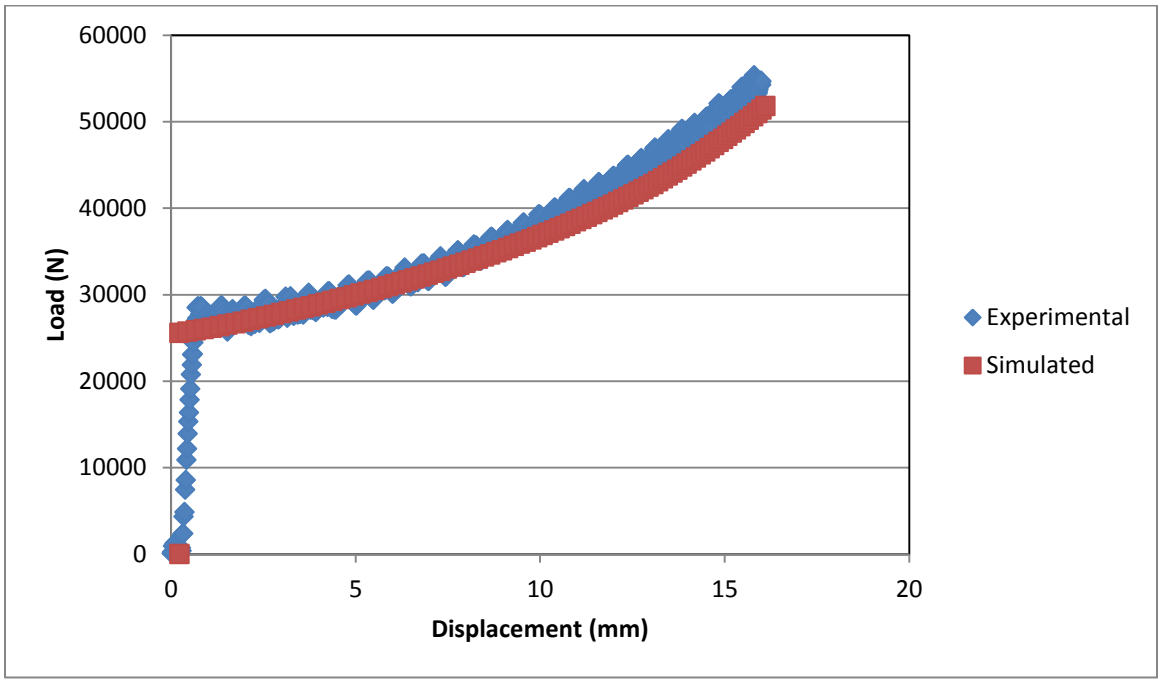

Figure 68 : Experimental v/s Simulated load-displacement curve at 829^{o}C at a strain rate of 10^{-2} s^{-1}

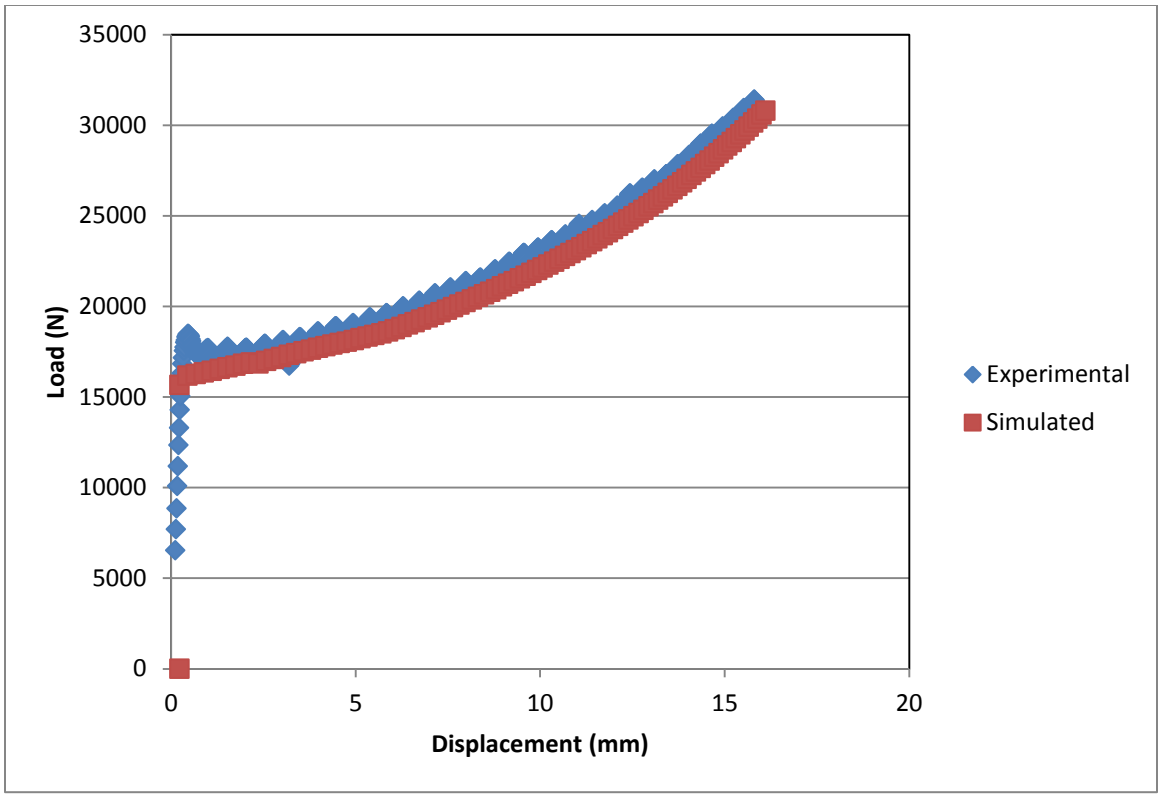

Figure 69 : Experimental v/s Simulated load-displacement curve at 885°C at a strain rate of 10^{-2} s^{-1}

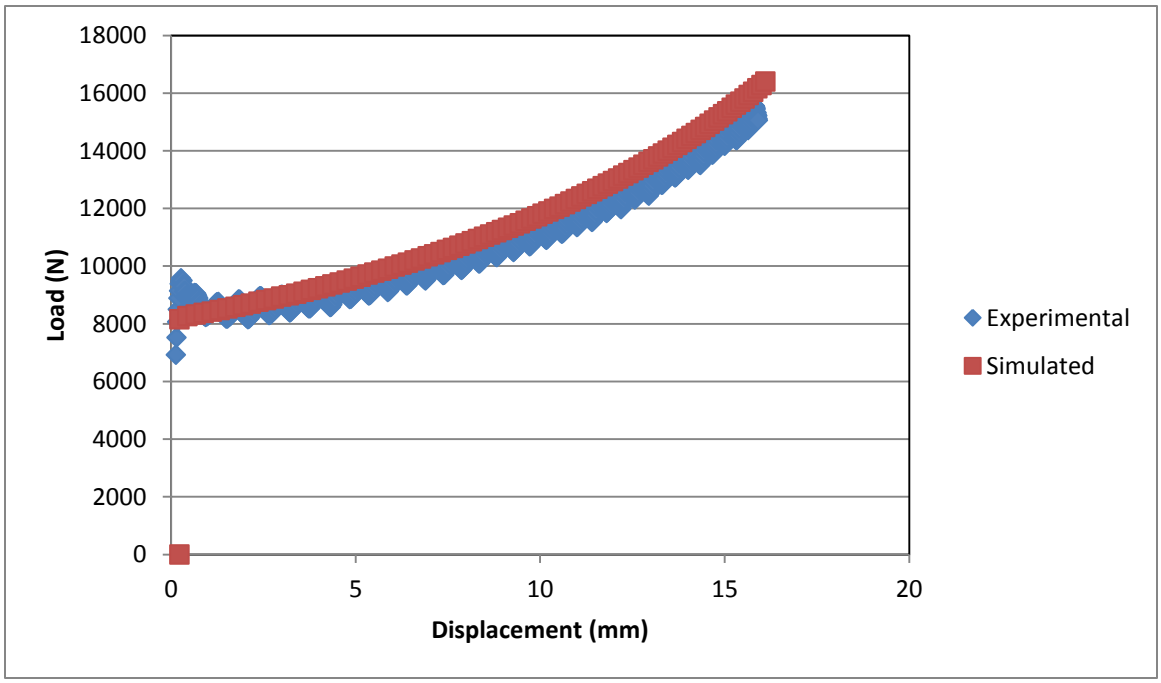

Figure 70 : Experimental v/s Simulated load-displacement curve at 940°C at a strain rate of 10^{-2} s^{-1}

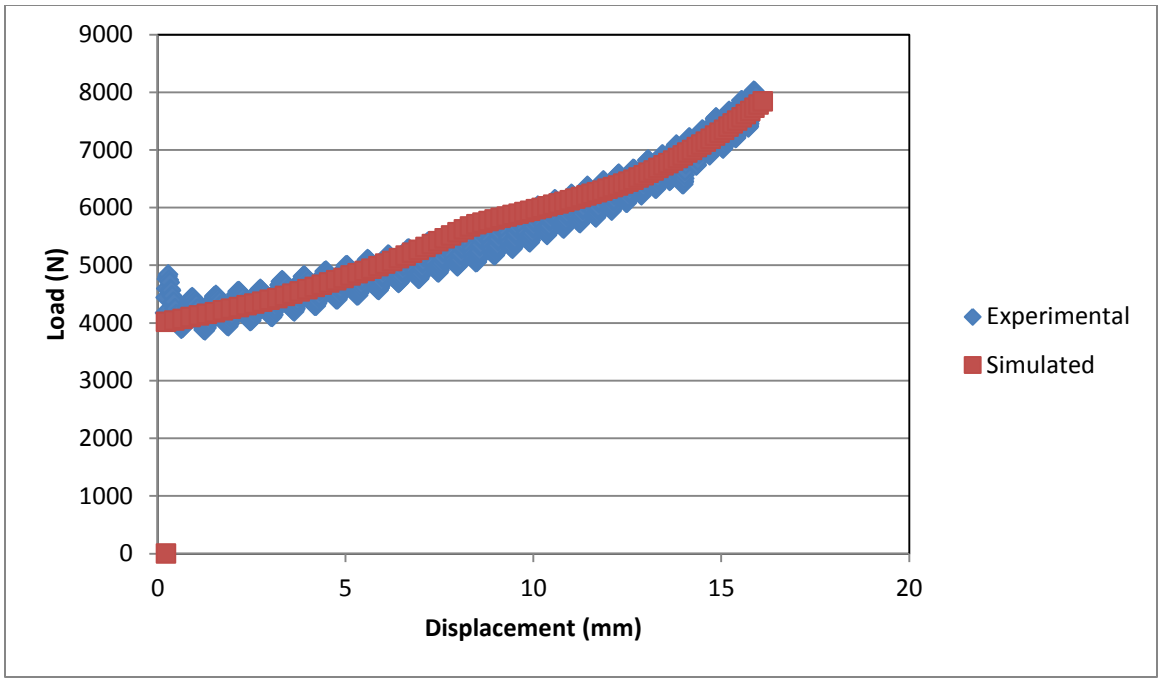

Figure 71 : Experimental v/s Simulated load-displacement curves at 996°C at a strain rate of 10^{-2} s^{-1}

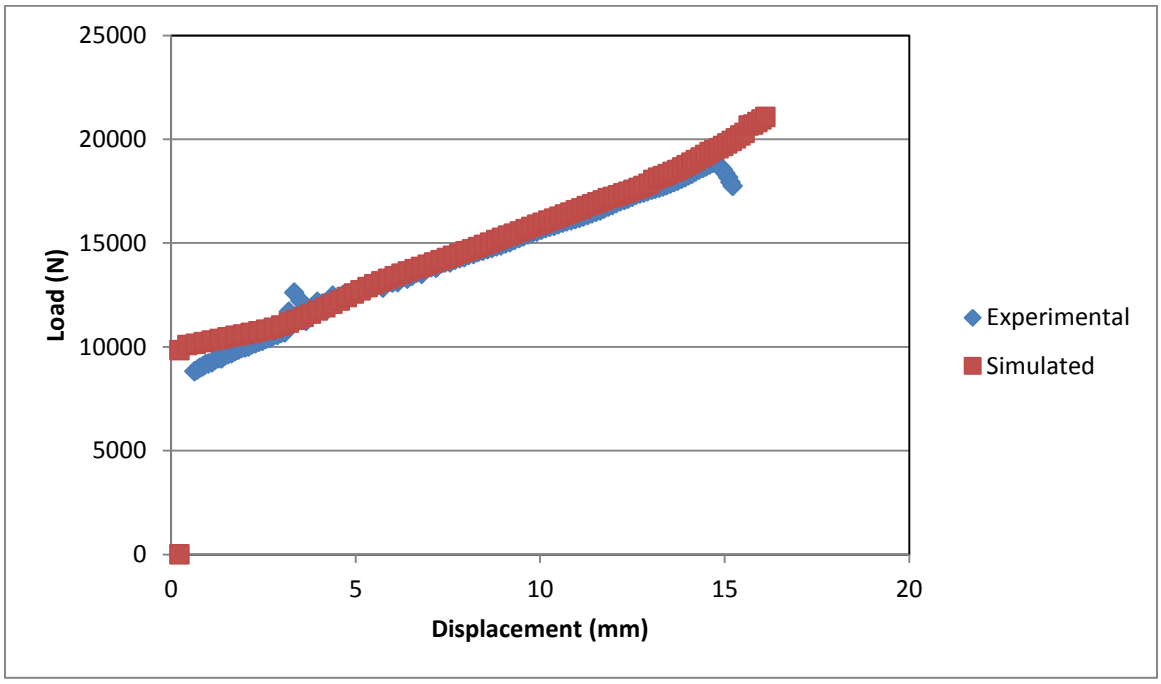

Figure 72 : Experimental v/s Simulated load-displacement curve at 940°C at a strain rate of 10^{0} s^{-1}

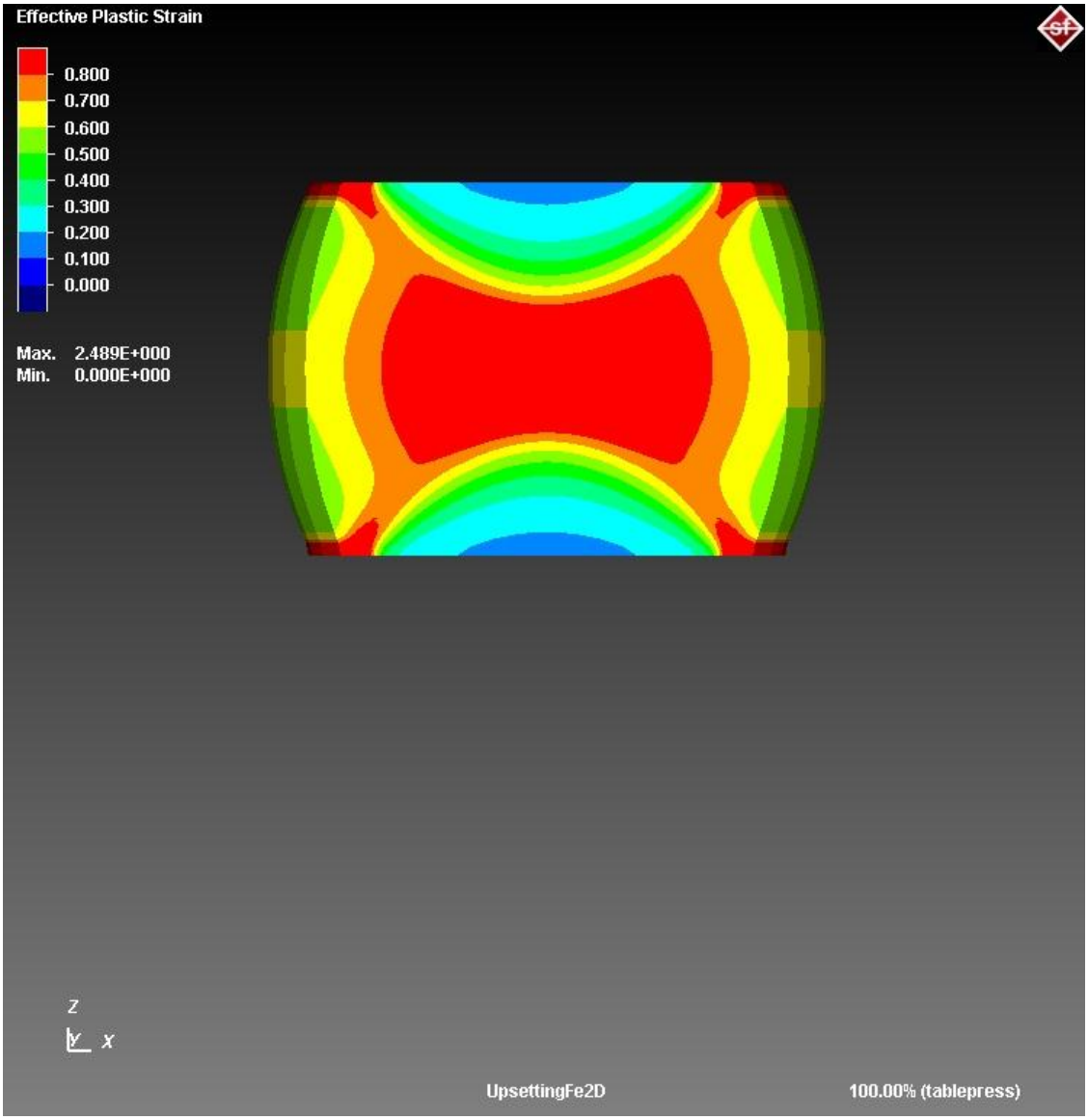

Figure 73: Effective Plastic Strain distribution across the sample

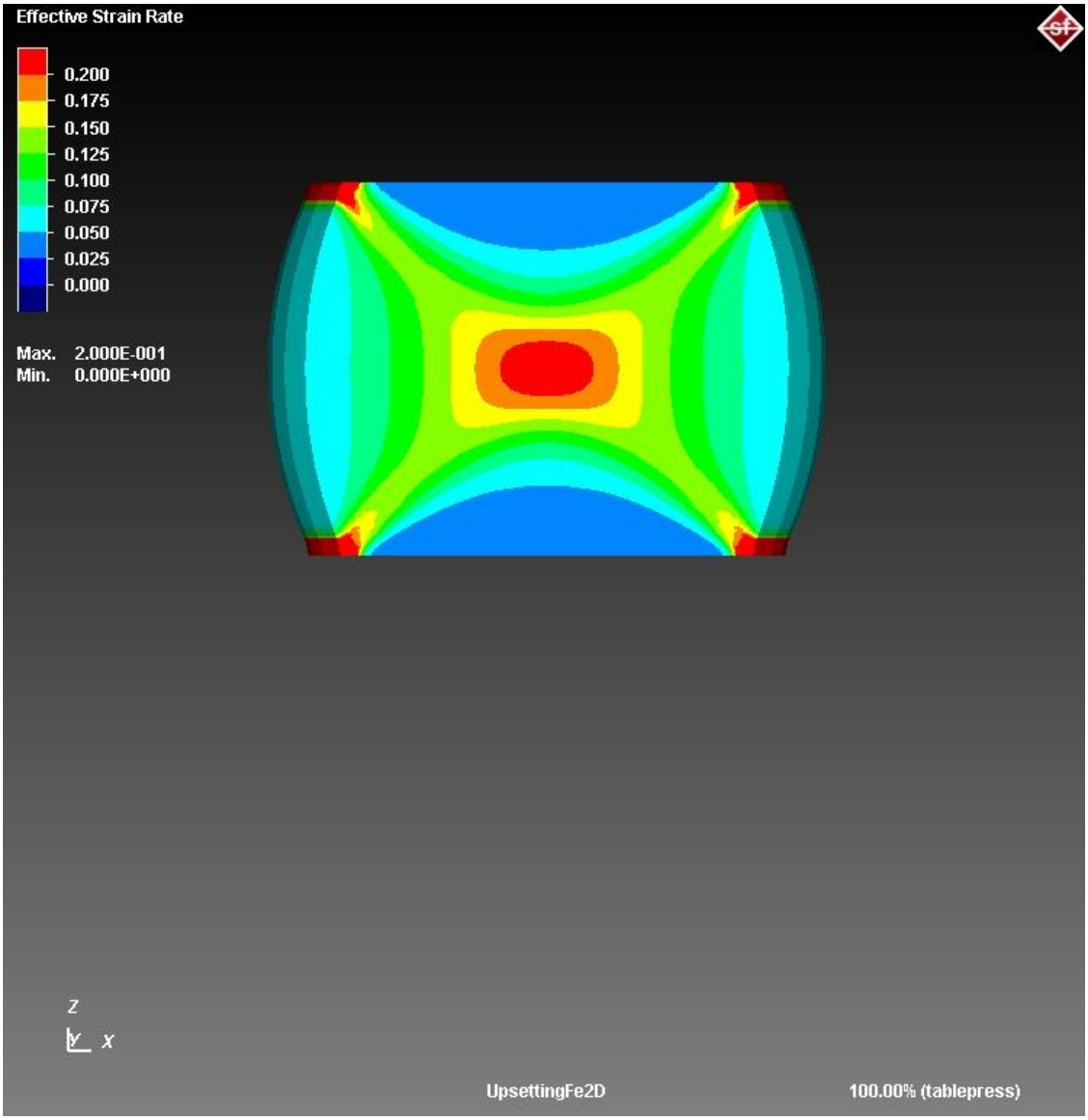

Figure 74: Effective Strain Rate distribution across the sample

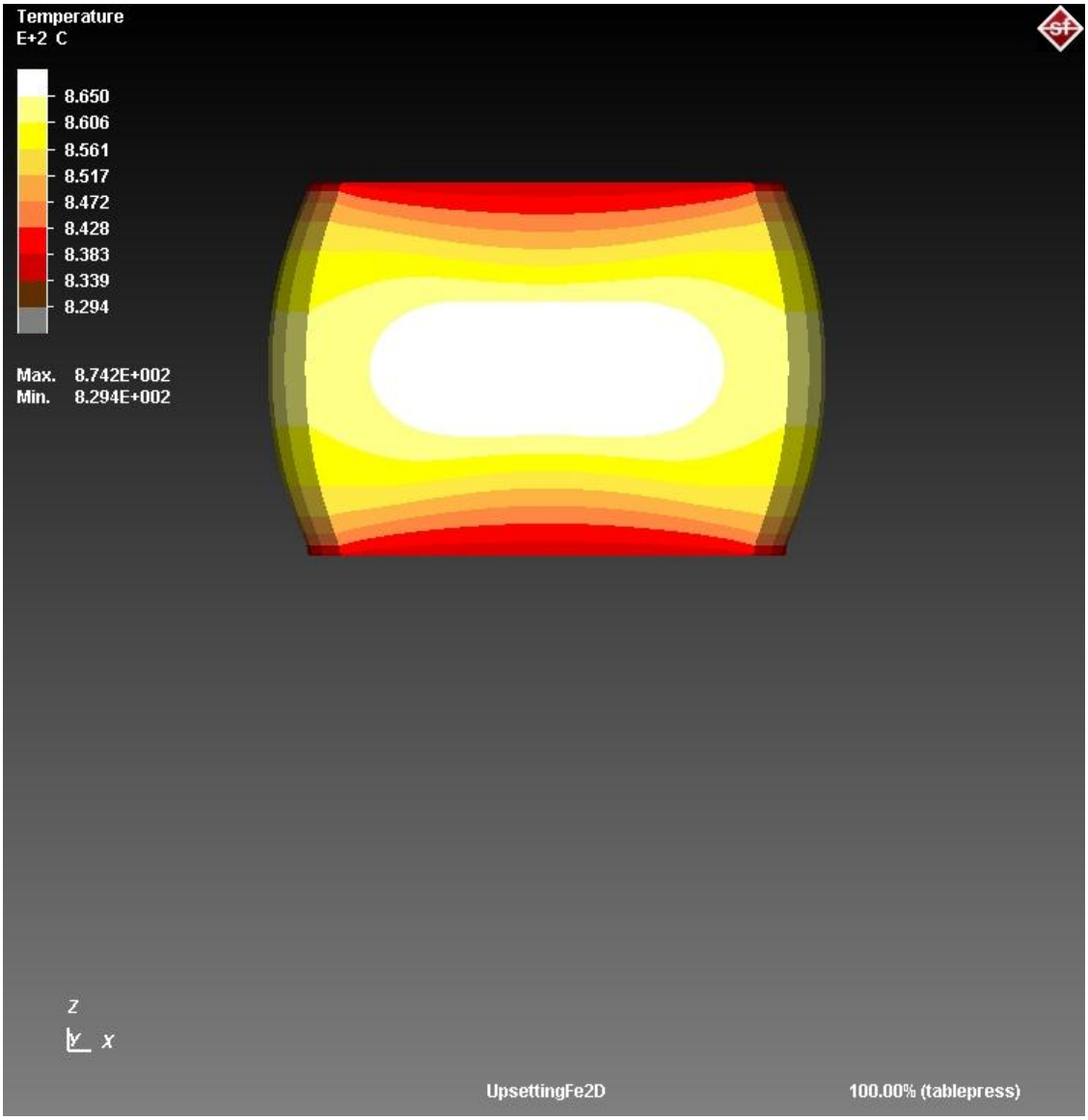

Figure 75: Temperature distribution across the sample

Chapter 5

Summary and Conclusions

1. Constant strain rate isothermal deformation tests were carried out on an ELI grade of Ti-6Al-4V which were processed to four different conditions which are:
    a. α+β processed
    b. α+β processed + HIPed
    c. β processed
    d. β processed + HIPed

    Tests were conducted over temperature range of 829^{o}C to 996^{0}C and strain rates 10^{-2} s^{-1}, 10^{-1} s^{-1} and 10^{0} s^{-1} to a final strain of 0.693 (50% reduction in height).
2. The flow behavior for all the materials was a peak stress was at a low strain value followed by flow softening at higher strains.
3. For all the materials the strain rate sensitivity value m increased with increase in temperature. The average values of m are:
    a. α+β processed: 0.2161
    b. α+β processed + HIPed: 0.1784
    c. β processed: 0.2539
    d. β processed + HIPed: 0.1741
4. The apparent activation energies of deformation for the different materials were determined to be
    a. α+β processed: 231.45 kJ/mol

b. α+β processed + HIPed: 321.61 kJ/mol

c. β processed: 107.77 kJ/mol

d. β processed + HIPed: 251.79 kJ/mol

5. The flow curves, which were corrected for deformation heating, were used as input for the finite element modeling. The load – deformation curves predicted by the simulation were found to be comparable with experimental results.

6. Microstructural changes:

   a. The α+β processed material had an initial microstructure of kinked lamellae. After the deformation the lamellae seem to have re - oriented to a direction perpendicular to compression direction. For the samples deformed below beta transus it is observed that the degree of coarsening of the lamellae increased as the deformation temperature was increased and also as the strain rate reduced at a given test temperature. When tested above the beta transus, the resulting microstructure consisted of transformed beta in addition to some amounts of retained alpha phase.

   b. The α+β processed + HIPed material had an initial microstructure of kinked lamellae but the width of the α lamellae was greater than that of the α+β processed material. As in the case of α+β processed material, in this material to the lamellae got oriented to compression direction after the deformation was done. For the samples tested below the beta transus temperature coarsening of the lamellae was observed as the temperature was increased and also when the strain rate was decreased at a given test

temperature. For the α+β processed material, as the test temperature was near the beta transus, small amounts of β along with α lamellae were observed which unlike the unHIPed α+β processed material. For the samples tested above the beta tansus, at all strain rates the microstructure consisted of β lamellae in addition to small amounts of retained α phase.

c. The β processed material exhibited a basket weave structure also known as Widmanstatten structure. For the samples deformed at 829^{o}C and 885^{o}C a bimodal structure of globular α and lamellar α+β regions were observed. The samples tested near and above the beta transus temperature exhibited a Widmanstatten structure, but here the width of the lamellae was greater than those in the initial microstructure.

d. The β processed + HIPed material initially exhibited a Widmanstatten structure but the width of the lamellae was greater than that of the β processed material. Before the deformation the lamellae were un-oriented, but after the deformation the lamellae got oriented perpendicular to the compression direction. For the samples deformed below the beta transus temperature, it is observed that width of the lamellae increased as the temperature of deformation was increased, and also with decrease in strain rate at a given test temperature. For the samples deformed above the beta transus a fully lamellar structure was observed at faster strain rates, and as the strain rate was decreased small amounts of retained alpha in the lamellar transformed beta structure were observed.

Reference:

1. R. Boyer, G. Welsch and E. W. Collings, Materials Properties Handbook: Titanium Alloys. Metals Park, OH, ASM, 1994.
2. J. Donachie, Jr., Titanium: A Technical Guide, Metals Park, OH, ASM International, 1988.
3. B. Hurless and F. Froes, "Lowering the cost of titanium", AMPTIAC Quarterly, vol. 6, pp. 2-9, 2002.
4. H. E. Boyer and T. Gall, Metals Handbook: Desk Edition. ASM, 1992.
5. C. Leynes and M. Peters, Titanium and Titanium alloys: Fundamentals and Applications. Wiley-VCH, 2003.
6. J. Peters, J. Hemptenmacher, J. Kumpfert, and C. Leyens, Structure and Properties of Titanium and Titanium Alloys. Germany: Willey-VCH, 2003.
7. O. E. Pohler, "Unalloyed titanium for implants in bone surgery Injury", Int. J.Care Injured, vol. 31, no. S, pp. D7-13, 2000.
8. N. Mitsuo, "Mechanical properties of biomedical titanium alloys", Materials Science and Engineering A, vol. 243, pp. 231-236, 1998.
9. K. Takao and K. Kusukawa., "Low-cycle fatigue behavior of commercially pure titanium", Materials Science and Engineering A, vol. 213, pp. 81-85, 1996.
10. I. Weiss and S. Semiatin, "Thermomechanical processing of alpha titanium alloys- an overview", Materials Science and Engineering A, vol. 263, pp. 243-256, 1999.
11. I. Walker., "Considerations on the selection of alloys for use in pressure cells at low temperatures", Cryogenics, vol. 45, pp. 87-108, 2005.

12. G. Lutjering., “Influence of processing on microstructure and mechanical properties of alpha+beta titanium alloys”, Materials Science and Engineering A, vol. 243, pp. 32-45, 1998.

13. P. J. Bania, “Beta titanium alloys and their role in the titanium industry”, Beta Titanium alloys in the 1990’s, pp. 3-14, TMS, 1993.

14. G. E. Dieter, Mechanical Metallurgy, Mc Graw Hill, SI Metric ed., 1988.

15. Y. Prasad, T. Seshacharyulu, S. C. Medeiros and W. Frazier, “A study of beta processing of Ti-6Al-4V: Is it trivial?” Journal of Engineering Materials and Technology, vol. 123, pp. 355-360, 2001.

16. T. Seshacharyulu, S. C. Medeiros, W. Frazier, Y. Prasad, “Hot working of commercial Ti-6Al-4V with an equiaxed α-β microstructure: materials modeling considerations”, Material Science and Engineering A, vol. 284, pp. 184-194, 2000.

17. G. Lutjering, J. Williams, Engineering material and process: Titanium, Springer, second edition, 2007.

18. M.Benedetti, V.Fontanari, “The role of bimodal and lamellar microstructures of Ti-6Al-4V on the behavior of fatigue cracks emanating from edge-notches”, European Structural Integrity Society, ECF15.

19. N. S. Reddy, Y. H. Lee, C. H. Park, C. S. Lee, “Prediction of flow stress in Ti-6Al-4V alloy with an equiaxed α+β microstructure by artificial neural networks”, Material Science and Engineering A, vol. 492, pp. 276-282, 2008.

20. G. Lutjering, M. Peters, “Titanium `80, Science and Technology”, AIME, p.925, 1980.

21. F. C. Campbell, Elements of Metallurgy and Engineering Alloys, ASM International, 2008

22. R. L. Goetz and S. L. Semiatin, “The adiabatic correction factor for deformation heating during uniaxial compression test”, Journal of Materials Engineering and Performance, vol. 10, pp. 710-717, 2001.

23. P. Dadras and J. F. Thomas, Metall. Trans. A, vol. 12A, pp. 1867-1873, 1981.

24. J. Weertman, “Zener - Stroh crack, Zener – Hollomon parameter and other topics”, J. Appl. Phys., vol.60, 1877, 1986.

25. A. J. Buijik, “Finite Volume (FV) and Finite Element (FE) integration in Simufact.forming”, 08 SFA-101, 2008.